UNIVERSIDAD DE CHILE
FACULTAD DE CIENCIAS FÍSICAS Y MATEMÁTICAS
DEPARTAMENTO DE ASTRONOMÍA

THE ROLE OF CONTINENTS ON THE GLOBAL SURFACE TEMPERATURE OF AN EARTH-LIKE PLANET

TESIS PARA OPTAR AL GRADO DE
MAGISTER EN CIENCIAS, MENCIÓN ASTRONOMÍA

ALEJANDRA GINETTE MEZA RAVEST

PROFESOR GUÍA:
PATRICIO ROJO RUBKE

MIEMBROS DE LA COMISIÓN:
CÉSAR FUENTES GONZÁLEZ
RENÉ GARREAUD SALAZAR
DIEGO MARDONES PÉREZ

SANTIAGO DE CHILE
2024

El rol de los continentes en la temperatura superficial global de un planeta similar a la Tierra

La habitabilidad, es decir, la capacidad de un planeta para sostener vida, está intrínsecamente ligada a la presencia de agua líquida, la cual, a su vez, depende de la temperatura. La distancia entre un planeta y su estrella anfitriona es el principal parámetro aparente para determinar estas temperaturas. Sin embargo, los entornos geodinámicos y geofísicos también impactan significativamente en la habitabilidad de un planeta (Lammer *et al.*, 2009).

Estos entornos abarcan numerosos factores que pueden modificar la temperatura de un planeta, como la composición de su atmósfera (gases de efecto invernadero) y la composición de su superficie (hielo marino, glaciares, océanos, tierra continental, etc.). Estudios recientes han revelado la influencia de la composición superficial planetaria en la climatología de mundos rocosos (Madden and Kaltenegger, 2020). En consecuencia, este estudio propone investigar cómo las alteraciones en la distribución de masas terrestres pueden afectar la temperatura de un planeta y, por ende, su habitabilidad.

Para llevar a cabo esta investigación, utilizamos Planet Simulator (PlaSim), un modelo de circulación general de complejidad intermedia diseñado para la Tierra y otros cuerpos planetarios. Mediante un cambio gradual en la superficie continental, exploramos cómo estas modificaciones afectan la temperatura de un planeta similar a la Tierra.

Al eliminar diferentes continentes, observamos que el albedo superficial y la interacción entre la superficie y la atmósfera son modificados directamente. Resultando en un cambio tanto en la temperatura superficial como en el albedo planetario.

Descubrimos que en general, la extracción de continentes provoca un aumento en la contribución de la atmósfera al albedo planetario. Sin embargo, la contribución específica tanto de la atmósfera como de la superficie al albedo planetario presenta un alto grado de complejidad, influenciado por parámetros como la ubicación y área de los continentes extraídos.

Por otro lado, la temperatura superficial está influenciada por el fenómeno conocido como 'continentalidad', la cual afecta principalmente continentes grandes en altas latitudes permitiéndonos inferir que planetas con excentricidad de 23° que posean estos continentes presentarán temperaturas más frías que los planetas que no los poseen.

The role of continents on the global surface temperature of an Earth-like planet

Habitability, the ability of a planet to support life, is intrinsically linked to the presence of liquid water, which, in turn, depends on temperature. The distance between a planet and its host star is the apparent main parameter in determining these temperatures. However, geodynamic and geophysical environments, also significantly impact a planet's habitability (Lammer *et al.*, 2009).

These environments encompass numerous factors that can modify the temperature of a planet, such as the composition of its atmosphere (greenhouse gases) and its composition's surface (sea ice, glaciers, oceans, continental land, etc.). Recent studies have revealed the profound influence of planetary surface composition on the climatology of rocky worlds (Madden and Kaltenegger, 2020). Consequently, this study proposes to investigate how alterations in the distribution of landmasses can affect a planet's temperature and, by extension, its habitability.

To conduct this investigation, we employed Planet Simulator (PlaSim), a general circulation model of intermediate complexity designed for the Earth and other planetary bodies. By performing a gradual change in the continental surface, we explore how these modifications affect the temperature of an Earth-like planet.

When different continents are removed, we observe that the surface albedo and the interaction between the surface and the atmosphere are directly modified, resulting in a change in both surface temperature and planetary albedo.

We find that, overall, the removal of continents leads to an increase in the contribution of the atmosphere to the planetary albedo. However, the specific contribution of both the atmosphere and the surface to the planetary albedo presents a high degree of complexity, influenced by parameters such as the location and area of the removed continents.

On the other hand, the surface temperature is influenced by the phenomenon known as 'continentality', which primarily affects large continents at high latitudes. This allows us to infer that planets with an eccentricity of 23° possessing these continents will have colder temperatures than planets that do not possess them.

A mi Venus
que hoy corre feliz en el cielo de los perritos

Agradecimientos

Agradezco principalmente a mis personas favoritas en la vida, mis papás. Gracias por siempre apoyarme y estar conmigo, no podría haber hecho esto sin ustedes, estoy muy feliz de ser su hija. Gracias a la Venus por ser la mejor compañera que pude tener, te extraño y te extrañaré por siempre. También, le agradezco a la Mei, que está acurrucada a mi lado en estos momentos, por ayudarme a crecer y acompañarme en este último trayecto. De igual manera, le doy las gracias al Toffee por alegrarme el año.

Mi agradecimiento especial a quienes estuvieron incluso antes de empezar este camino. Al Gabo por todas las aventuras y conversaciones por el barrio, a la Cami por ser mi mejor amiga y uno de los pilares más importantes en mi vida, al Sergio por siempre cuidarme y a la Java por esas noches de risas y llantos.

Me gustaría agradecer también a las personitas que tuve el lujo de conocer dentro de la Astronomía. Gracias a la Meli y Alexis por todos esos días de estudios, domingos incluidos. Sufrir juntos fue una de las partes más divertidas de la licenciatura. También gracias por ser mi mayor apoyo durante esos años, los quiero mucho. Gracias al Silvio por sus anectdotas y ser el mejor compañero de viajes. Al Presi por el apañe, el cariño y las risas. Al Emilio por ser uno de los mejores amigos que pude encontrar. Gracias por apoyarme, cuidarme y, sobre todo, acompañarme.

Gracias al Luis, principalmente por ser quien es. Conocerte ha sido de las cosas más lindas que me ha dejado la Astronomía y me siento muy afortunada de tenerte en mi vida. Gracias por alentarme todos los días y levantarme cada vez que sentía que no podía. Tu apoyo y ayuda ha sido crucial para mi este último año y te estaré siempre agradecida por eso.

Finalmente, pero no menos importante, gracias a Pato por la paciencia y la orientación. Me ayudó mucho a aprender y disfrutar este largo viaje llamado tesis. Así que probablemente lo siga molestando en el futuro jeje.

Table of Content

List of Tables

List of Figures

Chapter 1

Introduction

With over 5,500 confirmed exoplanets to date, the realm of potential study has expanded significantly, especially with advanced instruments such as the James Webb Space Telescope (JWST), offering detailed insights into planetary atmospheres. Consequently, the identification of planets worth in-depth investigation becomes crucial.

One of the primary criteria driving this interest is a planet's habitability. To sustain life, a planet must have energy sources and liquid water—components challenging to find beyond our planet but important for the metabolic processes of various species. The habitable zone, defined as the region around a star where the flux of incident radiation could support liquid water, serves as a quantitative reference and acts as the primary filter used by researchers to assess a planet's potential interest.

However, determining the habitability of a planet extends beyond this criterion, as it is necessary to consider other factors, including the planet's orbital, geodynamic, and geophysical characteristics. (Lammer *et al.*, 2009).

To date, studies have investigated how planetary orbital features, including obliquity and eccentricity, affect planets completely covered by the sea, known as aquaplanets. Findings indicate that planets with seasonal variability boast a larger habitable zone (Linsenmeier *et al.*, 2015), and for obliquity, a planet is fully habitable if it remains below 54° (Nowajewski *et al.*, 2018). Furthermore, researchers propose that a planet, sharing Earth's configuration, may exhibit heightened habitability with increased obliquity and/or eccentricity (Jernigan *et al.*, 2023).

In the geodynamic and geophysical setting, recent research underscores the importance of various surface components in planetary habitability (Madden and Kaltenegger, 2020), including investigations into the impact of continent size on exoplanets (Salazar *et al.*, 2020). Notably, land mass significantly influences planetary climate, playing a key role in weathering, influencing greenhouse gas levels (especially CO2), and facilitating nutrient transport to oceans—releasing essential substances like phosphates and nitrates (Derry, 2009). Additionally, land mass is a key component among the five main elements shaping climate, alongside the biosphere, cryosphere, hydrosphere, and atmosphere.

Building on these studies, our investigation delves into the influence of continental mass on planetary surface temperatures—a critical factor directly tied to habitability. Employing the Planet Simulator (PlaSim), a general circulation model developed by the University of Hamburg, we constructed Earth-based models of planets. In these models, continents were systematically removed, along with all parameters directly associated with them. This method allowed us to scrutinize the effects of gradual changes in continental area,in comparison to present-day Earth, on surface temperatures. This approach contributes to an improved understanding of the pivotal role played by continental mass in shaping planetary climates.

Chapter 2

Methodology

Creating simulations based on worlds as complex as our planet, even in a simplified way, involves an incredibly high computational cost. For this reason, it is important to select an efficient model that can simulate a large number of geologic years in a short time while delivering the most realistic output possible.

PlaSim (Planet Simulator) was thus chosen to perform the numerical simulations. Planet Simulator is a climate model of intermediate complexity(MIC) for Earth, Mars, and other planets that can be downloaded for free on the website of the University of Hamburg[1].

2.1 Model

The package available for download from the webpage includes two models: the Portable University Model of the Atmosphere (PUMA) and the Planet Simulator (PlaSim). PUMA is a simplified general circulation model (GCM) with a dynamical core, relying on linear processes like Newtonian cooling and Rayleigh friction (Fraedrich *et al.*, 2005). In contrast, PlaSim, while also featuring an atmospheric GCM like PUMA, encompasses additional components of the climate system, such as an ocean with sea ice and a land surface with a biosphere. These compartments are, however, simplified into low-complexity systems for this version.

2.1.1 Dynamical Core

To represent the conservation of momentum, mass, and energy, the dynamical core of PlaSim is based on their corresponding moist primitive equations:

- First law of thermodynamics.
- Equation of state (with hydrostatic approximation)

[1] `https://www.mi.uni-hamburg.de/en/arbeitsgruppen/theoretische-meteorologie/modelle/plasim.html`

- Continuity equation
- Prognostic equations for the vertical component of vorticity and horizontal divergence
- Prognostic equation for water vapor (specific humidity)

2.1.2 Parameterizations and subsystems

The effect of unresolved processes is also included by simplified parameterization of boundary layer fluxes and diffusion, radiation, and moisture processes with interactive clouds. On the other hand, interaction with other climate subsystems is achieved by incorporating simplified models for land surface, vegetation, ocean, and sea ice processes. Thus:

- Boundary layers:
  Aerodynamic formulas parameterize surface fluxes for both zonal and meridional momentum, as well as sensible and latent heat.
- Radiation:
  - Shortwave:
    The shortwave radiation scheme structure is based on Lacis and Hansen (1974) for the clear atmosphere, incorporating Rayleigh scattering, ozone absorption, and water vapor absorption. For the cloudy region, albedos and transmissivities of high, medium, and low clouds can be predefined or parameterized, as proposed by Stephens *et al.* (1984).
  - Longwave:
    Longwave radiation in clear skies is calculated using a broadband emissivity approach, while clouds are treated as gray bodies whose emissivity is determined by their liquid water content.
- Land surface and soil:
  The model includes calculations for surface and soil temperatures, soil hydrology, and a fluvial transport scheme. Properties such as albedo, roughness length, and evaporation efficiency are also considered.
  Surface temperature is determined by the linearized energy balance within the top 0.2 meters of the soil. Subsurface layers, divided into five levels (0.4 m, 0.8 m, 1.6 m, 3.2 m, and 6.4 m), have their temperatures calculated based on the energy balance at each level.
- Ocean and sea ice:
  Sea surface temperatures and sea ice distributions can be established through climatology or modeling. The modeling approach combines a mixed layer model with a constant thickness of 50 meters and a thermodynamic model for sea ice(Fraedrich *et al.*, 2005; Fraedrich, 2012). The latter is used by default.

For more information about PlaSim, including its use and editable parameters, please refer to the Appendix A

2.2 Experimental Set-Up

As mentioned earlier in the Introduction, the main objective of this thesis is to systematically remove individual continents one at a time and examine the consequent impact on the global temperature of an Earth-like planet. This experimental process requires adjusting various parameters within the PlaSim model.

2.2.1 Model optimization and accuracy

Due to the extensive number of planned experiments, the initial step involved a thorough review of parameters influencing the optimization and precision of simulations. These parameters, encompassing the number of cores, chosen resolution, and runtime of simulations, are easily modifiable in the graphical user interface. Since these variables are interconnected to some extent, the first set of experiments primarily focused on a general exploration of these parameters.

Fraedrich (2012) performed simulations lasting 100 years using the same model to ensure numerical equilibrium. The last 30 years of these simulations were utilized for the climatological study to avoid transient states. Following this strategy simulations were conducted over 120 years to ensure comprehensive results. Additionally, the last 30 simulated years were subjected to detailed analysis.

- Land-sea interaction

  To ensure the correct interaction between ocean, ice, and atmosphere in the model, the command 'NFLUKO' must be added in the namelist files 'icemod' and 'oceanmod', changing the base number from 0 to 1 (Nowajewski, 2018).

- Spatial Resolution

  A parameter to consider is the resolution used in this project. The model simulating interactions among atmospheric, geological, and astronomical factors divides the planet into grids, where the resolution dictates the number of latitudes and longitudes. A higher resolution implies more grids, leading to smaller areas or more pixels per mask. There are 3 resolutions accepted by PlaSim (Fig. 2.1 and Appendix A for details).

  All resolutions were tested against the real data for comparison sourced from the NOAA website [2], which provides the global monthly average temperatures between the years 1901 and 2000 (Fig. 2.2).

  All three resolutions exhibit differences from the real data. It is necessary to remember that the model used simulates oceanic movements and heat transfers with an ocean depth of 50 meters, which, although useful for a model of intermediate complexity, can

[2] https://www.ncei.noaa.gov/access/monitoring/global-temperature-anomalies/mean

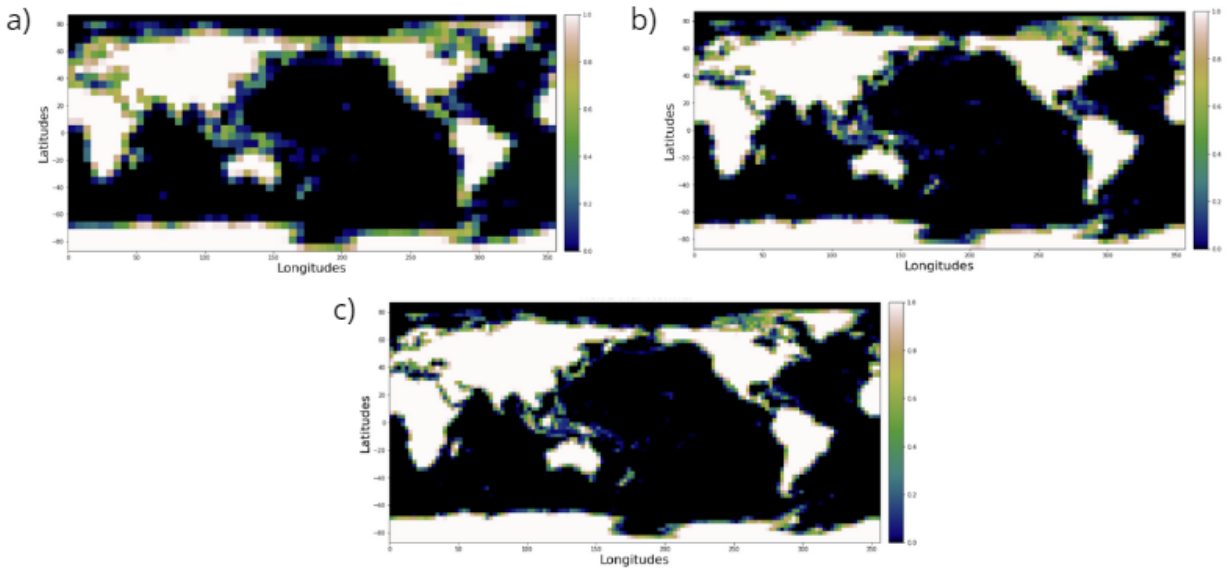

Figure 2.1: Land-Sea Mask in a) Low Resolution, b) Medium Resolution, and c) High Resolution.

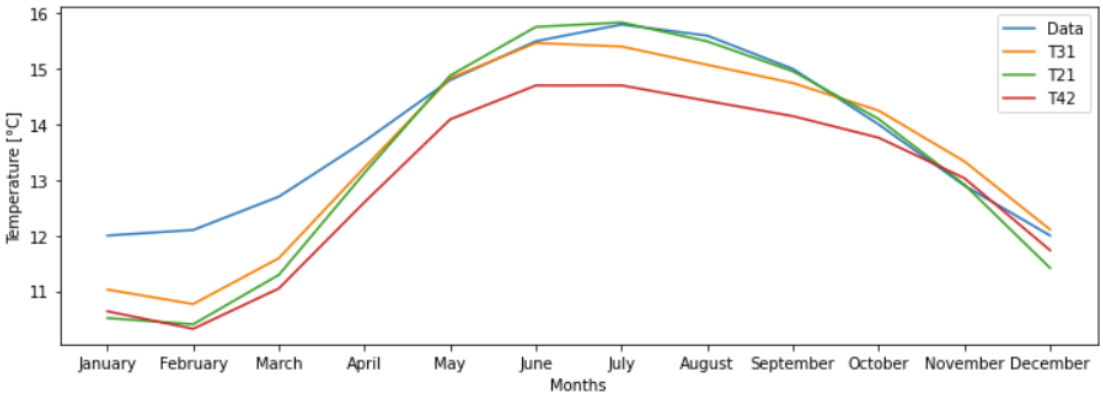

Figure 2.2: Comparison between the real data obtained from NOAA and simulations conducted at the three different resolutions

result in variations from real-world data as the ocean significantly influences temperature.

Surprisingly, the highest resolution displays the largest difference from the real data, and considering its longer execution time, it was the first option to be discarded.

Conversely, the low and medium resolutions provide similar data. Either of these resolutions could be chosen for the present project. Considering that the medium resolution offers more details in the grids and that it takes only 2 min longer per simulation year than the low resolution, we decided to use the medium resolution for all subsequent simulations.

- Stabilization period

Utilizing the data derived from the previous experiment, we analyzed the numerical stability of the model, as illustrated in Figure 2.3. The results indicate that after 40 years of simulation, the model begins to produce more consistent surface temperatures. Following the methodology of Fraedrich (2012), we opted for 100-year simulations, focusing on the climatology of the last 30 years. This aligns with the conventions of the World Meteorological Organization[3] (WMO) and the National Oceanic and Atmospheric Administration[4] (NOAA) in the United States, which typically adopt 30-year periods for defining the average climate. This duration provides a sufficiently extensive window to mitigate short-term variations and unveil broader weather patterns.

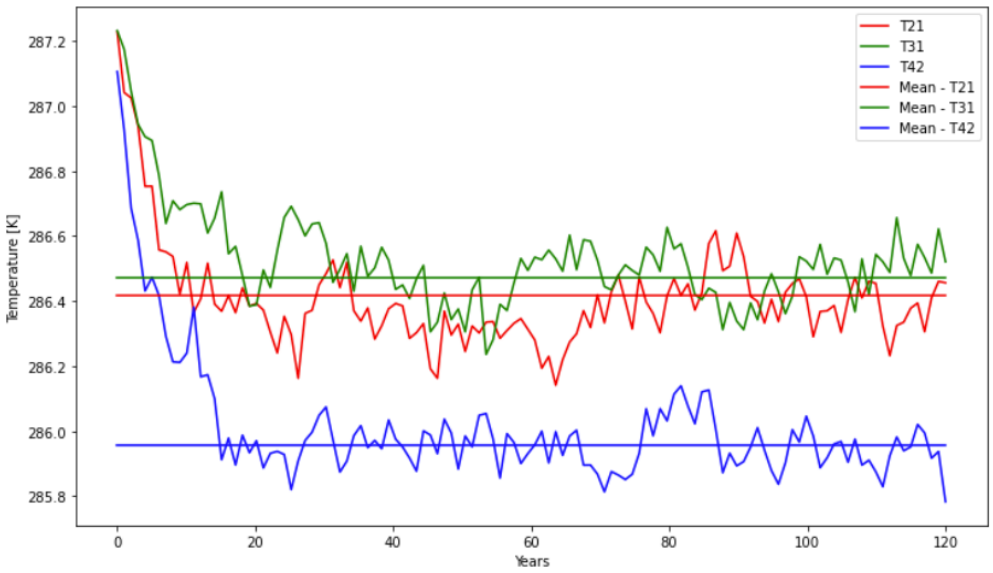

Figure 2.3: Comparison between the resolutions considering their mean value.

[3] https://wmo.int/topics/climate
[4] https://www.noaa.gov/education/resource-collections/climate

- Number of cores

  Once the resolution and simulation years were determined, the last parameter to be defined was the number of cores to be used. To get a more complete understanding of how many of the 32 possible cores to choose, we analyzed how long it took the simulator to run one year of simulation with 14 different numbers of cores (Fig.2.4).

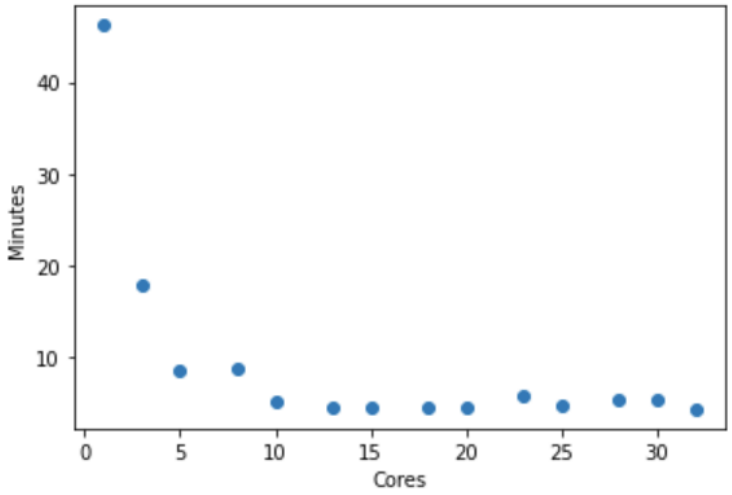

Figure 2.4: Execution time per core at medium resolution

  it is possible to note that after 10 cores, the time required became relatively stable. Considering system stability and CPU load, it was determined that performing the simulations with 16 cores was an optimal choice.

- CO_2

  Another parameter that could be adjusted via the graphical user interface (GUI) was the amount of CO2. In line to study an Earth-like planet, the CO2 concentration was set at 400 ppm, reflecting the level of carbon dioxide observed on Earth in 2015 as reported by the Mauna Loa Observatory in Hawaii[5](Figure 2.5).

- 'namelist' files

  Within the system, we encounter several files bearing the label 'namelist,' each containing critical information about the internal configuration of the planet, which was previously established in the graphical user interface (GUI). A file to highlight is 'plasim_namelist,' which required modification. To ensure consistency in output data, provided in monthly averages, we adjusted the parameter 'N_DAYS_PER_YEAR.' The standard value of 365 days was changed to 360 days, simplifying the calendar to 12 months of 30 days each. This adjustment facilitates the comparison of monthly averages, ensuring uniformity in

[5]`https://gml.noaa.gov/ccgg/trends/`

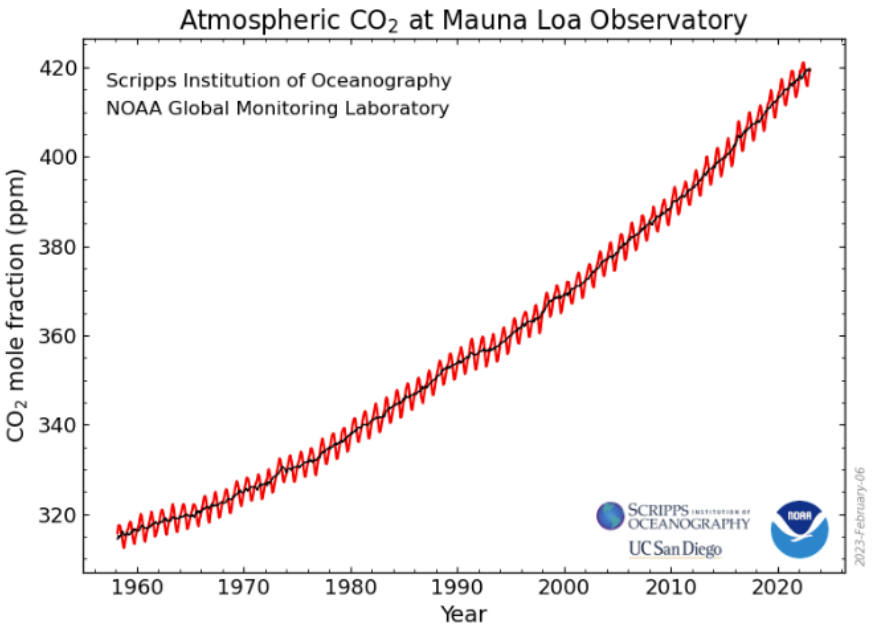

Figure 2.5: Atmospheric CO_2 at Mauna Loa Observatory.

the number of days.

On the other hand, as previously mentioned, the 'NFLUKO' parameter had to be added to the 'icemod' and 'oceanmod' namelists, where a value of 1 was set. To see how the final modifications of these files look like, see Appendix A

- '.sra' files

  In the context of our experiments, we made adjustments to a total of five masks for each simulation. These modifications were divided into two groups: masks that were uniformly modified and applied to all simulations, and masks that underwent unique alterations tailored to each specific simulation. This careful masking procedure contributes to the precision and accuracy of our experiments.

  - Modified masks according to the simulation
    - Surf. Geopotential Orography:

      This grid is in geopotential height measurements, so, as the objective is to extract territory. We proceeded to set to 0 $[m^2/s^2]$ the height of all the land we would like to extract, that is, set it to sea level.
    - Surface Roughness Mask:

      Surfaces possess not only geopotential height but also roughness. The mask containing Surface Roughness information must be modified accordingly.

      Surface Roughness, measured in meters [m], should be set to 0 [m] when extracting the terrain.
    - Land-Sea Mask:

The surface mask containing land-sea distribution data is one of the most crucial masks to modify. In this context, a value of 1 designates a pixel as 100% land, while a value of 0 signifies an entirely oceanic region. For the complete removal of a continent, the specified sector is uniformly set to 0, representing an oceanic area. This pivotal step facilitates continent extraction during our simulations.

- Masks used interchangeably

  The masks consistently modified and utilized in all simulations include number 199, containing Vegetation Cover, and number 212, providing information about Forest Cover

  These masks contain mainly information about the plant life of the planet to be simulated. As these are not variables of particular interest to us, moreover, we initially want to create lifeless planets. We proceeded to remove the vegetation of the planet. This corresponds to putting the number '0' in all points of the grid.

- Important masks not modified

  * Surface Temperature

    During multiple tests, it was found that surface temperature is correlated with information within the surface masks. As a result, adjustments to surface temperature were generally unnecessary unless specific modifications were made, such as ice removal. In such cases, a temperature above the freezing point, 273.15 K in the case of PlaSim (Dahms *et al.*, 2011), was applied. These adjustments were primarily made to ensure that surface temperature did not inadvertently influence the formation of new ice.

  * Albedo

    The albedo, or reflectivity of the surface, is automatically adjusted based on the type of surface initially specified as the simulation's starting condition. This automatic adaptation accounts for whether the surface is land, ocean, sea ice, or glacier. Therefore, there's typically no manual modification required for albedo.

To analyze the impact of different continental configurations on the climate, two sets of simulations were conducted: one with the current amount of sea ice and another without sea ice as the initial condition.

Chapter 3

Multistability of the climate

3.1 Context

The evolution of Earth has been extensively studied, and while not all details are known with certainty, there are well-established concepts regarding its development.

Numerous studies and discoveries suggest that our planet experienced global glaciation events in its history (Hoffman and Schrag, 2002), leading to extremely cold and dry conditions where a significant portion of the Earth's surface was completely frozen. These glacial episodes, known as Snowball Earth, are believed to have occurred for a limited period. This raises questions about the stability of these glaciation states and the factors that contribute to their onset and termination.

In the case of constant solar irradiance, long-term temperature regulation on Earth is primarily controlled by the carbon cycle. Carbon dioxide present in the atmosphere is removed through processes such as rainfall, which leads to its incorporation into rocks as carbonates through weathering. These carbonates eventually become deposited in the Earth's mantle, where they may undergo geological processes and return to the atmosphere over long timescales (Sleep and Zahnle, 2001; Pierrehumbert, 2010; Paradise *et al.*, 2019).

The carbon cycle plays a crucial role in the dynamics of snowball states, and its temperature sensitivity is a key factor. During snowball episodes, the low temperatures inhibit the weathering process, preventing the removal of carbon dioxide from the atmosphere. As a result, CO_2 accumulates in the atmosphere, leading to a greenhouse effect that causes the planet to warm up and initiate the melting of snow and ice. This, in turn, allows the weathering process to resume and remove CO_2 from the atmosphere, leading to a cooling effect (Pierrehumbert, 2010).

The availability of prior knowledge and the advancement of computational tools have facilitated extensive studies of snowball states. It has been discovered that, under identical levels of sunlight and CO_2, a planet can exhibit both snowball conditions and warmer states. This finding suggests that the climate system may exhibit bistability, meaning it can exist in multiple stable states depending on initial conditions and feedback mechanisms

(Pierrehumbert, 2004). This realization has further fueled research into understanding the factors that determine the transition between snowball and non-snowball states and the underlying mechanisms that drive bistability in the climate system.

3.1.1 Solar Irradiance

The study conducted by Lucarini *et al.* (2010, L10, hereafter) investigated the effect of varying irradiance on an Earth-like planet through numerical simulations. The simulations involved two states: a warm Earth and a Snowball Earth.

Figure 3.1, presented in L10, illustrates the simulation results. It shows that as the solar constant (irradiance) decreases for the warm Earth, its temperature gradually decreases. However, at a certain point around 1260 W/m^2, there is a drastic shift in temperature, and the warm Earth transitions into the Snowball state. Conversely, for Snowball Earth, increasing the irradiance leads to a gradual increase in temperature. Once the irradiance reaches approximately 1440 W/m^2, the Snowball Earth quickly transitions into the warm Earth state.

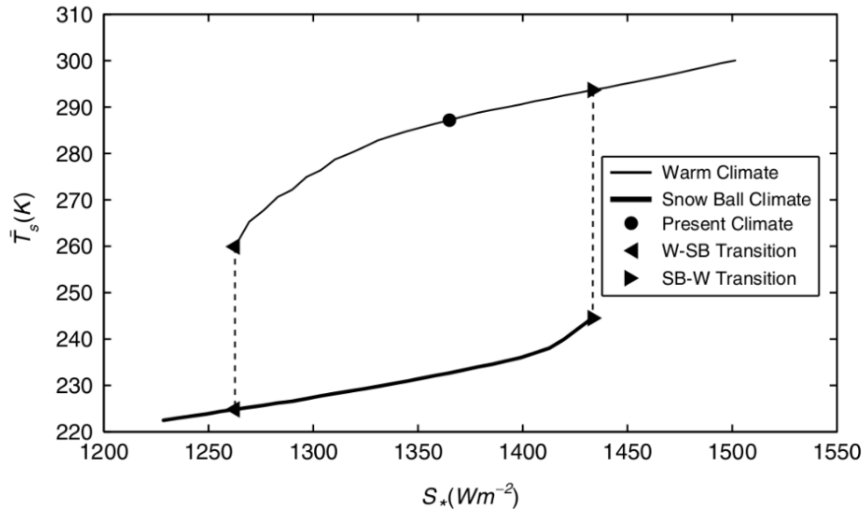

Figure 3.1: Note. Surface temperature T_s against solar constant S_*. Reprinted from "Thermodynamic Analysis of Snowball Earth Hysteresis Experiment: Efficiency, Entropy Production, and Irreversibility" by Lucarini, V. et. al, 2010, Planetary and Space Science 105, pp. 43-59

This finding underscores the significance of irradiance as a determinant of the transition between various climatic states. Furthermore, it demonstrates that different surface temperatures can be obtained under similar initial conditions solely by varying the model's initial state—either snowball Earth or warm Earth. This distinction is observable within the irradiances of 1260 W/m^2 and 1440 W/m^2, as depicted in the figure above.

3.1.2 Carbon Dioxide

In addition to studying the effect of varying irradiance, Lucarini further expanded his research by investigating the impact of varying atmospheric CO_2 levels on the climate states in Lucarini *et al.* (2013, L13, hereafter). By manipulating the opacity of the atmosphere, he explored different scenarios and discovered that instead of bistability (two stable states), there was a phenomenon called multistability, where multiple stable climate states coexisted.

Figure 3.2, presented in the follow-up study by L13 subsequent research in 2013, shows the results of these experiments. It demonstrates the existence of multiple stable climate states under different combinations of irradiance and atmospheric CO_2 levels.

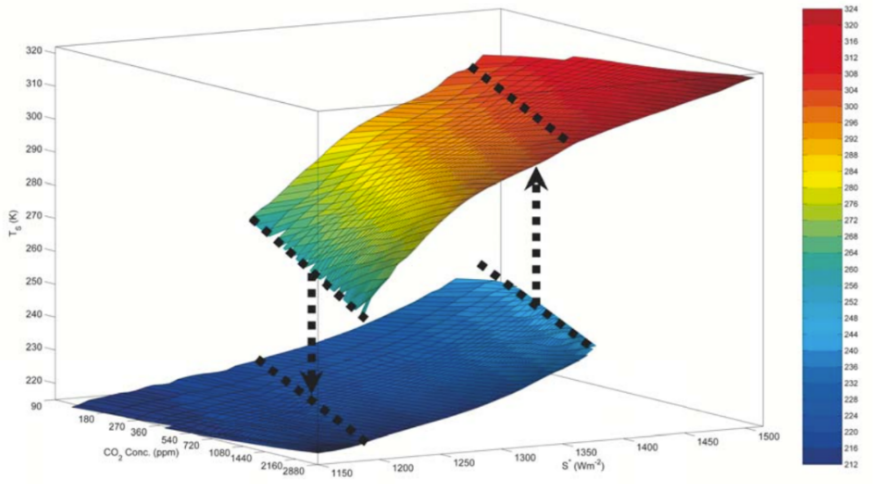

Figure 3.2: Note. Surface temperature (in K) as a function of S and the [CO_2]. Reprinted from " Habitability and Multistability in Earth-like Planets" by Lucarini, V. et. al, 2013, Astronomische Nachrichten 334, pp. 576

Following L13 groundbreaking findings, other studies delved into understanding the thermodynamics underlying these climate states. For example, Boschi *et al.* (2013) studied more about bistability in planets in the habitable zone, while Linsenmeier *et al.* (2015) expanded the investigation by considering additional factors such as variations in the planet's eccentricity and obliquity.

The collective efforts of these studies have significantly contributed to our understanding of the complexities of climate dynamics and the factors influencing climate stability.

3.2 Multistability depending on initial sea ice

3.2.1 Intermediate States

To explore intermediate states between a Snowball planet and an Aquaplanet, a series of experiments was conducted, drawing inspiration from the work of L13. Instead of varying atmospheric CO_2 levels, the amount of initial sea ice was manipulated in an aquaplanet while keeping the CO_2 concentration constant at 400 ppm. The eccentricity and obliquity of the planet were set to 0°, as in L10 and L13 studies.

Five different planet configurations were examined in this experiment. The first corresponds to an Aquaplanet, where the entire planet is covered with liquid water. The second represents a Snowball Earth, characterized by complete global freezing. The remaining three experiments explore intermediate states by introducing varying amounts of sea ice. One planet was created with sea ice covering up to latitude 20° in the northern hemisphere and down to -20° in the southern hemisphere, leaving a strip of open water at the equator between latitudes 20° and -20°. Similarly, planets with sea ice up to latitude 40° and latitude 60° were simulated. The presence of continental land was not considered in any of the experiments, as the focus was on studying the direct influence of sea ice on temperature.

A total of 45 simulations were conducted using nine different radiation quantities: 0.85, 0.90, 0.95, 1, 1.05, 1.1, 1.15, 1.2, and 1.25 times the actual solar radiation. These variations in irradiance allowed for a comprehensive exploration of the different climate states and their sensitivities to changes in incoming solar energy.

The main result of the study is shown in Figure 3.3, which displays a graph depicting the surface temperature of the five different states as the irradiance varies. Several key observations can be made:

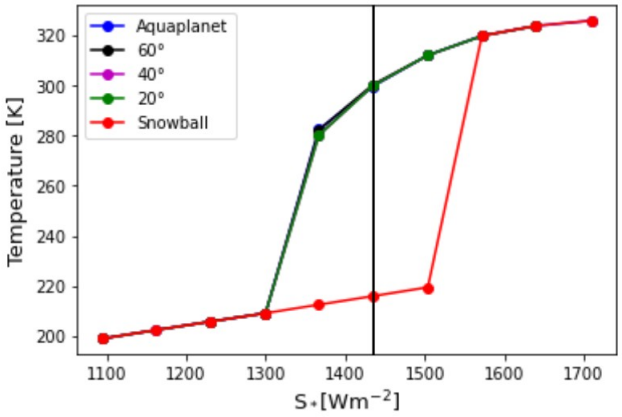

Figure 3.3: Final surface temperature of each experiment according to its solar constant. Note that between the irradiances of 1300 W/m^2 and 1500 W/m^2, the simulations with sea ice up to 20°, 40°, 60°, and Aquaplanet follow the same path. Meanwhile, the Snowball simulation follows a distinct trajectory between these irradiances and converges with the others both before and after this range. The black line represents the current sunlight.

- Aquaplanet: The temperature gradually decreases as the irradiance decreases. However, within a range of irradiance between 1298.65 Wm^{-2} and 1367 Wm^{-2}, there is a drastic drop in temperature to approximately 210 K.
- Snowball: The temperature initially rises smoothly as the irradiance increases until it reaches a range of irradiance between 1503.7 Wm^{-2} and 1572.1 Wm^{-2}.
- Bifurcation: After the bifurcation point, both the snowball state and the aquaplanet follow each other's behavior. The snowball state experiences a significant temperature increase, causing its sea ice to completely melt and behave like the initial aquaplanet.
- Transition temperatures: The transition from aquaplanet to snowball occurs at approximately 280 K, while the transition temperature from snowball to aquaplanet occurs at around 220 K. There is a difference of approximately 60 K between these transition temperatures.
- Experiments with sea ice up to certain latitudes: These experiments generally behave similarly to the aquaplanet, except near the transition to snowball. When the irradiance is equal to the current solar constant (1367 Wm^{-2}), these planets have slightly lower temperatures than the aquaplanet.

Figure 3.4 illustrates how sea ice varies with latitude according to irradiance. Key observations include:

- Current solar constant (1367 Wm^{-2}): At this irradiance level, the snowball remains completely frozen, while simulations with sea ice up to 20° and 40° generate sea ice up to approximately 40° latitude. The experiment with sea ice up to latitude 60° retains more ice, extending up to about 50° latitude. The aquaplanet transitions from a completely liquid state to generating sea ice up to approximately 50° latitude.
- Irradiance of 1435 Wm^{-2}: At this specific irradiance, two straight lines can be observed. One line with a value of 1 represents complete freezing for the snowball state, while another line with a value of 0 represents a completely liquid world for the other cases.
- Irradiance of 1572 Wm^{-2}: At this irradiance, all the experiments exhibit characteristics of an aquaplanet.
- Irradiance of 1300 Wm^{-2}: At this irradiance, all the Earth-like planets are completely frozen.

The obtained results are generally consistent with previous experiments conducted by L10 and Linsenmeier *et al.* (2015), although there may be slight differences in temperatures and irradiance values. These differences could be attributed to variations in initial parameters, such as atmospheric opacity. Nonetheless, the overall behavior and trends observed in the study align with previous findings.

The behavior of the snowball state can be understood as extreme cold temperature feedback due to high albedo. However, as weathering stops and CO_2 accumulates in the atmosphere, atmospheric opacity increases, leading to planetary warming and the melting

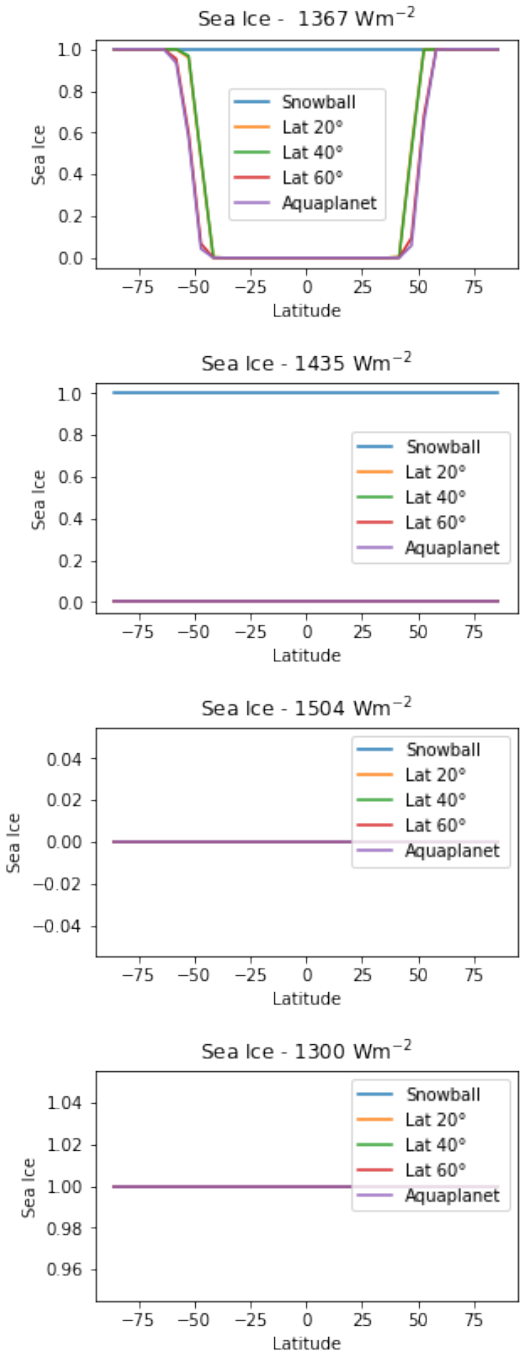

Figure 3.4: Sea Ice of selected experiment according to its solar constant

of the equatorial region. The variation in solar constant plays a role in determining the irradiance required to melt the sea ice at the equator.

In contrast, the climatic systems of the snowball and aquaplanet states differ significantly. The aquaplanet is dominated by the hydrological cycle, while the snowball state is characterized by extreme dryness and heat transport through sensible heat fluxes Boschi *et al.* (2013). This explains the lack of climatic sensitivity in the snowball state and the necessity of a high solar constant for its transition.

The experiments with initial sea ice at different latitudes exhibit similar behavior to the aquaplanet, indicating that the outcome of the planet depends on the presence or absence of ice at the equator. Therefore, the drastic temperature changes are primarily driven by what occurs in the equatorial zone. Thin sea ice may have a lower albedo than regular sea ice, leading to sunlight absorption and higher temperatures that facilitate ice melting Warren *et al.* (2002).

Furthermore, the observation that a planet with sea ice up to latitude 60° ends up with sea ice up to approximately latitude 50° is consistent with the current situation on Earth, taking into account variations in obliquity and eccentricity. This trend also applies to the aquaplanet state.

These discussions shed light on the behavior of different planetary states, their transitions, and the importance of equatorial ice coverage in determining overall climatic outcomes.

3.2.2 Current sea ice on Earth

After obtaining the results mentioned above, we wanted to investigate what occurs in the specific case of sea ice on Earth today and determine if it follows a similar trajectory as the scenario with sea ice up to latitude 60, which is considered the most similar.

By conducting 10 simulations with the current sea ice distribution while varying solar radiation, it was found that the overall path closely resembles the previous experiment, but with a notable discrepancy. That heralds the effect of continents discussed in further sections.

In the previous experiments, the bifurcation point occurred between solar radiation values of 1298.65 Wm^{-2} and 1367 Wm^{-2}. However, for the current Earth sea ice simulations(Figure 3.5), the transition took place between 1230.3 Wm^{-2} and 1298.65 Wm^{-2}. This difference suggests that the Earth's present-day sea ice distribution exhibits a distinct sensitivity to changes in solar radiation compared to the sea ice up to the latitude 60° scenario.

Notably, when the solar radiation is set to its current value, a temperature of 290K is obtained. Subsequently, with 95% of the current irradiance, the temperature drops to 276K, indicating a significant proximity to freezing conditions.

Additionally, Figure 3.6a illustrates the behavior of sea ice when the solar radiation decreases from 1367 Wm^{-2} to 1298.65 Wm^{-2}. In the southern hemisphere, sea ice forms around latitude 50°, while in the northern hemisphere, the growth of sea ice occurs more gradually with increasing latitude. Comparing these results with actual sea ice maps, it

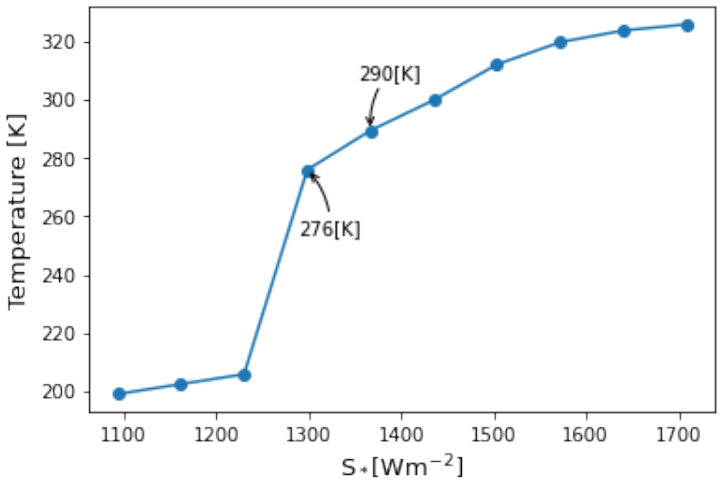

Figure 3.5: Surface temperature with current sea ice with 0 eccentricity and obliquity varying its amount of irradiance.

is observed that in the northern hemisphere, an island of sea ice begins to form between longitudes 300° and 30°, while in the southern hemisphere, the sea ice cover is more extensive, leaving only a few points of connection between the polar sea ice and the newly formed island(Fig. 3.6b and 3.6c).

The reasons behind this phenomenon, which is specific to the current Earth sea ice scenario could be attributed to the stability of the current sea ice extent and its resistance to drastic changes. It is also possible that the limitations of the model used in the study contribute to this phenomenon. Although this interesting phenomenon was not further investigated in the present work, it was acknowledged and taken into consideration in the simulations.

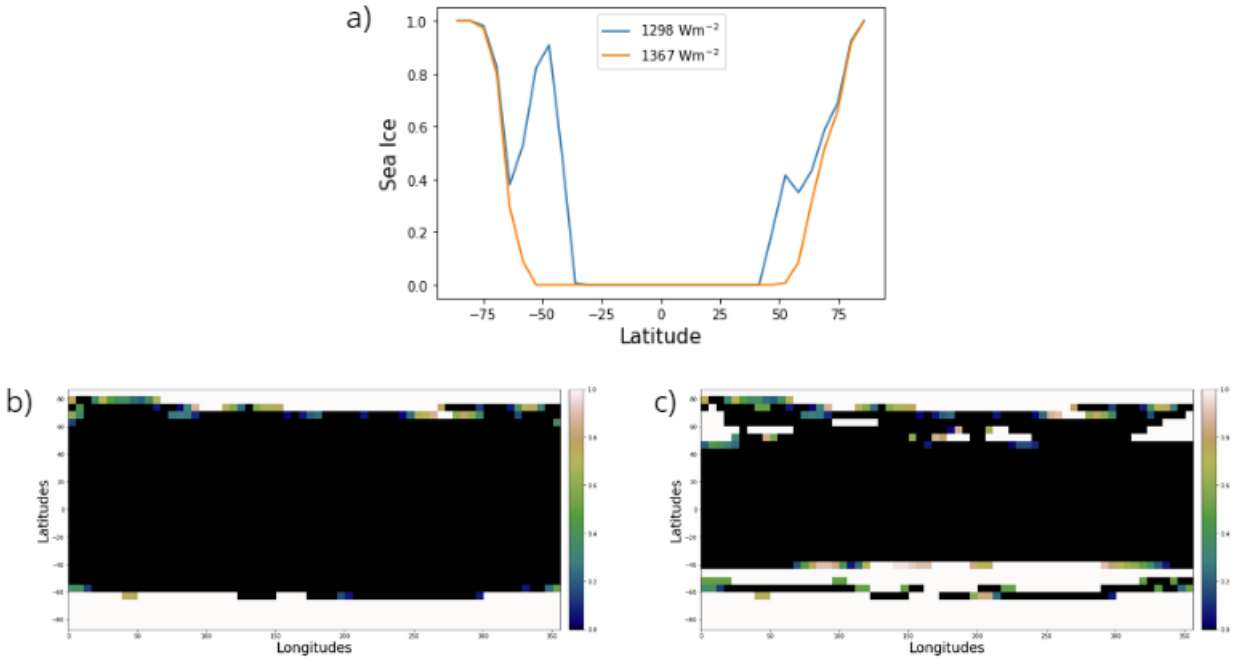

Figure 3.6: Sea ice change between an irradiance of 1367 Wm^{-2} and 1298.65 Wm^{-2} for numerical simulations conserving the Earth's current sea ice. a)Sea ice by latitude depending on the amount of irradiance, b) and c) Amount of sea ice with irradiation of 1367 Wm^{-2} and 1298.65 Wm^{-2}, respectively.

Chapter 4

Results - With Sea Ice

When starting from the current sea ice configuration, a total of 35 simulations were performed, each involving the removal of specific continents.

The following continents were extracted in these simulations:

- Oceania (O)
- Antarctica (A)
- Africa (F)
- Europe (E)
- Asia
  - North Asia (NS)
  - South Asia (SS)
- America
  - North America (NM)
  - South America (SM)

Due to the large size of Asia and America, a further division was made in the simulations. Asia was separated into North Asia and South Asia, with a division occurring at the 50°N latitude line. This division helps capture the potential differences in climate response between the northern and southern regions of Asia.

Similarly, America was divided into South America and North America. 'South America' encompasses South America, Central America, and Mexico, representing the climatic characteristics of these regions. On the other hand, North America includes all the countries in the northern part of the continent, excluding Mexico.

By separating these continents into subregions, the simulations can account for the diverse climate patterns and variations that exist within these large land masses. This approach

provides a more nuanced understanding of the continent-specific climate responses under different conditions.

For a comprehensive overview of the specific continent combinations used in the simulations, please refer to the Appendix C

4.1 Comparison between experiments

4.1.1 Surface Temperature

The main focus of this research is to investigate the impact of the amount of land on global surface temperature. A comparison was made across the entire set of simulations, considering both the temperature and the amount of land extracted.

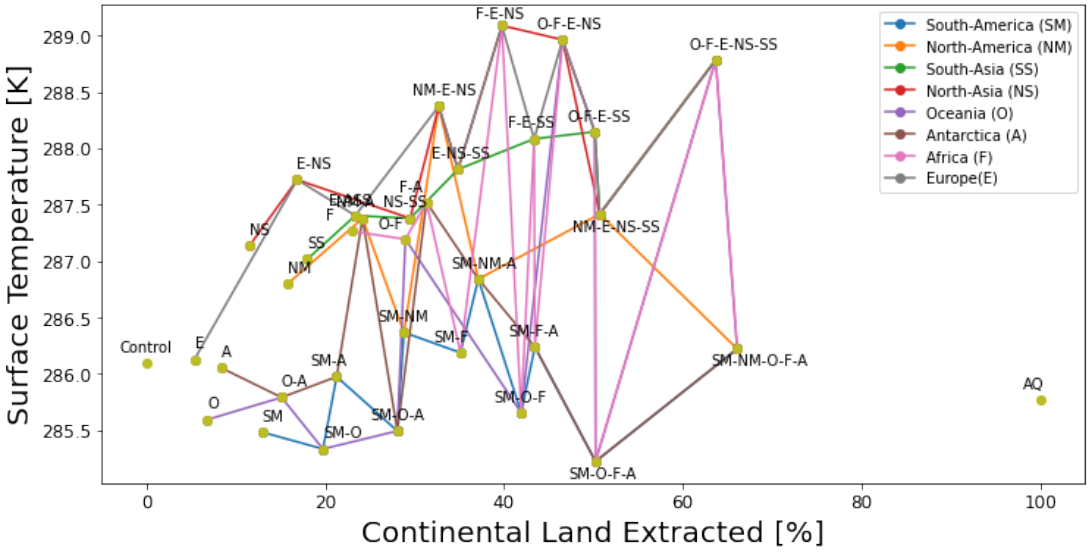

Figure 4.1: Surface temperature depends on the amount of continental land extracted relative to the current amount of continental land. The 'Control' point represents a numerical simulation that preserves all the parameters of our planet, while the 'AQ' point corresponds to a scenario where all continents have been completely extracted. Each line covers the extraction of a single continent, and the points of intersection between the lines correspond to the extraction of two or more continents. For example, the blue line follows the extraction of South America; when combined with the extraction of Oceania (purple line), The point is created that can be seen in 20% of extracted land.

The resulting image (Fig. 4.1) provides insights into the behavior of different continents concerning temperature when they are extracted. For instance, when South America is extracted, the global temperature tends to decrease, suggesting that the presence of South America contributes to higher temperatures. Similar trends are observed for Oceania.

On the other hand, continents located more centrally in the northern hemisphere, such as North America and Asia, tend to raise the global temperature when extracted. This highlights the importance of separating America into distinct regions, as the impact on temperature differs between South America and North America.

It is essential to note that each continent exhibits a unique behavior, indicating that the relationship between the amount of land extracted and temperature is not straightforward. Temperature variation is influenced more by the positioning of the landmass than its quantity.

4.1.2 Albedo

Another important factor that can be studied in contrast to the amount of extracted land is albedo.

Unlike global surface temperature, planetary albedo is not a parameter but a variable, which is why PlaSim does not provide it in the output data. Therefore, it was necessary to calculate it.

Planetary Albedo, also known as Bond Albedo, is the ratio of the amount of radiation reflected by a celestial body to the amount of electromagnetic radiation it receives:

$$\text{Bond Albedo} = \frac{\text{Reflected Radiation}}{\text{Incoming Radiation}} \tag{4.1}$$

Although PlaSim does not directly provide these parameters, it is possible to derive them using other parameters. One set of parameters that proves helpful in these calculations is the fluxes in a planet's radiative balance. Figure 4.2 visually represents Earth's radiative balance, offering a clear example of the fluxes we will employ in the planetary simulator.

When providing these fluxes, PlaSim uses different names and representations for each of them. Figure 4.3 illustrates a representation of the PlaSim parameter names, which will be further studied later. Given our specific focus on planetary albedo, it's necessary to concentrate on the upper boundary layer. In this particular region, PlaSim offers various energy fluxes, including:

- Top Solar Radiation
- Top Thermal Radiation
- Top Solar Radiation Upward

There is no parameter for the incident flux, but rather for the reflected flux, denoted as Top Solar Radiation Upward. Conversely, the Top Solar Radiation parameter represents the

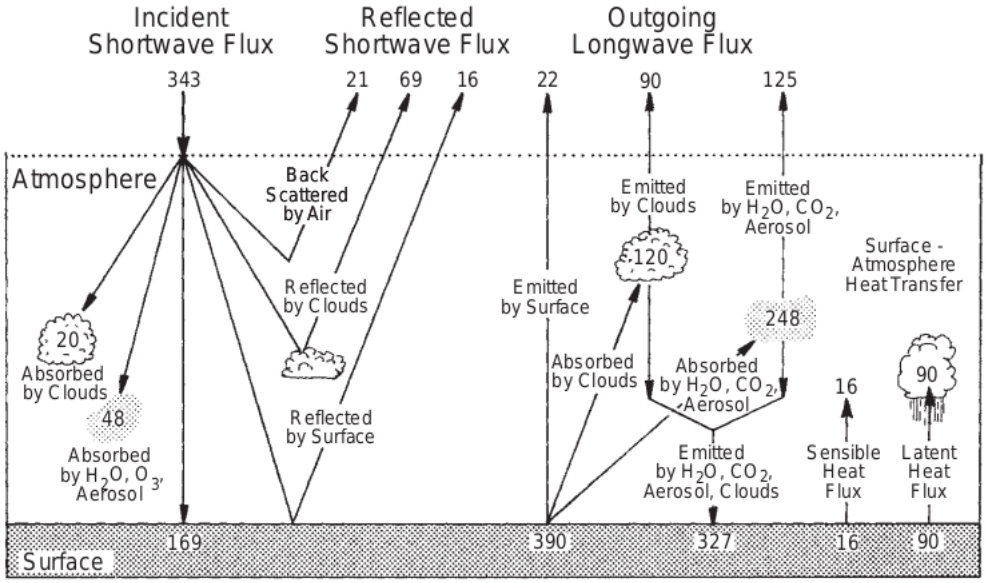

Figure 4.2: Note. Global-Mean Energy Budget (Wm^{-2}). From 'Physics of the atmosphere and climate' by Salby, Murry L., 2012, p.49, Cambridge University Press.

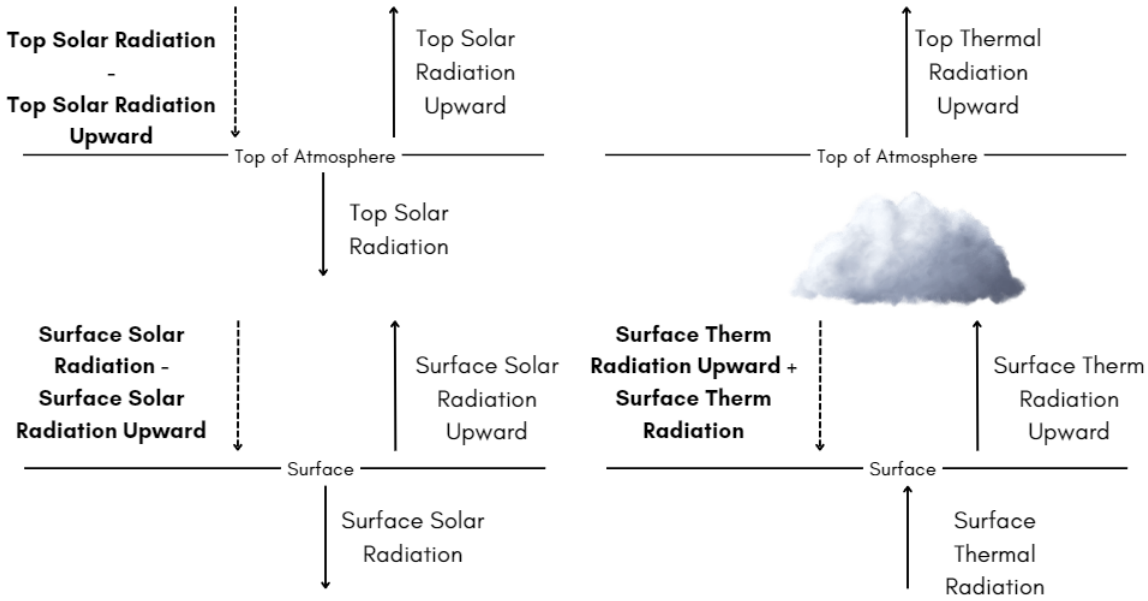

Figure 4.3: Diagram with the names PlaSim gives to the energy fluxes. The boldface and dashed lines represent fluxes that do not have their name in PlaSim, so it was necessary to calculate them.

amount of radiation that the planet does not reflect but absorbs. Therefore, we can calculate the incident radiation as the sum of Absorbed Radiation and Reflected Radiation, which in PlaSim terms would be:

$$F_{inc} = \text{Top Solar Radiation} - \text{Top Solar Radiation Upward} \tag{4.2}$$

In the Equation (4.2), we can see that Top Solar Radiation Upward (F_{TSRU}) is being subtracted instead of added in the equation, this happens because, as we will see later, PlaSim places positive values to the fluxes moving downward and negative values to those leaving the planet.

Finally, to calculate the planetary albedo in our numerical simulations, we need to compute it using the following formula:

$$A_P = \frac{-\text{Top Solar Radiation Upward}}{\text{Top Solar Radiation} - \text{Top Solar Radiation Upward}} \tag{4.3}$$

Figure 4.4 shows the global bond albedo for the different experiments. As expected, the opposite trend is observed compared to the surface temperature. When extracting SM and O, the albedo tends to increase, while extracting NM, SS, SN, and E leads to a decrease in albedo. Additionally, the planetary albedo in the scenario without continents is significantly higher than the albedo in the control point.

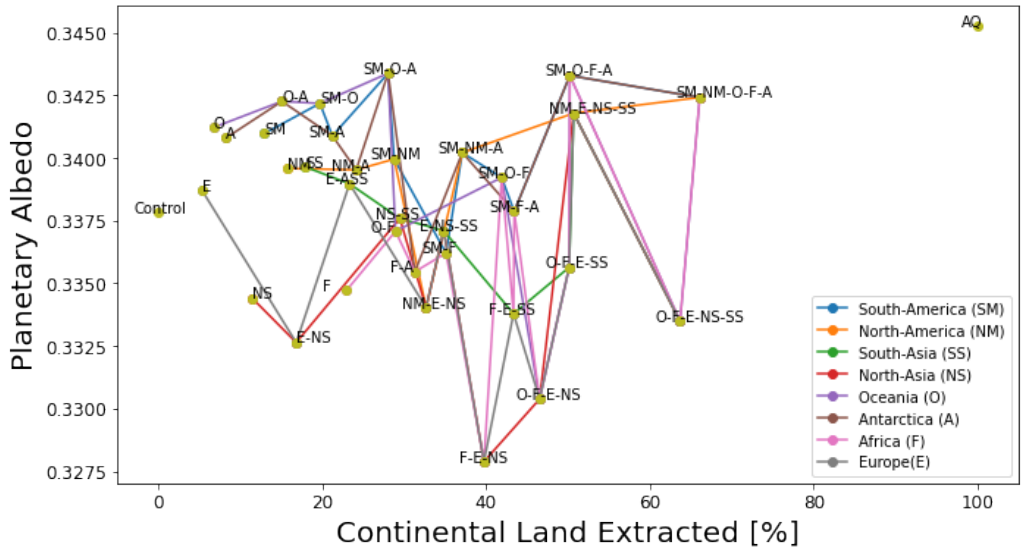

Figure 4.4: Variation of planetary albedo as a function of the amount of land extracted, displaying both the control point and the point without continent (AQ).

This relationship between albedo and surface temperature is significant(Fig. 4.5). It can be seen that the higher the albedo, the lower the surface temperature. To better explain this phenomenon, we must examine the planetary equilibrium temperature formula. This calculation is entirely theoretical (see Appendix D for details). The formula is as follows:

$$T_{eq} = \left(\frac{I_o(1 - A_B)}{4\sigma} \right)^{1/4} \tag{4.4}$$

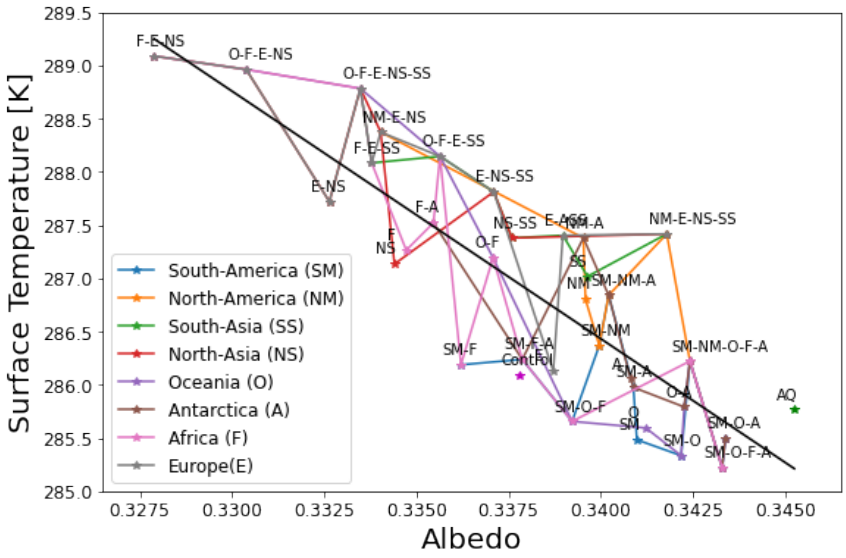

Figure 4.5: Relationship between surface temperature and planetary albedo. The black line is the linear regression of the surface temperature of the extracted continents.

In the case of our planet, the equilibrium temperature of Earth, using an albedo of 0.3 (Salby, 2012) and an irradiance of 1361 W/m^2 (Kopp and Lean, 2011), resulting in an equilibrium temperature of 254.58[K].

However, the surface temperature is around 288 K due to the presence of greenhouse gases in its atmosphere, which interact with radiation and raise the temperature of our planet. This phenomenon also occurs on other planets or moons in our solar system, with Venus being a prime example. Venus has predominantly carbon dioxide atmosphere causes its surface temperature to exceed 400 K, whereas its equilibrium temperature should be around 227 K.

Now, if we compare this information with the data provided by PlaSim, we find that in the control case with a solar constant of 1367 W/m^2 and a planetary albedo of 0.33, the equilibrium temperature would be:

$$\begin{aligned} T_{eq} &= \left(\frac{I_o(1-A_B)}{4\sigma}\right)^{1/4} \\ &= \left(\frac{1367[W/s^2](1-0.33)}{4\cdot 5.6\cdot 10^{-8}[W/s^2K]}\right)^{1/4} \\ &= 252.09[K] \end{aligned} \tag{4.5}$$

Figure 4.6a replicates 4.5 but without continental trends. In this image, two groups can be slightly distinguished, which are highlighted in Fig. 4.6b. It was primarily obtained by separating temperatures above 286.8K (Group 1 preliminary) and below 286.8K (Group 2 preliminary). Therefore, a more detailed and rigorous filtering of the groups is now required.

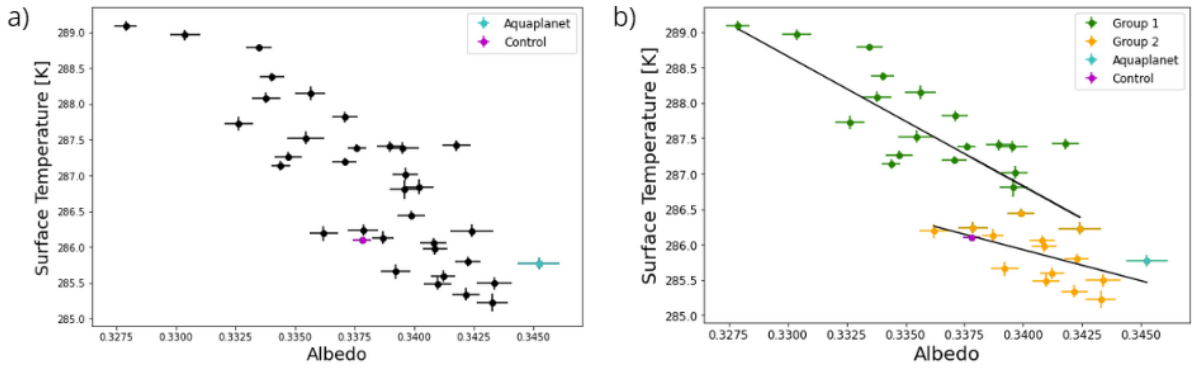

Figure 4.6: Representation of the relationship between surface temperature and albedo. a) Without separating the groups. b) The points in the figure are separated into groups based on their surface temperature, with temperatures above 286.8K and below 286.8K. Each group is shown with its respective linear regression line.

In Figure 4.7, we can observe the comparison between the extraction trend of each continent and the linear regression lines of both groups found in Figure 4.6b. It can be noted that the extraction from Asian regions, whether North Asia or South Asia, predominantly belongs to Group 1. Conversely, the extraction from South America dominates Group 2.

Regarding Oceania, Antarctica, and Africa, their data points are distributed across both groups, likely influenced by the dominant continents. In contrast, North America strongly belongs to Group 1, while Europe, although mostly associated with Group 1, is consistently accompanied by Asia. In the only instance where Europe stands alone, it falls within Group 2.

To assess the dominance of Asia in Group 1, we specifically identified simulations where some part of Asia was extracted. We then examined whether there were any other simulations near the linear regression line of Group 1. Figure 4.8a reveals that a few points did not correspond to Asia towards the end of the linear regression line. When considering the potential inclusion of North America in Group 1 (Fig. 4.8b), only three points that initially appeared to belong to Group 1 were neither Asia nor North America.

Further analysis of these points revealed that they were simulations dominated by the extraction of Africa, specifically, Africa alone, Africa combined with Oceania, and Africa combined with Antarctica. This finding suggests that, in contrast to Europe, the extraction of Africa tends to align with Group 1 but adopts the behavior of more dominant continents when combined with them.

In this way, we can now confirm the groups based on a more qualitative approach. From this point onward, we started to work with the groups separately, considering their distinct surface temperature behavior about albedo. This approach allows us to study the behavior of each group in more detail.

In part 4.9a, it can be seen that in group 1, the difference between the surface temperature and equilibrium temperature decreases as the planetary albedo increases. This suggests that

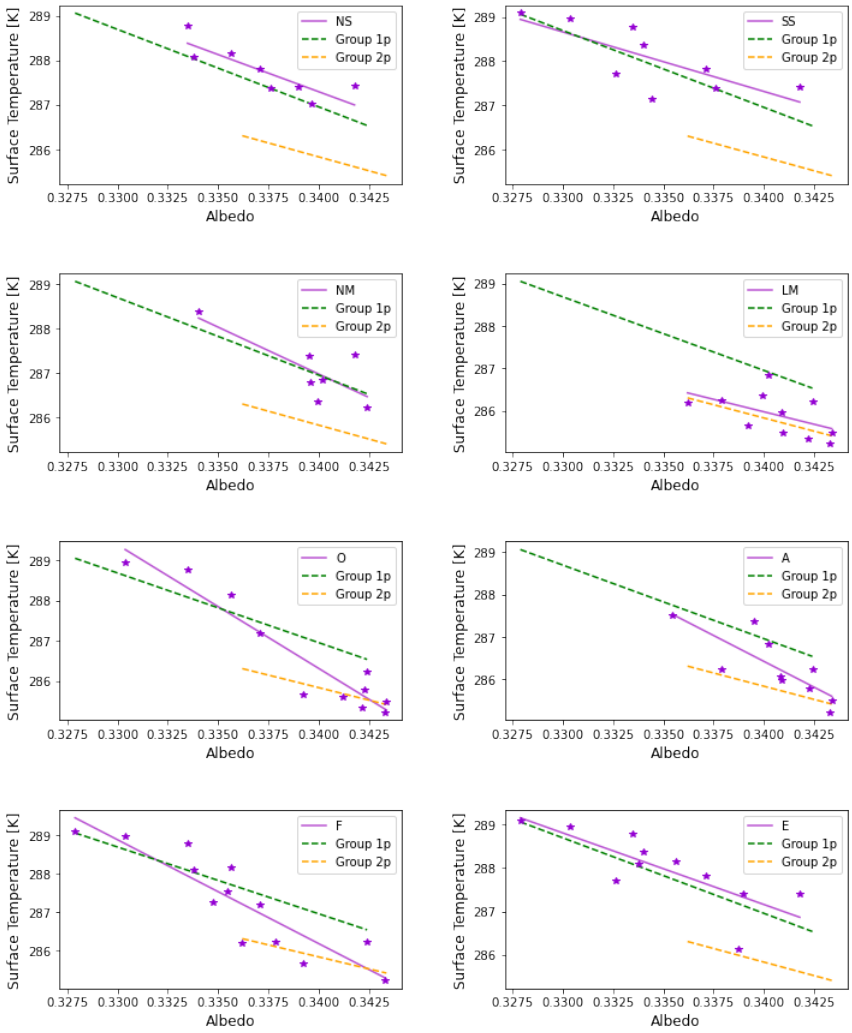

Figure 4.7: Comparison between the extraction trends when continents are extracted and the linear regression lines of the two groups. The legend in each image displays the acronyms representing the extracted continents for easy identification and reference.

as the albedo rises, the surface temperature tends to approach the equilibrium temperature.

On the other hand, in part 4.9b, we observe that in Group 2, although the temperatures also tend to converge as the albedo increases, the change is less pronounced compared to Group 1.

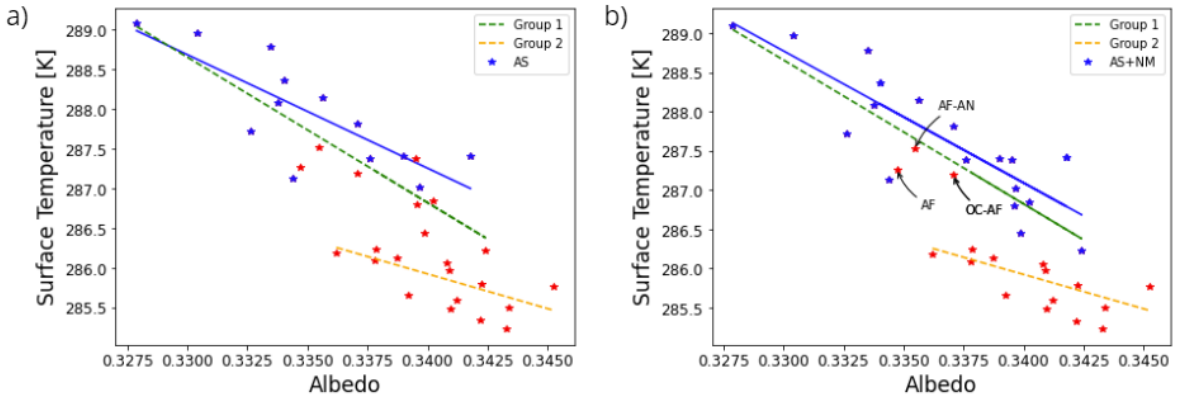

Figure 4.8: a) The experiments were divided into planetary simulations where some part of Asia was extracted (represented by blue stars) and where it was not extracted (represented by red stars). The dotted green line shows the linear regression of Group 1p, while the linear regression of Group 2p is shown as a dotted orange line. The full blue line represents the linear regression of the blue stars, indicating the overall trend of the experiments with extracted Asia. In part b), the extraction of North America was added to the blue stars. Additionally, points that remained around the initial Group 1p, even without being from the extracted continents, were marked with an arrow to highlight their proximity to the initial Group 1p.

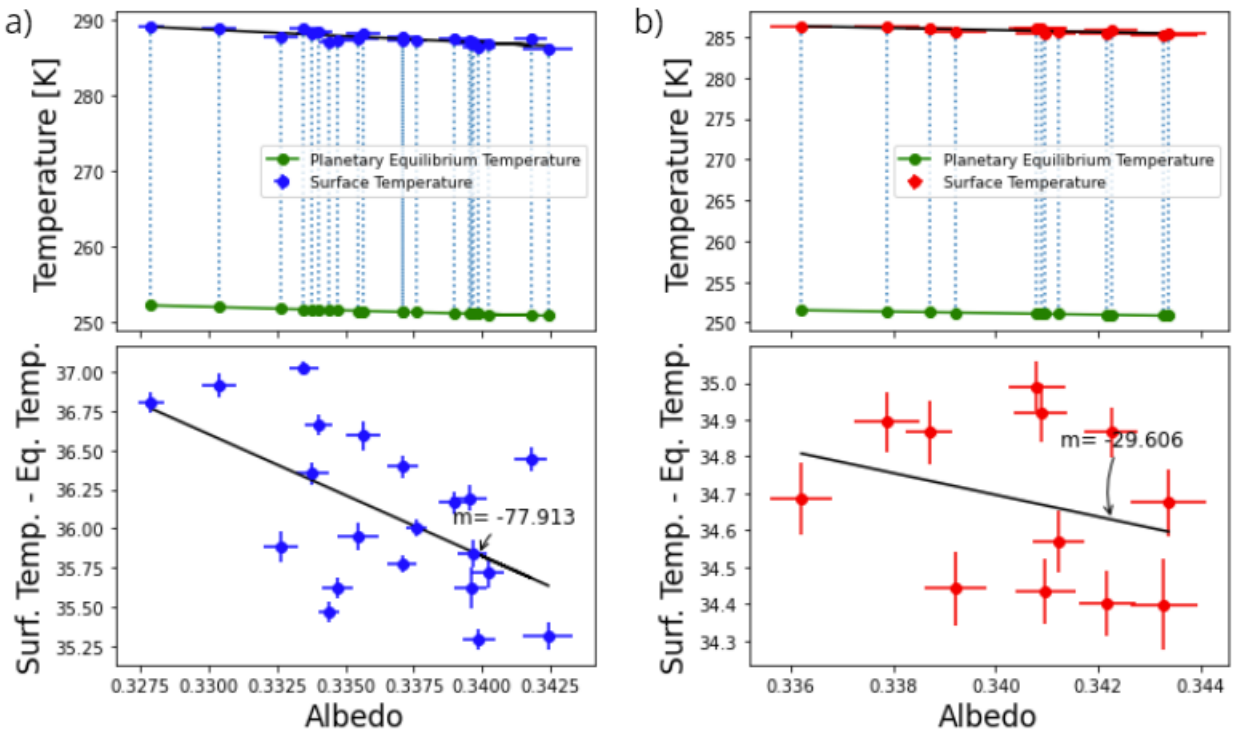

Figure 4.9: The upper graphs depict the equilibrium temperature and surface temperature for both a)Group 1 and b)Group 2. Meanwhile, the lower graphs illustrate the difference between the two temperatures and the slope of the regression line for this difference. The graphs of group 1 and 2 are comparable

4.2 Planetary Albedo

So far, we have examined the variations in surface temperature under different circumstances and established a direct relationship with the planetary albedo. Now, we will delve into the study of the planetary albedo itself.

This aspect is of utmost importance because altering the number of continents directly impacts the surface albedo in each simulation. According to PlaSim parameters, different land types have distinct albedo values. Naked soil typically has an albedo of approximately 0.2, while the albedo of glaciers falls within the range of 0.6 to 0.8. The albedo of open sea without sea ice is 0.07, and when sea ice is present, the maximum albedo reaches 0.7.

Therefore, when we convert a continent to an oceanic area, we effectively modify the albedo of the entire region from 0.2 to 0.07. This alteration affects the surface albedo and has implications for the atmospheric albedo, ultimately influencing the planetary albedo. Consequently, changing the planetary albedo leads to surface and equilibrium temperature

modifications.

As previously discussed, the planetary albedo is determined by the amount of incident solar radiation and the amount of radiation reflected into space. However, the amount of radiation reflected depends on two main factors: the reflection by the atmosphere and the reflection by the surface, represented by the surface albedo.

To comprehensively study the contributions of the atmosphere and the surface to the reflection of radiation, we need to consider the following points:

- Incident radiation enters the Earth's atmosphere and undergoes reflection and absorption before reaching the surface. The atmosphere reflects a fraction of the radiation into space while another portion is absorbed. Consequently, only a fraction of the incident radiation reaches the surface.
- Once the radiation reaches the surface, part of it is reflected into space, while the surface absorbs the remaining portion.
- The radiation reflected by the surface then interacts with the atmosphere once again. The atmosphere performs similar actions, reflecting a portion to the surface and allowing another portion to pass through. Additionally, some of the radiation may be absorbed by the atmosphere.

Therefore, the fraction of radiation reflected by the surface is entirely dependent on the initial reflection by the atmosphere. Thus, in addition to studying the impact of surface albedo, it is important to consider the consequences of the atmosphere and its contribution to the planetary albedo.

An important detail to note here is that unlike the atmosphere, where the 'atmospheric albedo' (R) is equal to its contribution to the planetary albedo (A_A), characteristic surface albedo (α) is different from the 'surface albedo contribution to the planetary albedo' (A_S, 'surface albedo' hereafter). On one hand, the characteristic surface albedo corresponds to the radiation reflected by the surface before passing through the atmosphere, while the 'surface albedo contribution' refers to the amount of that reflection that reaches the planet, contributing to the planetary albedo. In the end, we have the following relationship:

$$A_P = A_A + A_S \tag{4.6}$$

An earlier study of the contribution of both surface and atmospheric albedo to the total albedo of the Earth used the Coupled Model Intercomparison Project phase 3 and incorporated real data from the CERES experiment to compare their results (Donohoe and Battisti, 2011). Their research provided valuable insights into the albedo contributions on our planet during pre-industrial times.

Taking inspiration from the aforementioned study, we conducted our investigation into the albedo contributions within each of our experiments. We utilized a diagram similar to the one employed by Donohoe and Battisti to examine the behavior of radiation upon entering

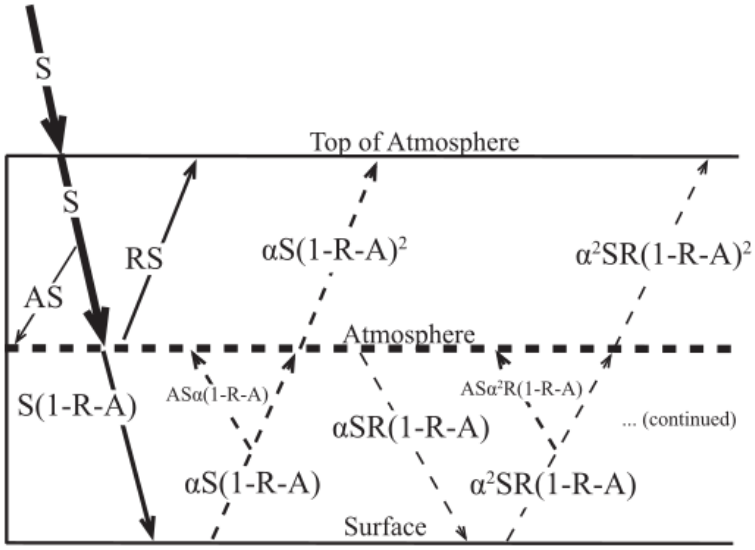

Figure 4.10: Note. Schematic representing the first two reflections in the single-layer solar radiation model. Moving from left to right, the arrows represent the radiative fluxes associated with the incident solar, first reflection, and second reflection. The variables A, R, and α are the attenuation i.e. atmospheric absorption fraction during a single pass through the atmosphere, the fraction of cloud reflection, and the surface albedo, respectively. The solid arrows at the TOA represent the radiative fluxes that we associated with cloud reflection and the dashed lines represent the radiative fluxes that we associated with the surface reflection. From 'Atmospheric and surface contributions to planetary albedo' by Donohoe & Battisti, 2012, Journal of Climate, 24(16), pp. 4402–4418

the planet(Fig 4.10). Following this diagram and the formulas developed in their study, we obtain that the total reflected radiation is:

$$\begin{aligned} F_{RT} &= SR + S\alpha(1-R-A)^2 + S\alpha^2 R(1-R-A)^2 + S\alpha^3 R^2(1-R-A)^2 + ... \\ &= SR + S\alpha(1-R-A)^2(1 + \alpha R + (\alpha R)^2 + (\alpha R)^3 + ...) \\ &= SR + S\alpha(1-R-A)^2\left(\frac{1}{1-\alpha R}\right) \\ &= SR + S\alpha\frac{(1-R-A)^2}{1-\alpha R} \end{aligned} \tag{4.7}$$

From this formula, we can obtain both the surface albedo and the atmospheric albedo. Since S is the total radiation received, we only need to do the following:

$$\frac{F_{RT}}{S} = A_P = \underbrace{R}_{A_A} + \underbrace{\alpha\frac{(1-R-A)^2}{1-\alpha R}}_{A_S} \tag{4.8}$$

Where the first part corresponds to the contribution of the atmospheric albedo (A_A), and the second part corresponds to the contribution of the surface albedo (A_S).

Therefore, to accurately study the contribution of surface albedo to the planetary albedo, we need to consider all the variables mentioned above (α, R, and A). However, PlaSim does not directly provide these parameters; instead, it offers other relevant parameters, as shown in Fig. 4.3.

Fortunately, by analyzing Fig 4.10, we can derive additional equations based on the fluxes, specifically the surface fluxes such as the incident flux on the surface (F_{IS}) and the reflected flux by the surface (F_{RS}). With these values, we can calculate the incident and reflected radiation by the planetary surface as functions of the unknown parameters. We will proceed similarly as follows:

$$\begin{aligned} F_{IS} &= S(1-R-A) + S\alpha R(1-R-A) + S\alpha^2 R^2(1-R-A) + ... \\ &= S(1-R-A)(1 + \alpha R + (\alpha R)^2 + (\alpha R)^3 + ...) \\ &= S(1-R-A)\left(\frac{1}{1-\alpha R}\right) \\ &= \frac{S(1-R-A)}{1-\alpha R} \end{aligned} \tag{4.9}$$

In a similar manner:

$$\begin{aligned} F_{RS} &= S\alpha(1-R-A) + S\alpha^2 R(1-R-A) + S\alpha^3 R^2(1-R-A) + ... \\ &= S\alpha(1-R-A)(1 + \alpha R + (\alpha R)^2 + (\alpha R)^3 + ...) \\ &= S\alpha(1-R-A)\left(\frac{1}{1-\alpha R}\right) \\ &= S\alpha\frac{(1-R-A)}{1-\alpha R} \end{aligned} \tag{4.10}$$

Now, we can calculate alpha based on the data provided by PlaSim. Performing the same procedure used in the Eq. 4.11, we obtain:

$$\alpha = \frac{F_{RS}}{F_{IS}} = \frac{-\text{Surface Solar Radiation Upward}}{\text{Surface Solar Radiation} - \text{Surface Solar Radiation Upward}} \tag{4.11}$$

We still have 2 unknowns (R and A). First, we start looking for R, for which we use F_{IS}.

$$\begin{aligned} F_{IS}^2 &= \frac{S^2(1-R-A)^2}{(1-\alpha R)^2} \\ \frac{F_{IS}^2(1-\alpha R)}{S} &= \frac{S(1-R-A)^2}{(1-\alpha R)} \end{aligned} \tag{4.12}$$

Replacing (4.7) in (4.12):

$$
\begin{aligned}
F_{RT} &= SR + \frac{\alpha F_{IS}^2(1-\alpha R)}{S} \\
F_{RT} &= SR + \frac{\alpha F_{IS}^2}{S} - \frac{\alpha^2 F_{IS}^2 R}{S} \\
SR - \frac{\alpha^2 F_{IS}^2 R}{S} &= F_{RT} - \frac{\alpha F_{IS}^2}{S} \\
SR - \frac{\alpha^2 F_{IS}^2 R}{S} &= F_{RT} - \frac{\alpha F_{IS}^2}{S} \\
R\left(S - \frac{\alpha^2 F_{IS}^2}{S}\right) &= F_{RT} - \frac{\alpha F_{IS}^2}{S} \\
R &= \frac{F_{RT} - \frac{\alpha F_{IS}^2}{S}}{\left(S - \frac{\alpha^2 F_{IS}^2}{S}\right)}
\end{aligned} \tag{4.13}
$$

Then, we can now calculate the attenuation (A):

$$
\begin{aligned}
F_{IS} &= \frac{S(1-R-A)}{1-\alpha R} \\
\frac{F_{IS}(1-\alpha R)}{S} &= (1-R-A) \\
\frac{F_{IS}(1-\alpha R)}{S} &= (1-R-A) \\
A &= 1 - R - \frac{F_{IS}(1-\alpha R)}{S}
\end{aligned} \tag{4.14}
$$

Finally, we now have all the parameters necessary to calculate the contributions of surface albedo and atmospheric albedo.

4.2.1 Contribution of atmospheric and surface albedo

In Figure 4.11a, the lines representing albedo in group 1 are not completely parallel. On the other hand, in part b of the same figure, it can be observed that there is slightly more parallelism between their lines, and there appears to be a greater contribution of surface albedo in the latter group. To study both groups in more detail, individual separations were made.

- Group 1

  In Fig 4.12, we can observe a small trend in the attenuation caused by the atmosphere on the surface albedo. Attenuation is the atmospheric absorption during a single pass

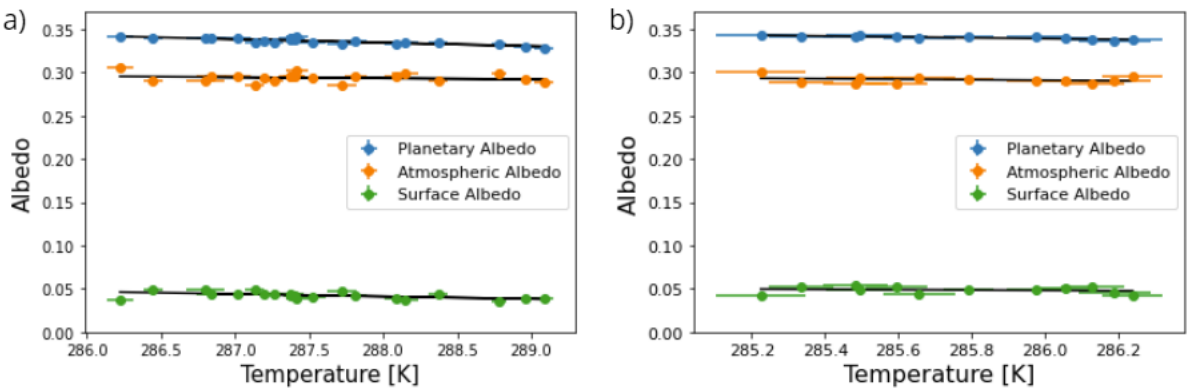

Figure 4.11: Contribution of both atmospheric albedo and surface albedo to the planetary albedo in a)Group 1 and b)Group 2

through the atmosphere. It shows that as the temperature increases (resulting in a lower total albedo), the atmosphere attenuates the surface albedo by more than 70%. Similarly, in Fig 4.12b, we can see that more than 85% of the planetary albedo is attributed to the atmosphere. It is also evident that the contribution of the atmosphere increases as the temperature increases. In Fig 4.12c, the contribution of the surface albedo is depicted, which decreases as the temperature rises. Lastly, the ratio between surface and atmospheric albedo confirms that as the albedo decreases, the atmospheric albedo increases.

- Group 2

  Contrary to what occurred in the previous case, Group 2 exhibits lines that appear to be flatter. By seeking the same proportions as in Group 1, we obtain the image 4.13.

  Initially, it can be observed that all components display flatter slopes. This suggests that altering the surface albedo in these cases does not significantly affect the contribution of each component.

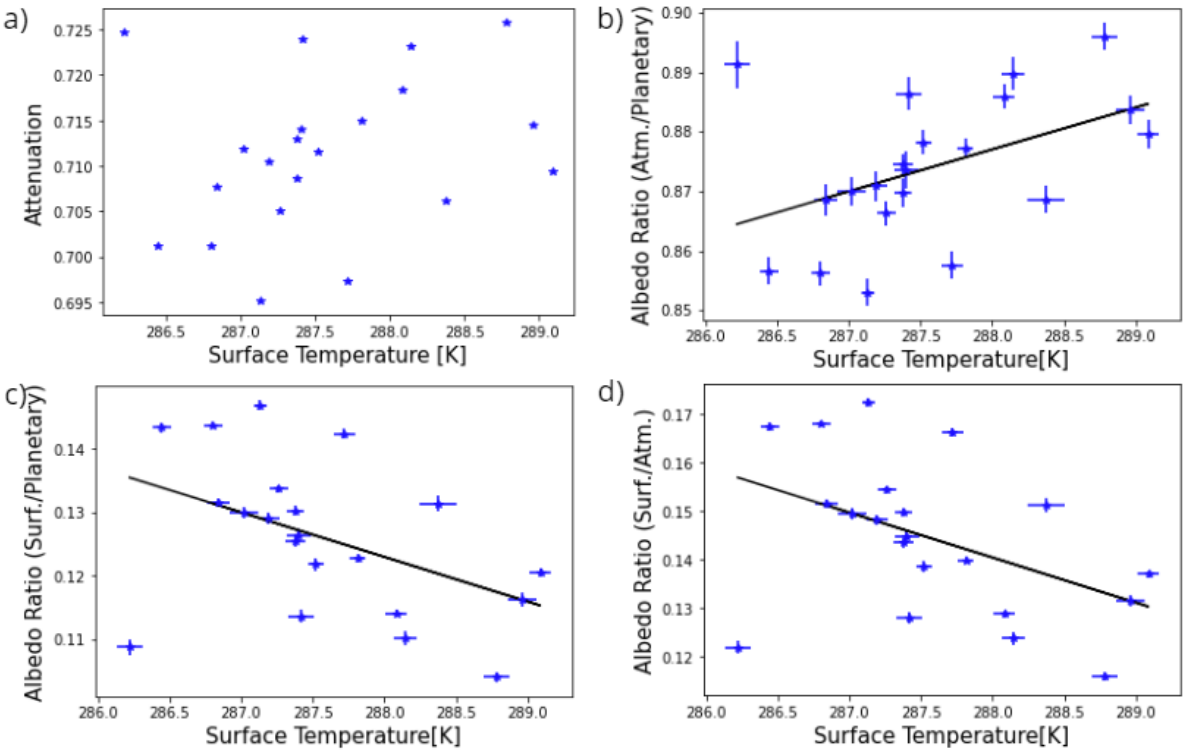

Figure 4.12: Comparison between the ratios of the different albedos in Group 1. a) Attenuation. b) Ratio of the albedo contributed by the atmosphere in the planetary albedo. c) Ratio of the albedo contributed by the surface in the planetary albedo. d) Ratio of surface albedo as a function of atmospheric albedo.

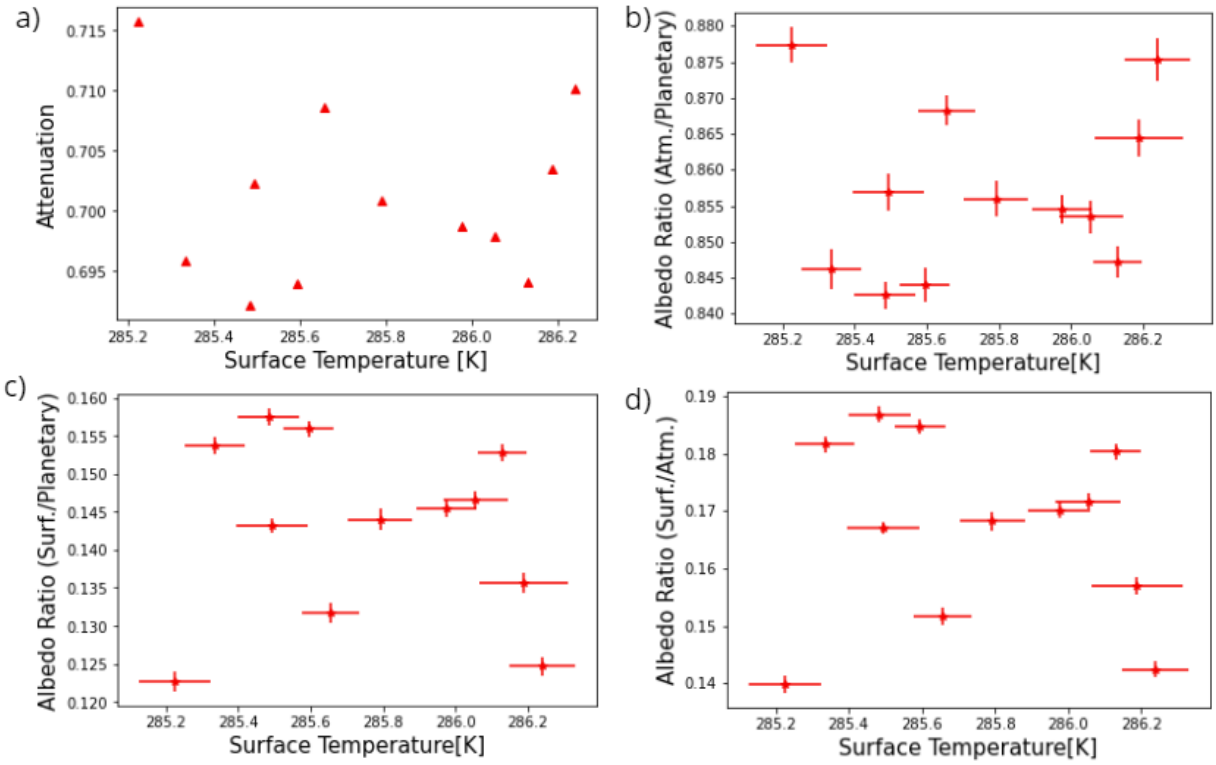

Figure 4.13: Comparison between the ratios of the different albedos in Group 2. a) Attenuation. b) Ratio of the albedo contributed by the atmosphere in the planetary albedo. c) Ratio of the albedo contributed by the surface in the planetary albedo. d) Ratio of surface albedo as a function of atmospheric albedo.

4.2.2 Contribution of surface components

To delve into the details of the contribution of albedo, we studied the components of the surface albedo in more depth. This involved examining the composition of the surface, including whether it consisted of ocean, land, sea ice, or glacier, and determining the contribution of each component to the surface albedo. To conduct this study, corresponding masks were utilized.

Firstly, the composition of each pixel was identified, distinguishing between pixels containing sea or land, as well as pixels containing sea ice or glacier ice. For instance, if a pixel had an atmospheric albedo of 85.3% and a surface albedo of 14.7%, we calculated the breakdown of the surface albedo to determine its sources. If the surface was composed of 73.3% ocean and 26.7% sea ice, it meant that 10.7% of the total albedo of that pixel originated from the ocean, while only 3.9% came from sea ice (see fig 4.14).

The fig 4.14 was performed for all pixels of the grid. Then, they were studied at the

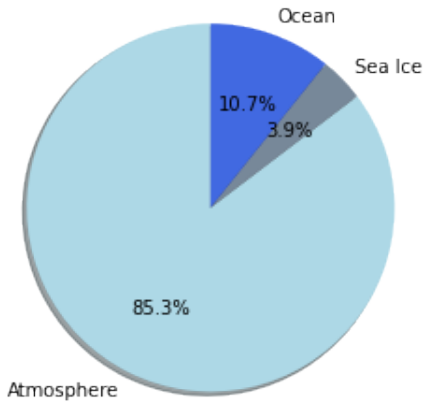

Figure 4.14: Example of how the contribution of each component to the albedo, atmosphere of each pixel was determined.

latitude level by summing contributions at all longitudes (Fig 4.15a).

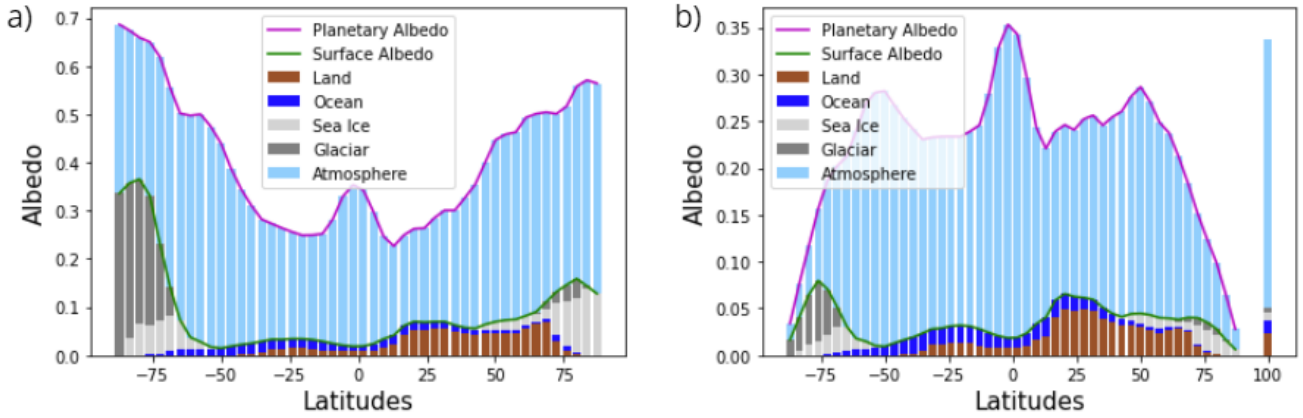

Figure 4.15: Example of how the contribution of each component to the albedo, atmosphere of each pixel was determined.

In the figure 4.15, we can observe the contrast between the graph that does not consider the sphericity of the planet and the graph that does consider it. In part 4.15a, all areas, regardless of latitude, are assumed to have the same contribution to the total area of the planet. As a result, a high albedo can be observed at the poles and the equator. Conversely, in part 4.15b, the planet is considered as the sphere that it is, taking into account the different areas of the poles and the equator. Consequently, the contribution of the poles in the total albedo is reduced, while the important contribution of the equator zone is preserved.

Now, when studying the contribution of all surface factors to the surface albedo, we obtain Figure 4.16. This allows us to compare the behavior of each group as well. In Group 1, we can observe that the albedo contributions vary as the surface temperature changes. Conversely, in Group 2, the lines remain relatively constant and do not intersect.

Finally, when examining the ratio of the albedo of all components to the surface albedo in Figure 4.17, we can observe that in the case of Group 1, continental land initially has the

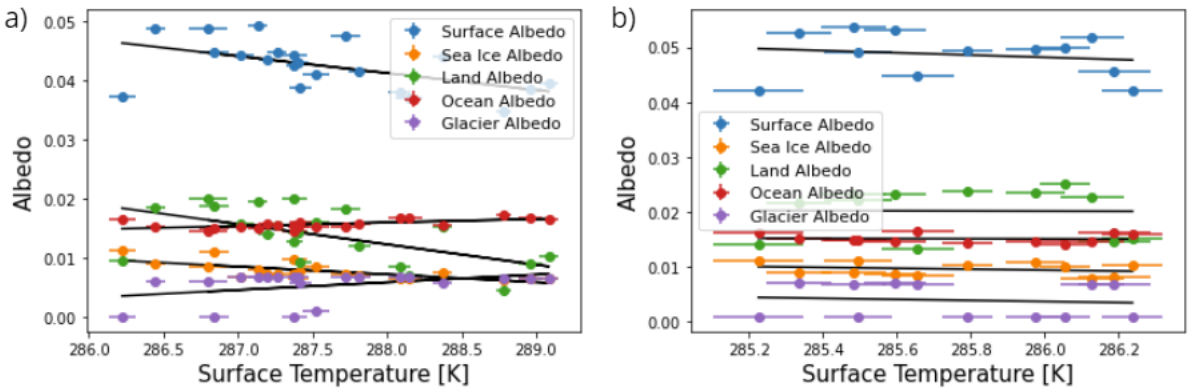

Figure 4.16: Contribution of all surface factors to the surface albedo for a) Group 1 and b) Group 2.

greatest influence, but its relevance decreases as the temperature rises. It transitions from contributing over 50% to around 20%. Conversely, ocean albedo becomes more important as the temperature rises, increasing from less than 30% in some simulations to over 45% in others towards the end of the graph. Additionally, sea ice decreases by an average of 6%, while the contribution of glaciers increases by 10%.

On the other hand, in Group 2, the proportions of albedo in all components remain relatively stable. Continental land albedo maintains a contribution of over 40%, while ocean albedo remains above 30%.

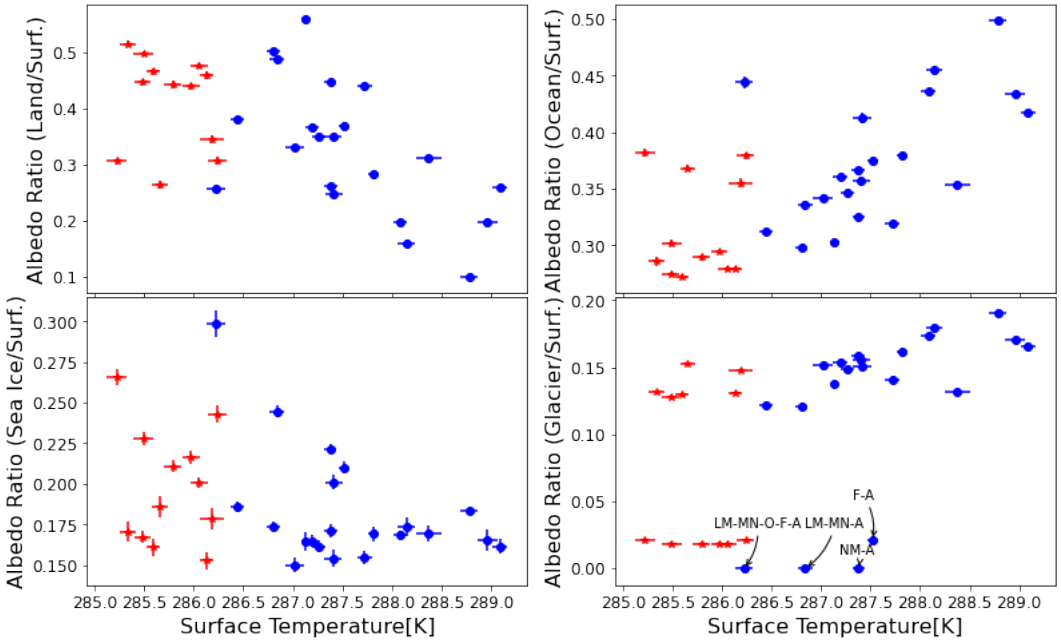

Figure 4.17: Contribution of all surface factors to the surface albedo.

Chapter 5

Results - Without Sea Ice

As discussed in §3, the behavior of the Earth differs depending on the presence or absence of sea ice in the initial conditions. Therefore, we conducted simulations following the same methodology as in the previous section, with the exception that both the sea ice and the glacial component were completely removed at the start of the simulation.

By extracting the same continents in the same manner, we aim to enable a more direct comparison between the two states in subsequent analyses.

5.1 Comparison between experiments

5.1.1 Surface Temperature

When comparing the continents as a function of the extracted landmass (Figure 5.1) no clear trend, similar to the 'with sea ice' case, is observed. However, it is still evident that the smaller the mass extracted, the smaller the variations observed between experiments with the same amount of continental soil. For instance, the temperature difference between experiments with minimal landmass extraction, such as NS and SM, is less than one degree. In contrast, experiments extracting larger landmasses, such as F-E-SN and SM-O-F, exhibit a temperature difference of more than 5 K.

On the other hand, it is possible to note that the planet that starts without sea ice or continents ends up with a significantly lower temperature compared to planets that do have continents.

Furthermore, despite the scattered points, a slight tendency towards lower temperatures can be observed.

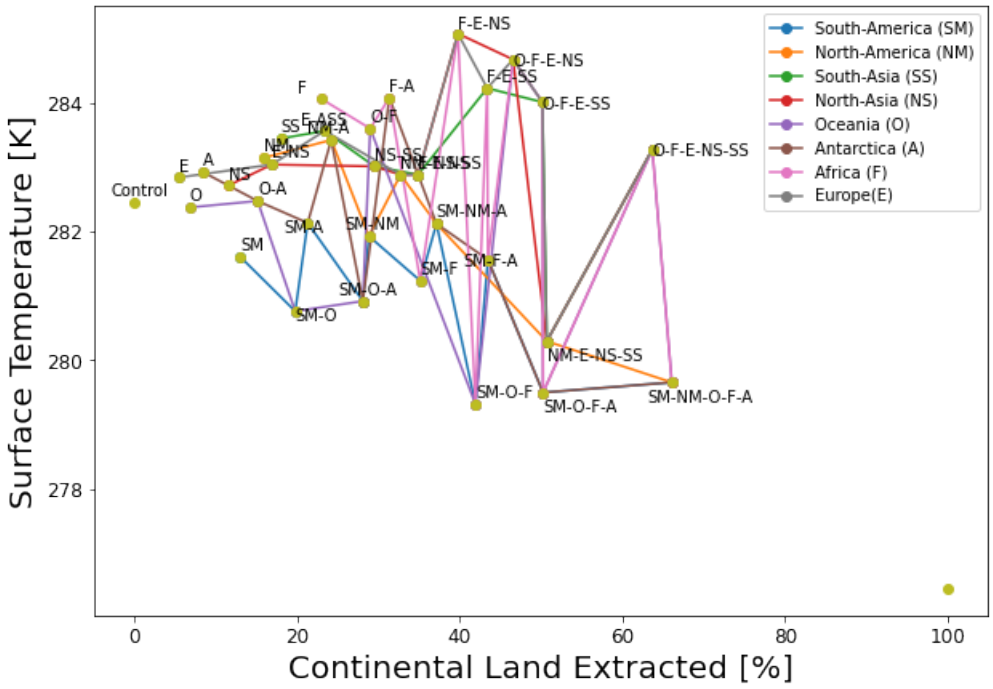

Figure 5.1: Surface temperature depends on the amount of continental land extracted relative to the current amount of continental land. The 'Control' point represents a numerical simulation that preserves all the parameters of our planet, while the 'Aquaplanet' or 'AQ' point corresponds to a scenario where all continents have been completely extracted

5.1.2 Albedo

If we now proceed to study the comparison with albedo, as represented in Fig 5.2, we observe that although there is no clear trend, it can be seen that albedo tends to increase slightly when the amount of continental land is modified.

It is also noteworthy that when Africa is removed, the albedo decreases by approximately 0.05, representing the most significant change in both experiments. However, the rest of the continents do not show significant variations when extracted individually, following a similar pattern as in the experiment 'with initial sea ice'.

Then, we observe what happens between albedo and surface temperature. We can notice (Fig 5.3) that there is a much more marked tendency. In Fig 5.3b, if we examine the points around the linear regression line, we can observe their proximity to it, indicating the well-defined nature of the trend. With a correlation coefficient of -0.959 and a coefficient of determination of 0.921, it is evident that there is a strong negative correlation between the variables, indicating a high degree of relationship and predictability between the surface temperature and the albedo in this case.

As albedo increases, the difference between the surface and equilibrium temperature decreases by almost 4 degrees (Fig. 5.4), which is larger compared to the scenario depicted

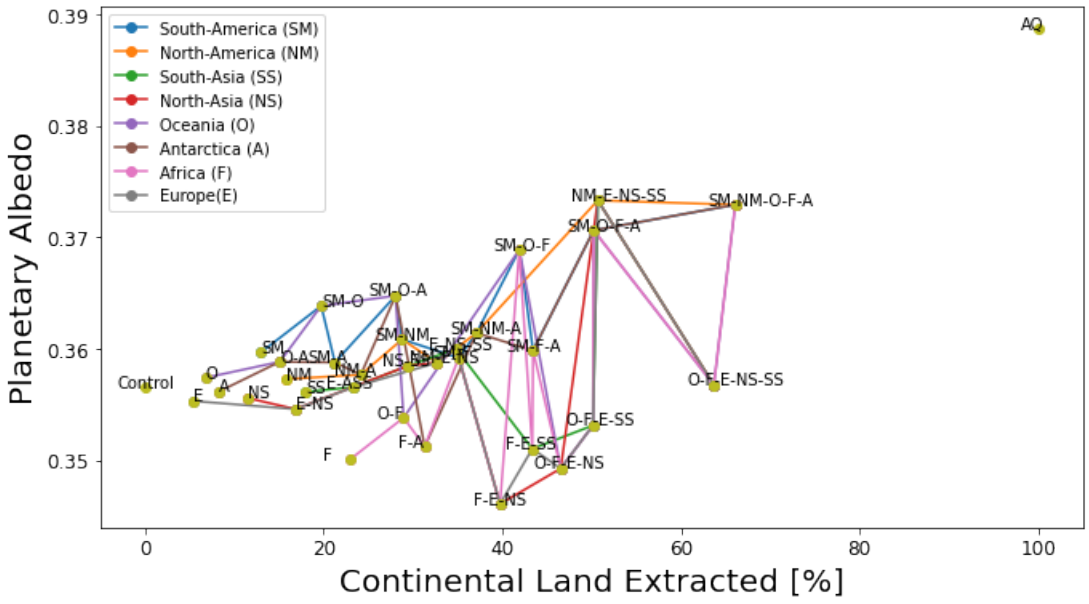

Figure 5.2: Variation of planetary albedo as a function of the amount of land extracted, displaying both the control point and the aquaplanet point.

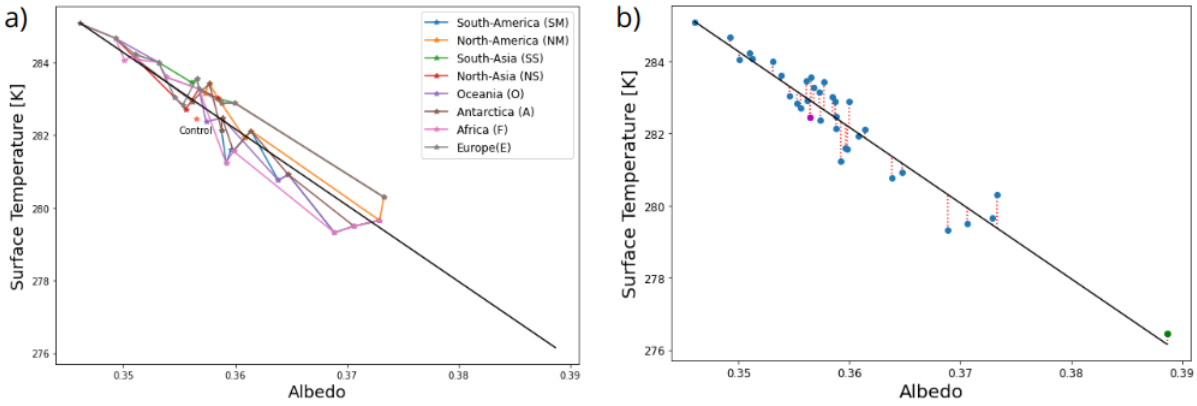

Figure 5.3: a) Shows the extraction behavior of different continents. The names of the continents were not added. b) We can see the distance between each of the points and the linear regression in black. The magenta dot represents the control, and the green dot represents an aquaplanet.

in §4 (Fig. 4.9). This observation indicates that as the planet approaches an aquaplanet state (with only oceans and no continents), the surface temperature converges towards the equilibrium temperature.

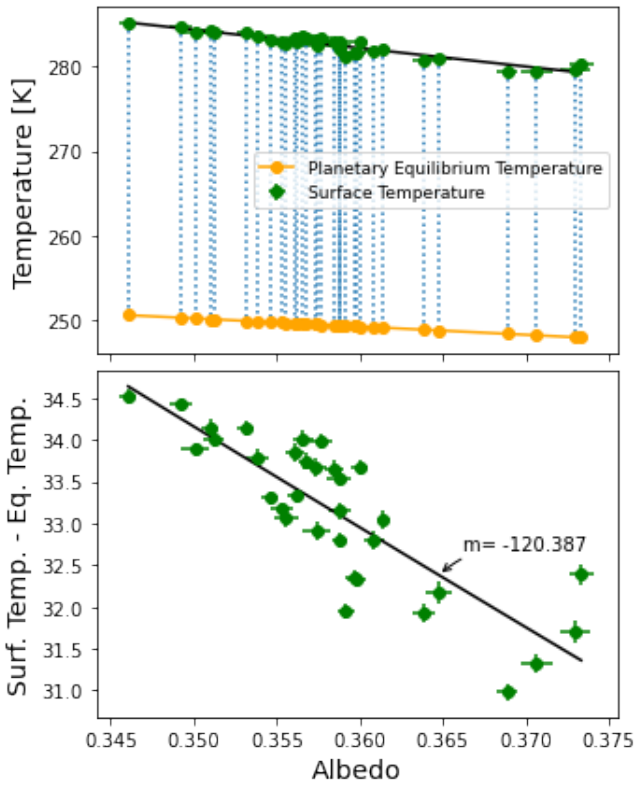

Figure 5.4: Comparison between planetary equilibrium temperature and surface temperature (c.f Fig 4.9).

5.2 Planetary Albedo

This section follows the same steps detailed in Chapter 4.

5.2.1 Contribution of atmospheric and surface albedo

It is observed that at higher temperatures, the contribution of the atmosphere is larger than at lower temperatures (Fig. 5.5a). Fig.5.5b and Fig. 5.5c show that as the surface temperature increases, the contribution of surface albedo decreases, while the contribution of atmospheric albedo increases. Similar to what happened in Group 1, the lower the planetary albedo, the higher the contribution of surface albedo, reaching approximately 18%. However, the albedo is still predominantly influenced by atmospheric albedo.

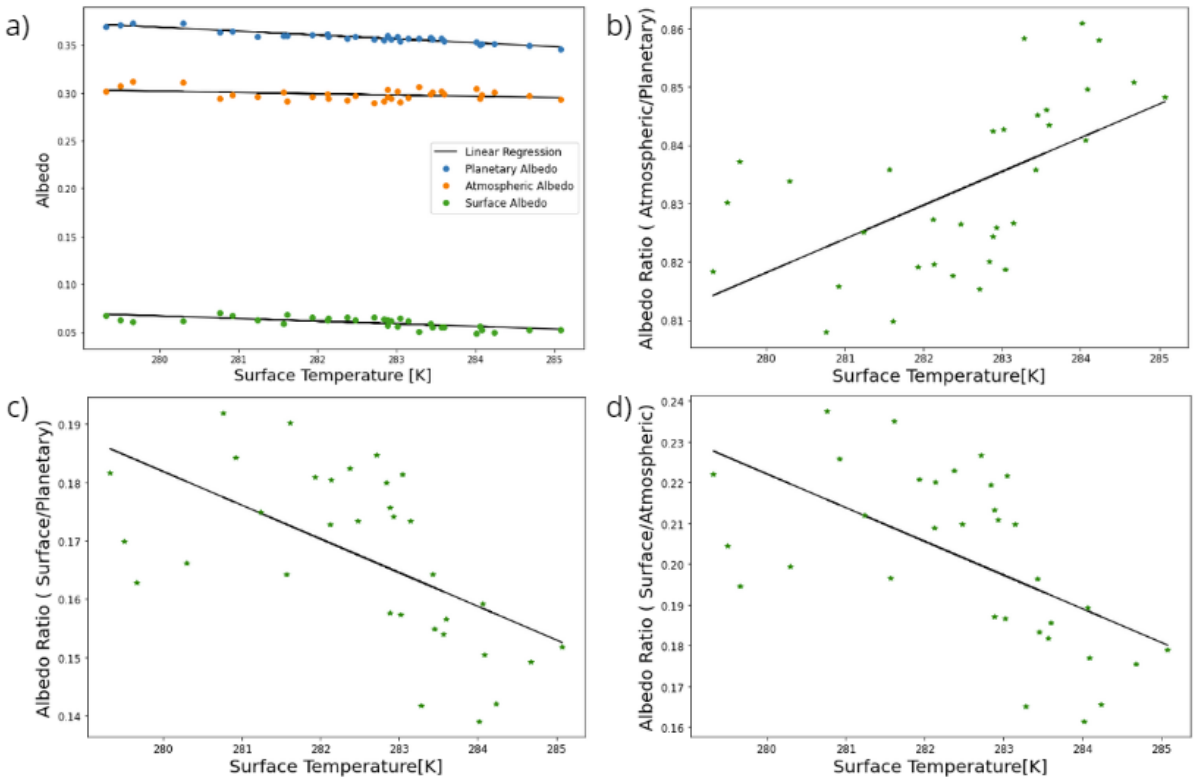

Figure 5.5: a) Attenuation. b) Ratio of the albedo contributed by the atmosphere in the planetary albedo. c) Ratio of the albedo contributed by the surface in the planetary albedo. d) Ratio of surface albedo as a function of atmospheric albedo.

5.2.2 Contribution of surface components

Now, when we examine all the surface factors that could influence the albedo(Fig 5.6), a clear pattern emerges: the surface albedo contribution decreases as the temperature rises. In broad terms, we can observe that the behavior of surface albedo aligns with the albedo exhibited by sea ice. Additionally, it becomes apparent that the ocean's contribution becomes slightly more pronounced as the temperature increases. Meanwhile, the contribution from glacier or snow-covered areas combines with that of continental land. Interestingly, in certain simulations, the impact of glaciers on surface albedo becomes more significant than that of the continental land itself.

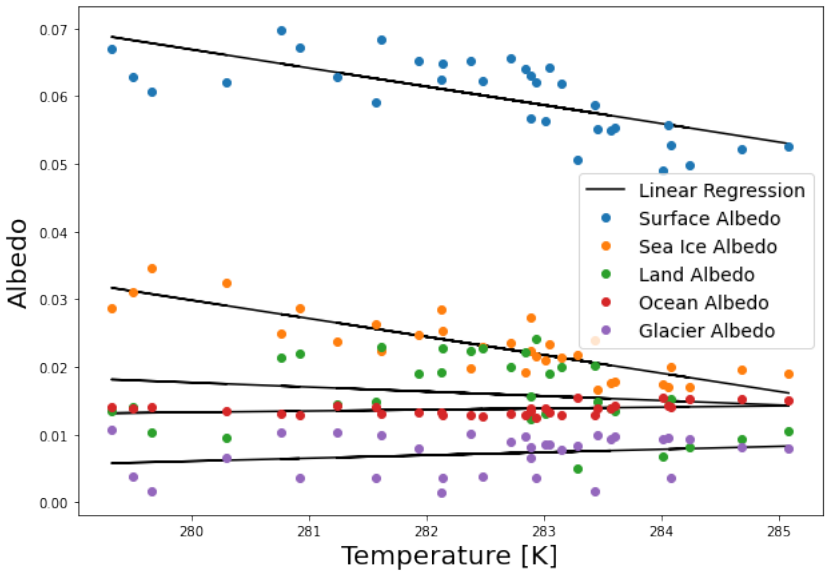

Figure 5.6: Contribution of all surface factors to the surface albedo.

Upon further analysis of the contribution of all factors to the surface albedo (Fig 5.7), we observe that the ocean contribution increases by about 0.1 relative to the surface contribution within the studied temperature range. In contrast, sea ice maintains a range between 0.3 and 0.45, except for three points at the lowest temperatures.

Moreover, the contribution of both continental land and snow lacks a definite trend, and, above all, the contribution of continental land shows a wide range, ranging about 0.4.

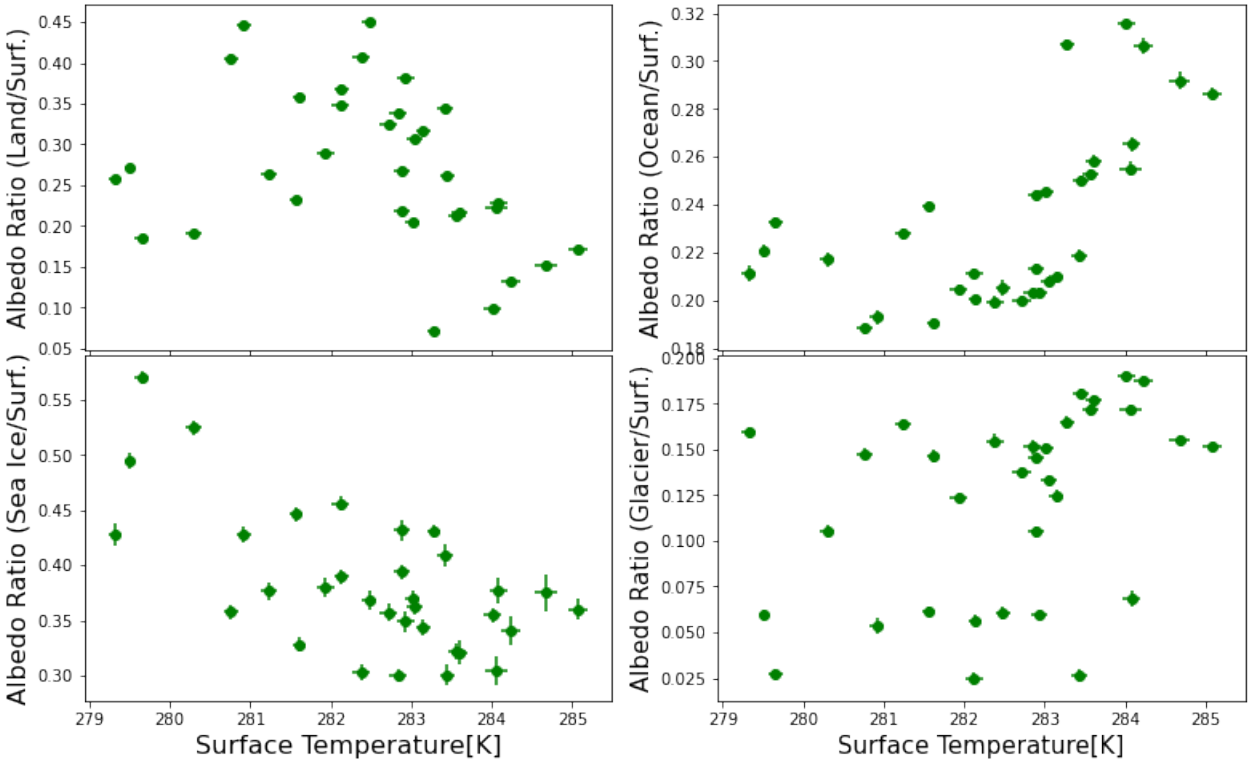

Figure 5.7: Contribution of all surface factors to the surface albedo.

Chapter 6

Discussion

6.1 Continental Land

To conduct a more comprehensive analysis of the results, a comparison will be made between the two experiments conducted in the previous sections: the experiment with the current sea ice(CSI) and the experiment without initial sea ice(WSI).

Thus, we compared the variations in surface temperature to the initial change in the amount of continental land (Fig. 6.1).

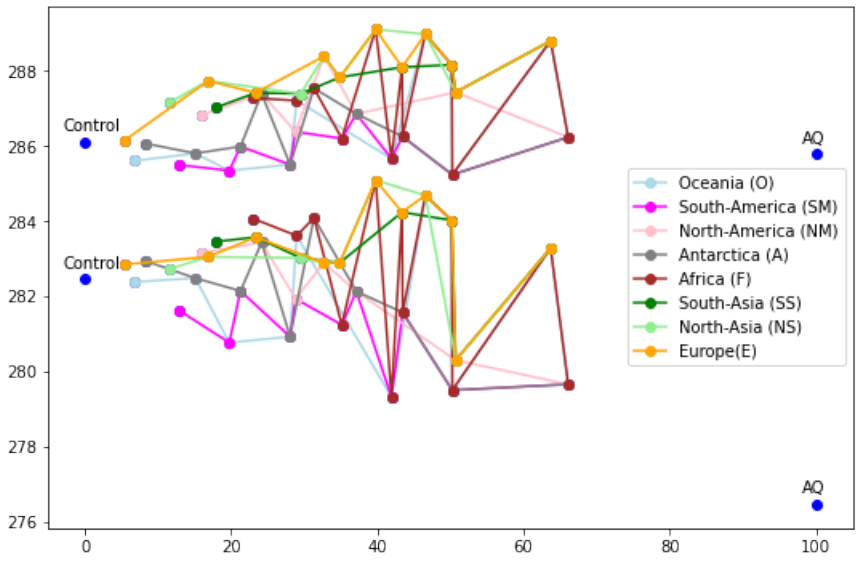

Figure 6.1: Comparison of surface temperature changes between two experiments. The group with higher temperatures corresponds to the experiment with initial sea ice, while the group with lower temperatures corresponds to the experiment without initial ice.

First, there is an approximate $4°C$ difference among the control planetary simulations. Second, it is noticeable that simulations starting with the current sea ice tend to maintain

a temperature around 286K, with some cases even exhibiting slight temperature increases. Conversely, the temperatures of the second set of experiments remain around 282K, with a slightly more distinct tendency towards a decrease of temperature with increasing landmass.

Moreover, it can be seen that the experiments without continents, in both scenarios, exhibit a temperature difference exceeding $8°C$. Notably, in WSI, unlike the situation in CSI, the aquaplanet experiences a considerably lower temperature than the other simulations.

Subsequently, we calculated the temperature differences between CSI and WSI. This comparison was made while considering equivalent simulations (Fig. 6.2).

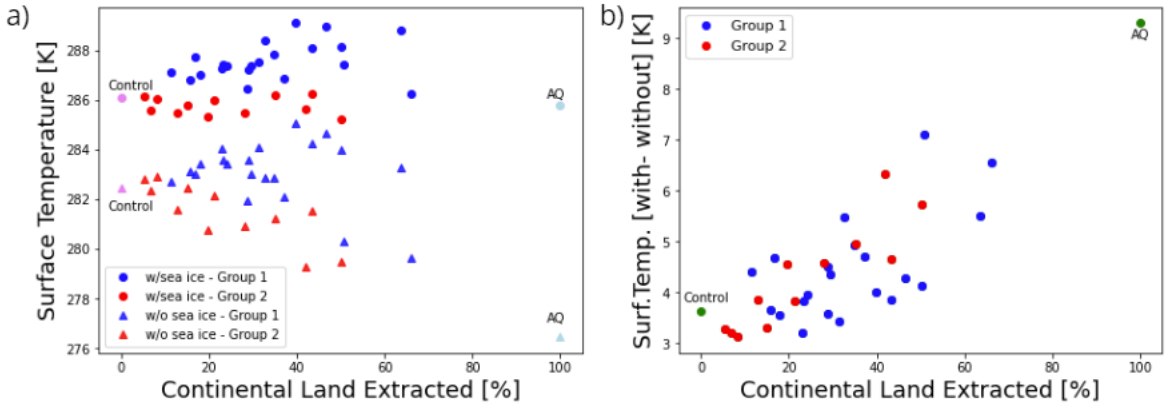

Figure 6.2: a) Depicts Figure 6.1 while denoting the groups in both experiments. b) Presents the temperature differences between the experiments, Group 1 (blue) and Group 2 (red) points.

It is noticeable that as the amount of extracted soil increases, the disparity in temperatures between the two experiments also grows (Fig.6.3). Moreover, the distribution of the groups appears to be fairly consistent. Consequently, it can be inferred that the temperature difference between CSI and WSI is independent of a cause distinct from the factor influencing the divergent behavior of the groups.

Furthermore, upon examining Fig.6.3b, Fig.6.3c and Fig.6.3d, it is possible to see that the growth pattern of sea ice differs depending on its initial amount. In cases where the experiments commence without initial sea ice, the sea ice is capable of growing unimpeded. In contrast, when sea ice is present from the outset, particularly in the instance of current sea ice, it displays more stability and resists alteration. As previously mentioned in §3, this stability might arise from various factors, including potential equilibrium up to the present state, limitations inherent to the model, and more.

6.2 Results - with Sea Ice

6.2.1 Temperature

If we study the first experiment in §4, the division of the groups is as follows (Fig 6.4).

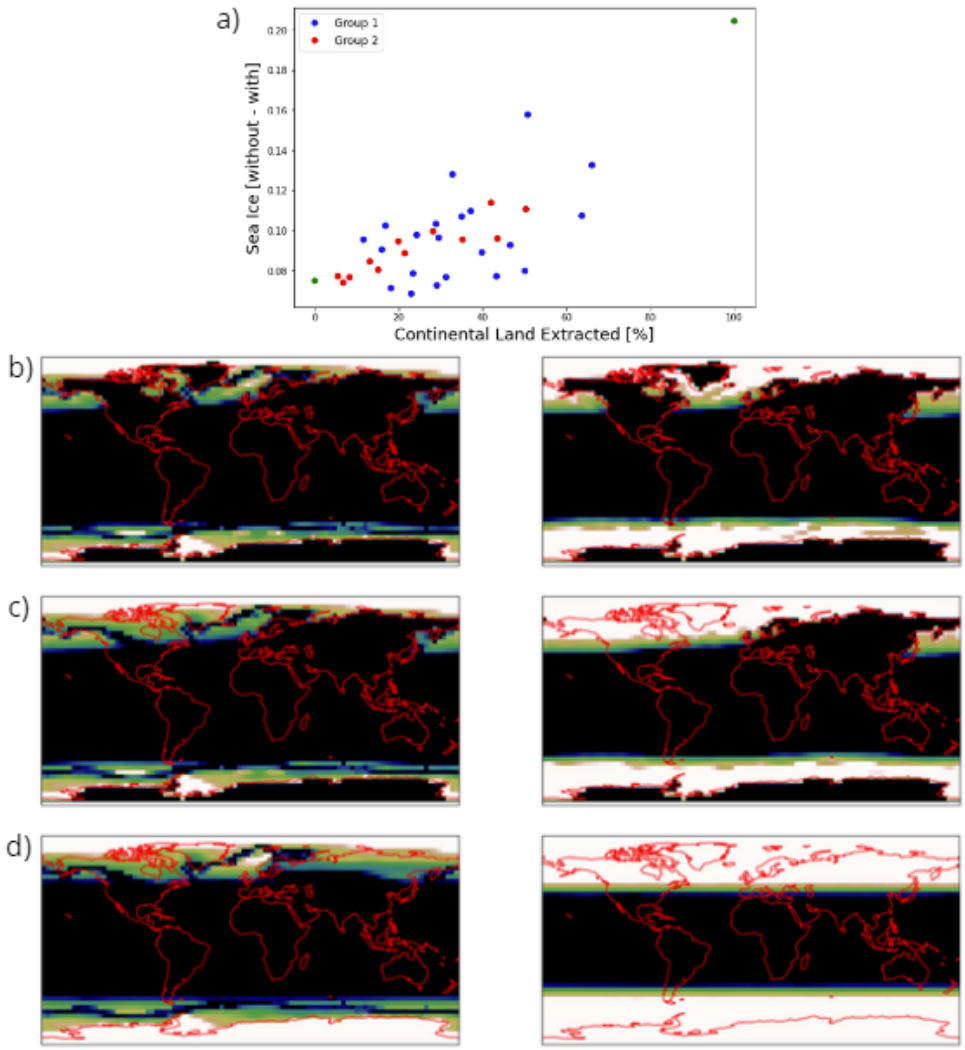

Figure 6.3: a) Represents the sea ice disparity between the two experiments by subtracting Experiment 1 from Experiment 2. b), c), and d) show maps illustrating the behavior of sea ice experiments with the same amount of land extracted, including the control experiment, extraction from Asia and Europe, and extraction from all continents, respectively. The maps on the left correspond to the experiment with current sea ice, while those on the right represent experiments started without initial sea ice. The red outlines indicate the real continental distribution in all cases for reference only.

First, as mentioned above, it is possible to notice that all members belonging to Group 1 (in blue) have a higher temperature than the temperature of the control simulation. On the other hand, Group 2 has a similar or lower temperature than the control.

Second, when making a comparison between the groups, it can be observed that on several occasions, we have two or more simulations with a similar planetary albedo but with quite different temperatures. This difference in surface temperature suggests that, while some simulations retain more energy at the surface, others dissipate more energy to the planet's atmosphere.

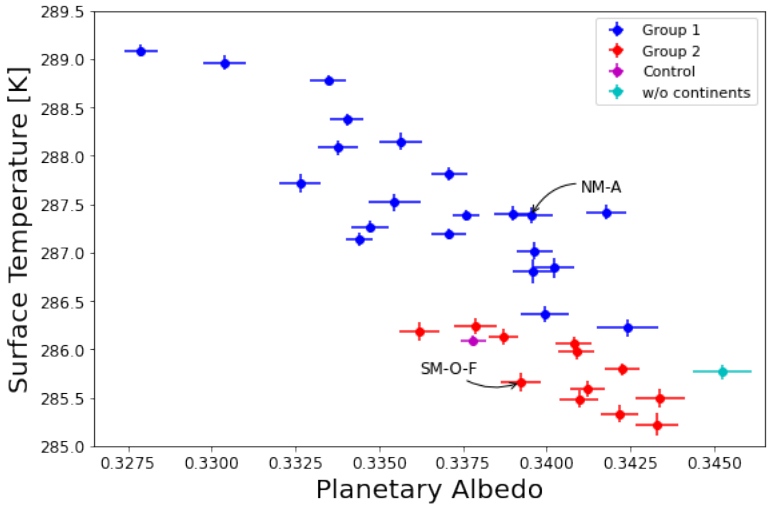

Figure 6.4: Representation of the experiment groups in Chapter 4, highlighting the two groups mentioned above. Two different combinations of extracted continents are marked. The experiment marked in the blue group corresponds to the extraction of Antarctica (A) and North America (NM), while the red dot represents the extraction of South America (SM), Oceania (O), and Africa (F). Both tests show a difference of 0.001 in their planetary albedo and a difference of 1.7 °C in surface temperature.

Looking at and comparing the planetary simulations we find a particularly interesting case, which is the comparison between extraction from North America, Asia, and Europe (NM-E-NS-SS, CNHE hereafter) versus extraction from South America, Oceania, Antarctica, and Africa(LM-O-F-A, CSHE hereafter). These cases are complete opposites since the opposite continents are extracted (Fig. 6.5).

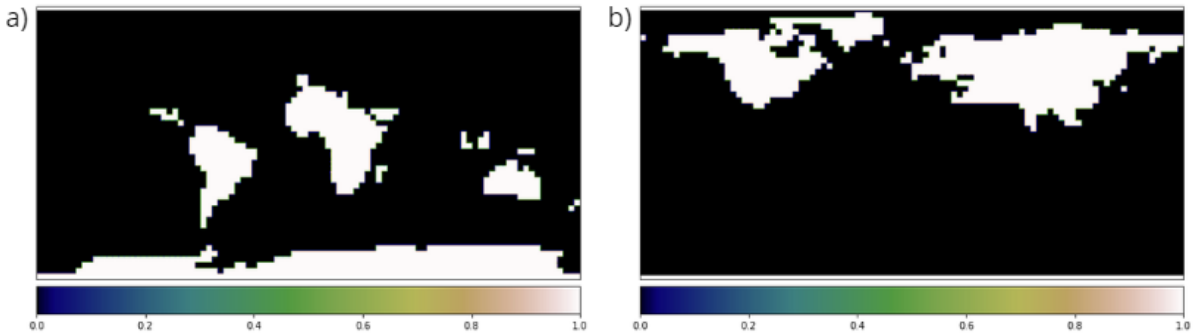

Figure 6.5: Masks representing the amount of continental land remaining in a)NM-E-NS-SS and b) SM-O-F-A. Where 1 represents that there is continental land and 0 represents that there is only sea.

In Figure 6.7a, we can see that the extraction of continents in both experiments has a similar amount of extracted land, 50.3% vs 49.7% of extracted land for CNHE and CSHE, respectively.

Now, if we look at part 6.7b, it is possible to notice that while the CNHE extraction has a

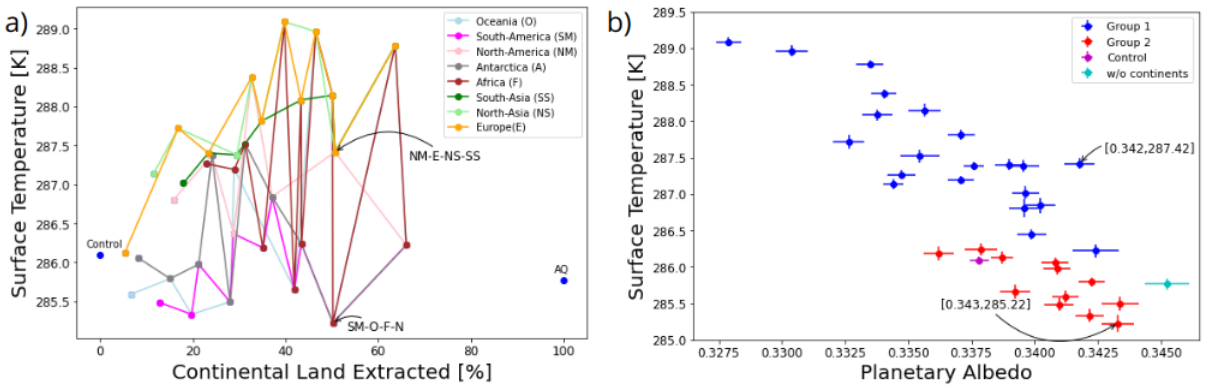

Figure 6.6: Comparison between the extraction of NM-E-NS-SS and SM-O-F-A. a) Shows the relationship between the amount of continental land extracted and the surface temperature and b) planetary albedo in both experiments.

planetary albedo of 0.342, its counterpart has an albedo of 0.343, thus having a difference of only 0.001, corresponding to 7% of the experimental range. Quite different from what happens with the temperature, where CNHE and CSHE have surface temperatures of 287.416 K and 285.224 K, thus having a difference of 2.2 K, being 58% of the experimental range.

6.2.2 Surface Temperature

Our initial focus will be on the surface layer of our planets, which we compared with the control planetary simulation for subsequent analysis. It is important to note that the control surface temperature registers at 286.09 K, representing a variance of 0.83 K higher than CSHE and 1.32 K lower than CNHE.

In Figure 6.7a, the map illustrates the surface temperature (ST) difference between CNHE and the Control, with the most pronounced temperature changes predominantly occurring within the altered zone. Notably, regions such as Greenland exhibit significant temperature increases, which may be attributed to alterations in snow depth in that specific area. On the other hand, in the southern hemisphere where all continents were retained, surface temperature variations remained minimal.

Conversely, in Figure 6.7b, which illustrates the ST map of CSHE relative to the control, it becomes observed that the absence of these continents has repercussions on the surface temperature of multiple regions across the planet, extending beyond the originally altered zone. The most substantial ST elevation occurs within the Antarctic sector, where certain areas witness temperature increases exceeding 30 K in comparison to the control. Nevertheless, a noteworthy portion of the planet experiences temperature reductions.

The following figure (Fig. 6.7c) shows the average surface temperature by latitude based on the maps we have just analyzed. It confirms that CNHE alters the surface temperature (ST) only in the northern hemispheres(NH). In contrast, CSHE affects all latitudes. Firstly, it significantly raises the temperature of the southernmost zone, corresponding to latitudes

70°S and beyond. It also lowers the temperature between latitudes 60°S and 20°S. However, it is important to note that it also modifies the ST of the northern sector of the planet, above latitude 50°N. This implies that while the extraction of CNHE generates a localized change without greatly altering the global atmospheric dynamics, the extraction of CSHE alters all atmospheric dynamics, causing the zones between 20°S and 60°S and those beyond 50°N to dissipate more energy flux into the atmosphere.

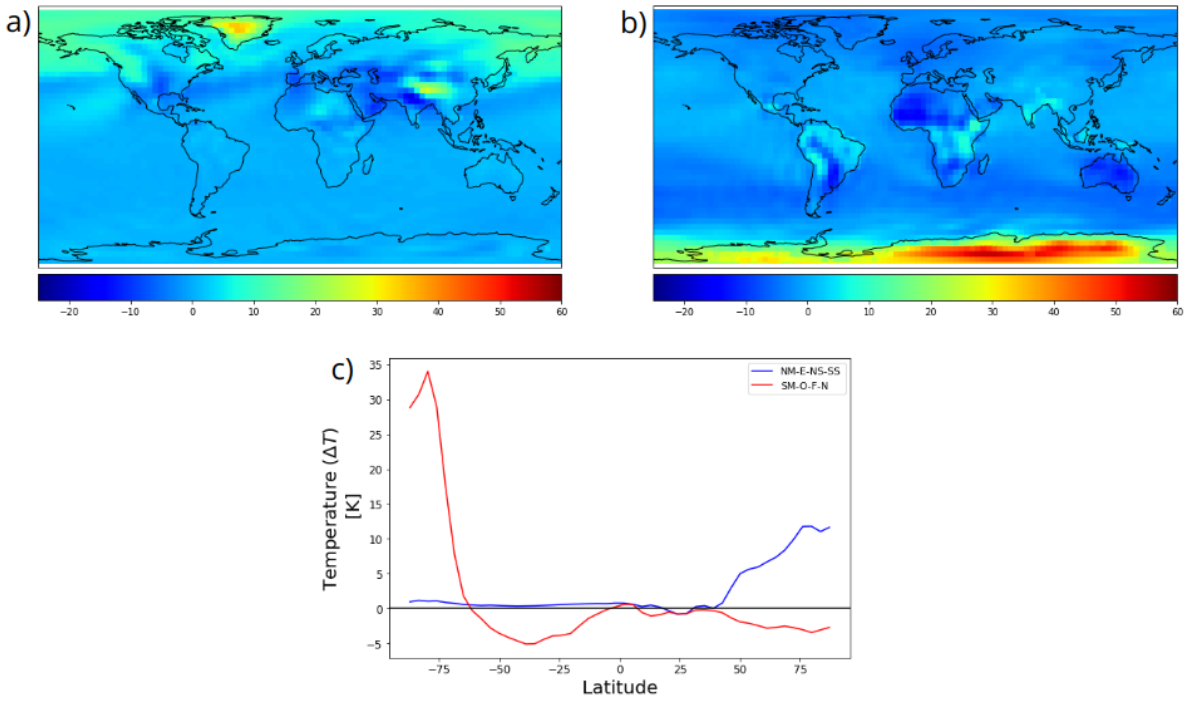

Figure 6.7: The difference in surface temperature between a) CNHE and b) CSHE and the control. c) Difference in surface temperature by latitude.

When examining the temperature by hemisphere, as detailed in Table 6.1, we observe that in the control planetary simulation, the northern hemisphere has a lower temperature than the southern hemisphere. This pattern is also observed in the CSHE simulation. This temperature difference can be attributed to the fact that although extractions in the southern hemisphere lead to an increase in Antarctic temperature, they also result in a lower temperature around the 40° S parallel. Due to the sphericity of the planet, this does not have a significant impact on the average temperature of the hemisphere.

Table 6.1: The table shows the surface temperature of the different planets averaged both globally and by hemisphere.

	Global ST [K]	NH ST [K]	SH ST [K]
Control	286.092	285.823	286.362
CNHE	287.416	287.920	286.911
CSHE	285.224	284.825	285.623

In contrast, the extraction of continents from the northern hemisphere leads to a substantial alteration of the northern hemisphere temperature, resulting in a surface temperature (ST)

that exceeds the control by 2 K. This experiment is the only one among the three with a higher temperature in the northern hemisphere than in the southern hemisphere. Furthermore, the temperature in its southern hemisphere shows only a slight increase compared to the control, confirming that this extraction predominantly induces a localized perturbation.

Finally, let's delve into the behavior of planetary simulations during the two most distinctive seasons of the year: winter and summer (Figure 6.8). The naming of these seasons depends on the hemisphere. They are primarily referred to as December-January-February (DJF) and June-July-August (JJA).

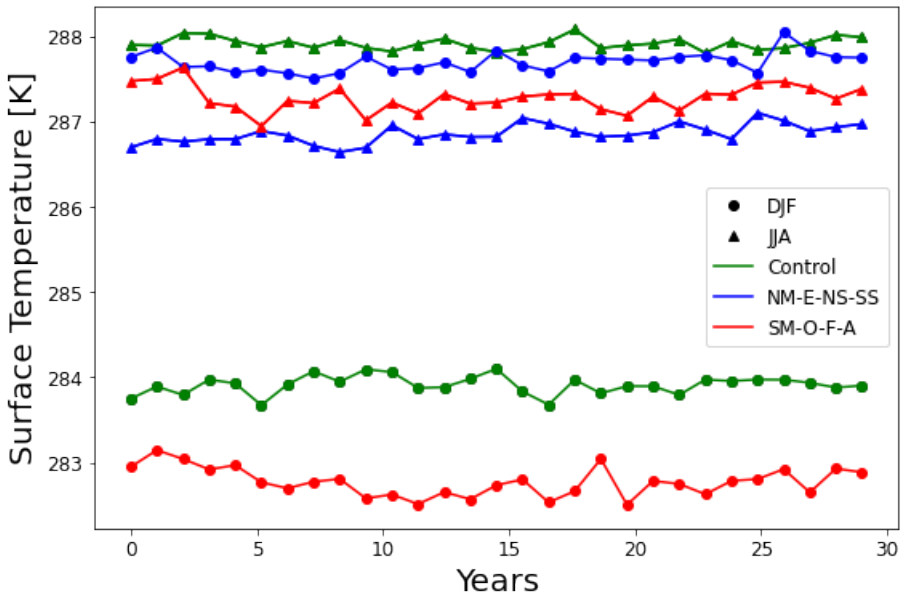

Figure 6.8: Representation of the experiment groups in §4

The main observations from the figure are as follows: In the control simulation, the temperature difference between months JJA and DJF is 4 K. This is similar for CSHE. In contrast, CNHE shows a much smaller temperature variation, suggesting that the removal of continents in this experiment does not significantly alter the mean temperature of the planet throughout the year.

Analyzing the case of CNHE in detail, it is possible to note that while its mean temperature during the JJA months does not differ from the other two simulations, the DJF months exhibit significantly higher temperatures.

For a detailed examination of each hemisphere during different months, we have compiled data in Table 6.2, which displays surface temperatures globally and by hemisphere, averaged across the months in which they were measured. In the control simulation, the expected pattern emerges: the southern hemisphere experiences warmer temperatures during DJF months and cooler temperatures during JJA, consistent with its winter season. The temperature difference between these seasons in the southern hemisphere is 7 K. In contrast, the northern hemisphere exhibits a substantial difference of 15 K between DJF and JJA months, which can be explained by the concept of 'continentality' coined in the 1800s.

The term "continentality" refers to the great thermal variability experienced by a land

Table 6.2: The table shows the surface temperature of the different experiments averaged both globally and by hemisphere including the months of DJF and JJA.

	Global ST [K]		NH ST [K]		SH ST [K]	
	DJF	JJA	DJF	JJA	DJF	JJA
Control	283.91	287.91	277.92	293.03	289.90	282.80
CNHE	287.70	286.86	285.02	290.24	290.37	283.47
CSHE	282.77	287.28	277.20	292.00	288.35	282.55

region due to its distance from a large body of water. A continental climate is characterized by extreme temperatures in the winter and summer seasons, with summers tending to be extremely hot and winters incredibly cold. This is because soils have a limited capacity to retain heat, and heat transfer occurs primarily through the movement of molecules. Therefore, when sunlight, or insolation, reaches the soil, it only penetrates a shallow surface layer. As a result, almost all of the thermal energy is gained and lost at the soil surface. Thus, land areas heat up and cool down rapidly. On the other hand, air, which has a low heat retention capacity and high internal mobility, also changes temperature rapidly in response to the heating and cooling of the land surface.

Water, on the other hand, experiences fewer temperature fluctuations due to its high heat retention capacity and its ability to distribute heat by convection. Insolation penetrates deeper into the water so there is relatively little energy left to heat the air above it. In addition, water experiences more significant evaporation compared to land surfaces, which means that less sunlight is available to heat the water. Lower humidity levels also contribute to more significant temperature variations over land. Consequently, daily and annual temperature ranges are more pronounced over land than over water bodies (Driscoll and Fong, 1992; Duckson, 1987).

Another critical aspect to consider when discussing continentality pertains to the sun's angle and its effects on various latitudes. Our planet has an axial tilt of 23.5°, which results in varying amounts of sunlight reaching different latitudinal regions over a year. This inclination has a minor influence on the equatorial zone or lower latitudes. These regions experience relatively consistent sunlight throughout the year, resulting in a consistently warm and humid tropical climate with minimal temperature fluctuations.

Conversely, higher latitudes receive sunlight at a more oblique angle, leading to fluctuations in energy intake based on the time of year (Brooks, 1919).

Thanks to the definition of 'continentality,' a more precise classification of climates found across a substantial portion of our planet became attainable (Köppen, 1936; Currey, 1974). Notably, continentality manifests most distinctly in the expansive land masses of Asia and North America. These regions meet two primary criteria: their considerable land extent, which extends significantly far from the oceans, and their location at higher latitudes. As a result, they experience considerable variations in solar radiation throughout the year.

This climatological phenomenon explains the observations in the planetary simulation

after CNHE extraction. As mentioned above, the climatic changes in Group 1 can be attributed to the removal of portions of Asia or North America. This suggests that the removal of these continents would result in milder winters and cooler summers in this region (Table 6.2).

By replacing these vast land masses with the sea, which has a higher heat capacity, the sea can more effectively moderate surface temperatures, resulting in significantly more temperate conditions.

On the other hand, to analyze what happens with the CSHE experiment, it is necessary to consider the impact of each of the continents extracted. First, when studying the case of Africa, it is noticeable that, like Asia and North America, it is a large continent located between latitudes 37°N and 34°S. Therefore, unlike the aforementioned continents, it is not significantly affected by continentality. Africa is nearly centered on the equator, resulting in warm climates in areas closest to the equator, including equatorial (Af), monsoon (Am), and savanna (As) climates according to Köppen's classification (Fig 6.9). In contrast, the northern and southern parts of Africa primarily experience warm desert climates (BWh) because they are situated around latitudes 30°N and 30°S, known as horse latitudes. These latitudes are characterized by the descent of the Hadley cells, which leads to high atmospheric pressure in the area, referred to as subtropical high. These regions receive little rainfall and have mainly calm winds, resulting in hot and dry conditions that contribute to the existence of deserts.

Returning to Fig 6.7b, it can be observed that the extraction of North Africa contributes to a significant portion of the land extracted in the northern hemisphere in this planetary simulation. This could be a cause of the slight temperature decrease in these latitudes (Fig. 6.7c). However, it's important to note that while temperatures drop in the area where North Africa is extracted, they rise slightly in the regions of India and Central America.

When comparing the temperature in the northern hemisphere in this experiment with the control experiment, it becomes evident that both summer and winter in this hemisphere would be slightly colder.

Analyzing South America, we can note that this extract of the American continent spans from latitude 12°N to 53°S. A significant portion of its landmass is situated between latitude 12°N and the Tropic of Capricorn (23°S), resulting in predominantly equatorial and tropical climates, similar to central Africa. Further south from the tropics, a wide variety of climates can be found, including a warm desert climate in the Atacama Desert and a warm-summer humid continental climate in Lonquimay.

Fig 6.7a shows that when land is extracted around the equator's latitudes, temperatures tend to rise in this area, except for a sector in the Amazon that extends down the eastern side of the Andes mountain range to the northern sector of Argentina. A slight drop in ocean temperatures at this latitude can also be observed, indicating that there is not a significant temperature variation in this area.

Oceania primarily experiences a warm desert climate, similar to southern Africa.

Antarctica, on the other hand, has a glacial climate. However, it's important to note the

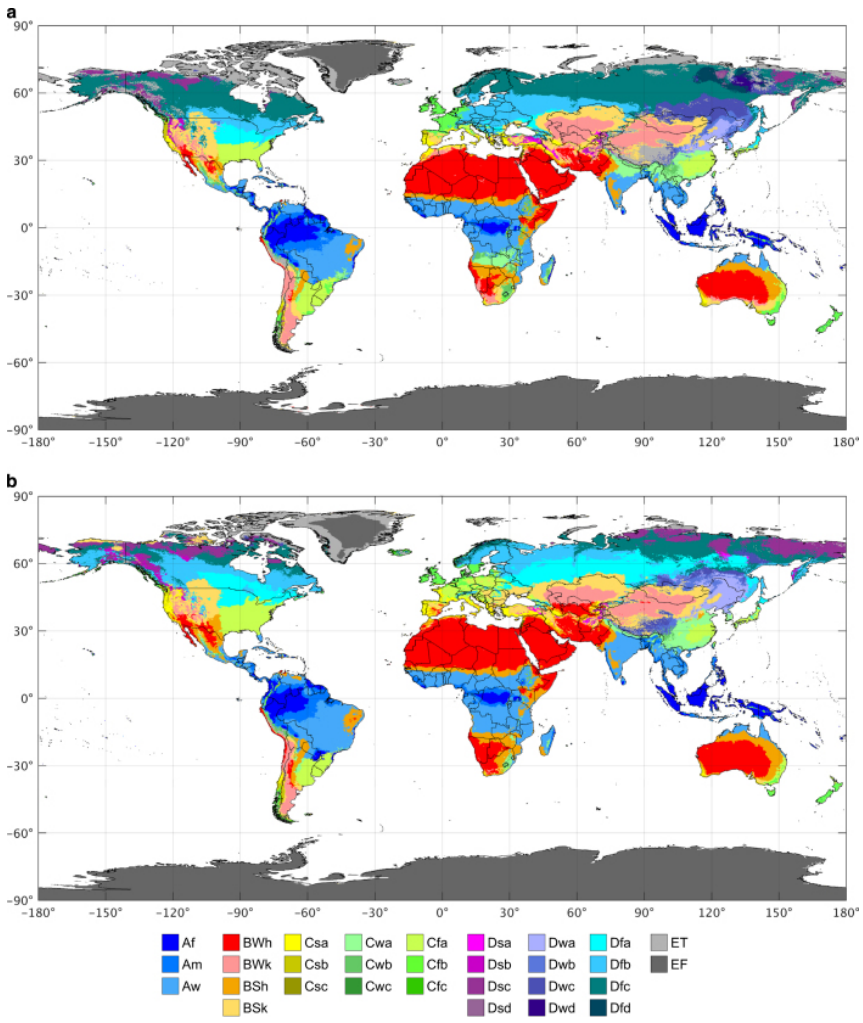

Figure 6.9: Note. New and improved Köppen-Geiger classifications. Reprinted from "Present and future Köppen-Geiger climate classification maps at 1-km resolution" by Hylke E. Beck., et. al, 2018, Nature Scientific Data, 5, id. 180214, p. 3 (`https://www.nature.com/articles/sdata2018214`).

difference between sea ice and ice sheets. Sea ice, being constantly exposed to the ocean, which has a higher temperature than freezing, is more sensitive to both ocean temperature and currents, which vary with the seasons. It is also more exposed to warmer air in the summer, making it more susceptible to melting compared to ice sheets.

Ice sheets are situated further inland and generally at higher altitudes, resulting in lower temperatures. They are farther from the ocean and have a more stable and extremely cold environment, making them more resistant to melting. Hence, when the south polar ice shifts from sea ice to ice sheets, it has a higher temperature and is more prone to seasonal variations (Jacobs *et al.*, 1992; Cuffey and Paterson, 2010).

The southern hemisphere's temperature difference compared to the original simulation is approximately 0.7 K in summer and nearly 1 K in winter. This difference arises because the removal of Antarctica raises temperatures in the polar latitudes, while the removal of

land from South America and Oceania decreases temperatures in the mid-latitudes. These opposing effects balance out the overall change in this hemisphere.

It's important to consider that the observations related to the CSHE experiment are based on assumptions derived from the climates of the extracted continents and the obtained results. The outcome is likely a result of the collective impact of these four extracted zones. Different results could be expected if these zones were extracted differently. To provide a comprehensive analysis, further studies on the variation of ocean currents and temperatures would be required, which falls outside this project's scope.

6.2.3 Cloud Cover and Precipitation

When modifying the planet's surface, not only direct changes occur, such as surface albedo, but also atmospheric circulation, precipitation, and cloudiness, among others, are altered. These latter two factors can assist us in understanding and visualizing the effect of continentality, as well as confirming or refuting this hypothesis.

CNHE

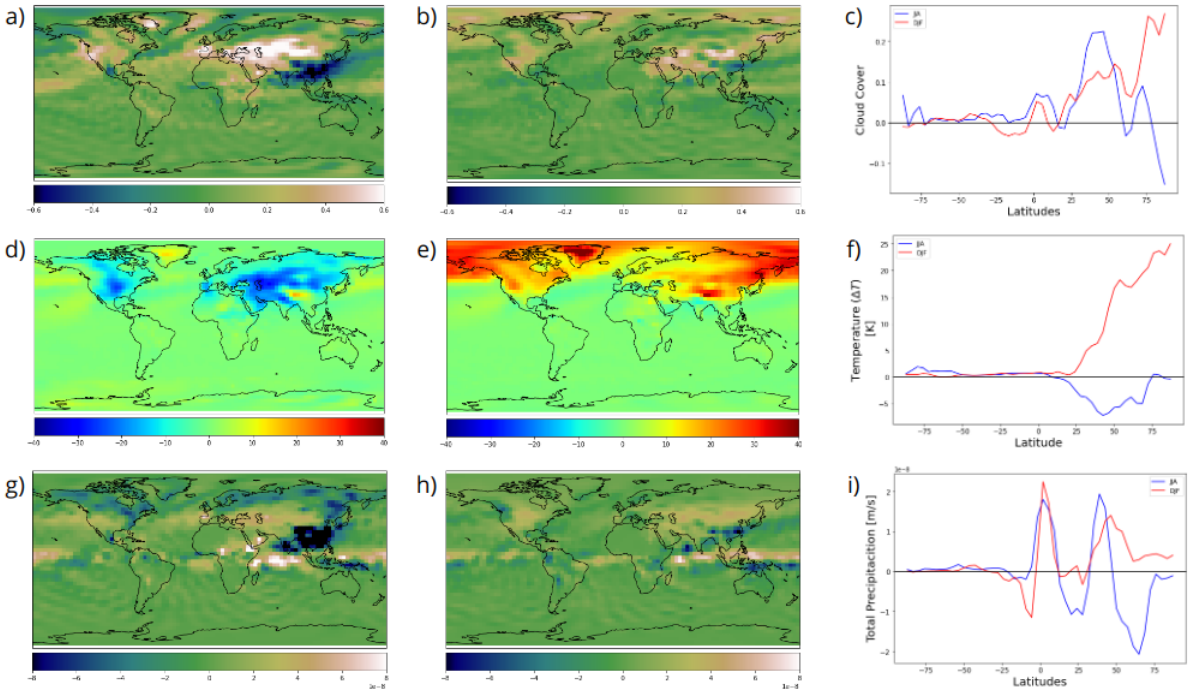

Figure 6.10: a), b), c) are graphs corresponding to the cloud cover of the region when compared to the control simulation. Similarly, d), e), and f) would be the difference in Surface Temperature with the control, and finally, g), h), and i) represent the difference in precipitation. The letters a), d), and g) correspond to the months of JJA, while b), e), and h) are for the months of DJF.

The cloud cover is notably higher in both the JJA and DJF months (Fig. 6.10a and Fig. 6.10b), but a greater coverage can be observed during the summer months, covering much of Central Asia. This could be caused by the absence of land in the region, as increasing temperatures in the summer would heat the sea, leading to greater water evaporation. Additionally, the formation of clouds in this area would create a layer that would prevent light from reaching the surface, thus generating colder areas (Fig. 6.10d). That could corroborate the effects of continentality on the large continents. As for precipitation, it varies in summer compared to the control simulation, decreasing by around 25°, then increasing to about 40°, and finally decreasing by about 70°. The difference in cloudiness and precipitation in the East Asian sector is likely due to the suppression of the East Asian Rainy Season, which produces heavy rains in this region (Fig. 6.10i).

In winter, there are also more clouds in the Northern Hemisphere, but they are much more controlled than in summer (Fig. 6.10b). These clouds could also help retain heat on the surface and prevent it from becoming too cold. However, when comparing the temperature and cloudiness of this region, it can be observed that there is a large sector over the Pacific Ocean, near the polar zone, which has a higher temperature (Fig. 6.10e), which cannot be explained solely by the number of clouds in the area. On the other hand, precipitation increases at the 50-degree North latitude during these months (Fig. 6.10i).

CSHE

When extracting SM-O-F-A, the summer months (DJF) and winter months (JJA) in the southern hemisphere show temperature variations across the globe, both in the region belonging to the southern hemisphere and in the opposite hemisphere (Fig. 6.11.d and Fig. 6.11.e), but focusing this change on the directly affected hemisphere. During the summer, temperature and cloud cover decrease in the southern subtropical zone. On the other hand, there is an increase in surface temperature and cloud cover in the equatorial zones and an increase in cloud cover in the African savanna region (Fig. 6.11.b). This differs from what occurred with NM-E-SS-SN.

During the JJA months, a temperature decrease can be observed in the African savanna region (Fig. 6.11d). Cloud cover slightly increases in the subtropics and the African savanna but tends to decrease slightly near the equator (Fig. 6.11a and Fig. 6.11c). Precipitation increases mainly near the equator (Fig. 6.11i).

6.2.4 Albedo

In the control case, 85% of the planetary albedo is attributed to atmospheric albedo, while only 15% is attributed to surface albedo. In the case of NM-E-SS-NS, atmospheric albedo affects planetary albedo by 4% more than the control, and in the case of SM-O-F-A, it affects it by 3% more(Fig.6.12b).

Thus, the extraction of these continents slightly increases the planet's albedo, resulting in clouds making a greater contribution. On the other hand, as mentioned earlier, CSHE and

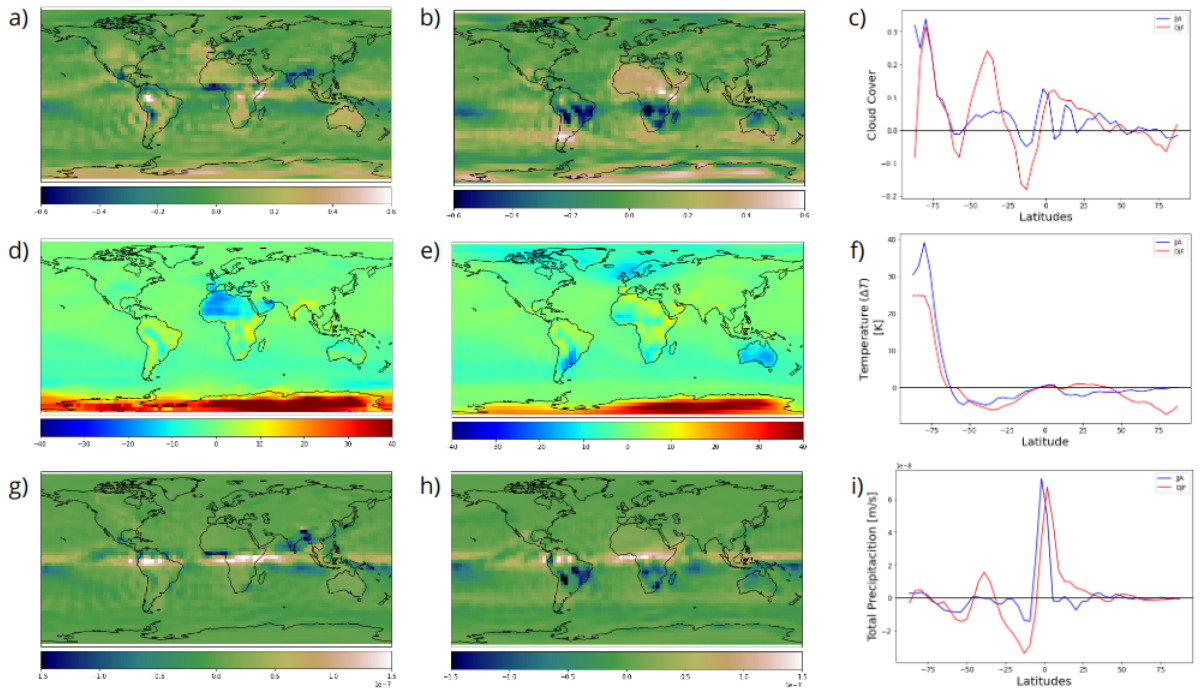

Figure 6.11: a), b), c) are graphs corresponding to the cloud cover of the region when compared to the control simulation. Similarly, d), e), and f) would be the difference in Surface Temperature with the control, and finally, g), h), and i) represent the difference in precipitation. The letters a), d), and g) correspond to the months of JJA, while b), e), and h) are for the months of DJF.

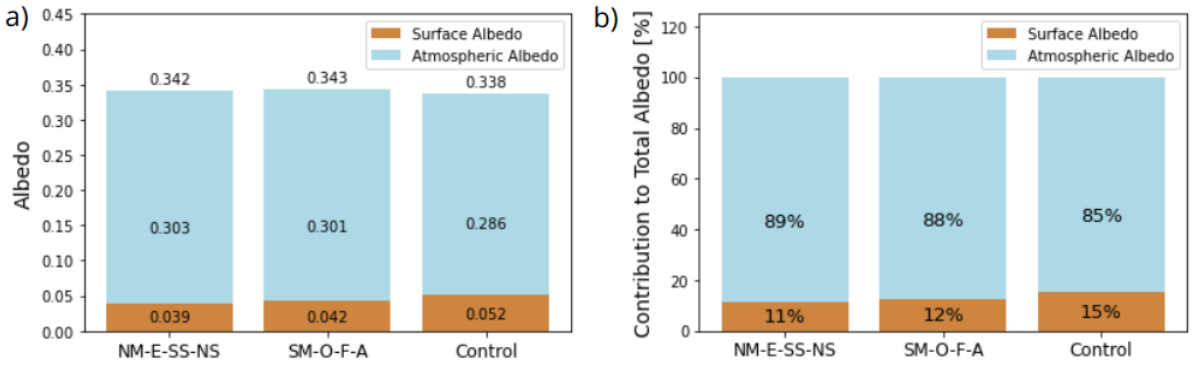

Figure 6.12: a) Comparison of albedo between control simulation, CSHE, and CNHE. The planetary albedo of each experiment is shown on top of the bars, while within each color on the bar, the albedo provided by both the atmosphere and the surface is shown as applicable. b) Contribution of each component to the planetary albedo; within the bars, the percentage contribution of each component is displayed.

CSHE have similar planetary albedo, but surface albedo slightly affects CSHE more than CNHE(Fig.6.12a).

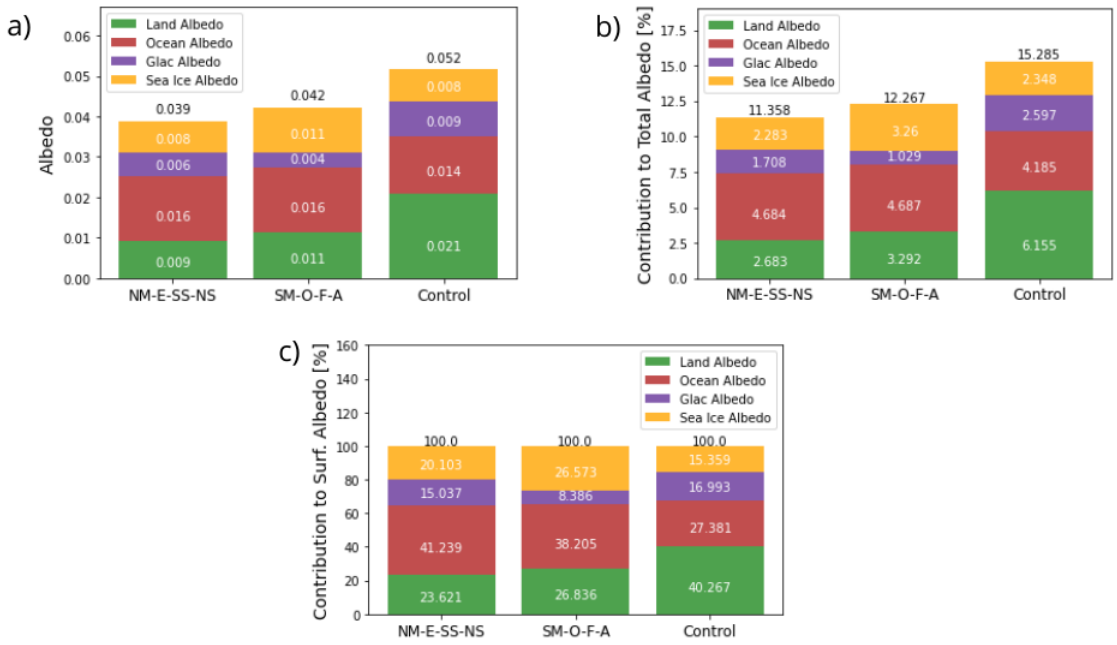

Figure 6.13: a) Comparison of albedo between control simulation, CSHE, and CNHE. The planetary albedo of each experiment is shown on top of the bars, while within each color on the bar, the albedo provided by each component on the planet's surface is shown as applicable. b) Contribution of each component to the planetary albedo; within the bars, the percentage contribution of each component is displayed. c) Contribution of each component to the surface albedo; within the bars, the percentage contribution of each component is displayed.

In the case of different planet surface components, the albedo provided by the ocean is similar in both the control and CNHE and CSHE simulations. Similarly, this occurs with the 'ice' component, with the difference that in CSHE there is notably more sea ice than glacier ice, which the extraction of Antarctica could explain. It can be seen that the biggest difference lies specifically in the albedo provided by the land, whereas in the control simulation, it is clearly higher (Fig. 6.13).

Proportionally, the ocean's contribution leads to both CNHE and CSHE, with its contribution being greater in CNHE. In CSHE, the land contributes more to the surface albedo and, thus, to the planetary albedo.

6.2.5 Vertical Temperature Profile

To better comprehend the distribution of energy fluxes in CSHE and CNHE as proxies for their respective groups, an analysis of the variation in atmospheric temperature with increasing altitude from the Earth's surface was conducted.

CNHE keeps the atmosphere warmer in the lower kilometers of altitude, while CSHE

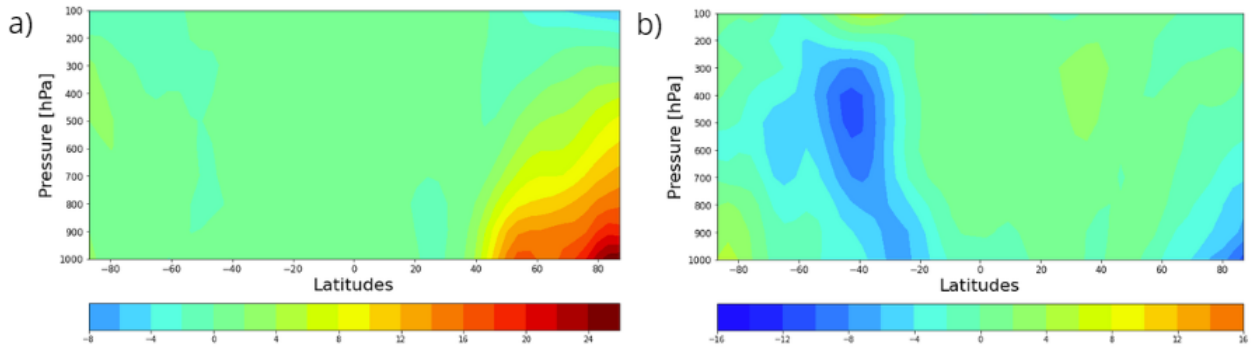

Figure 6.14: Temperature profile of both representatives minus the control case for a) CNHE and b) CSHE. CNHE presents higher temperatures from the 50th parallel northward, maintaining temperatures close to the control simulation in the rest of the atmosphere. In contrast, CSHE exhibits a region with lower temperatures over latitudes -20 to -40 at 400 hPa, extending to the surface and another cold region near the North Pole.

displays a slight decrease in temperature in specific parts of the atmosphere(Fig.6.14). Therefore, it is essential to determine where the energy is distributed for the latter.

When examining a vertical atmosphere profile, as depicted in Figure 6.15a, we notice a shift between the experiments in the 200 hPa to 100 hPa range, where CNHE becomes cooler than CSHE. This suggests that CSHE retains more energy than CNHE at altitudes above 100 hPa and vice-versa.

It should be noted that the profile shown here extends only up to 10 hPa, as this is the altitude up to which PlaSim provides reliable temperature data.

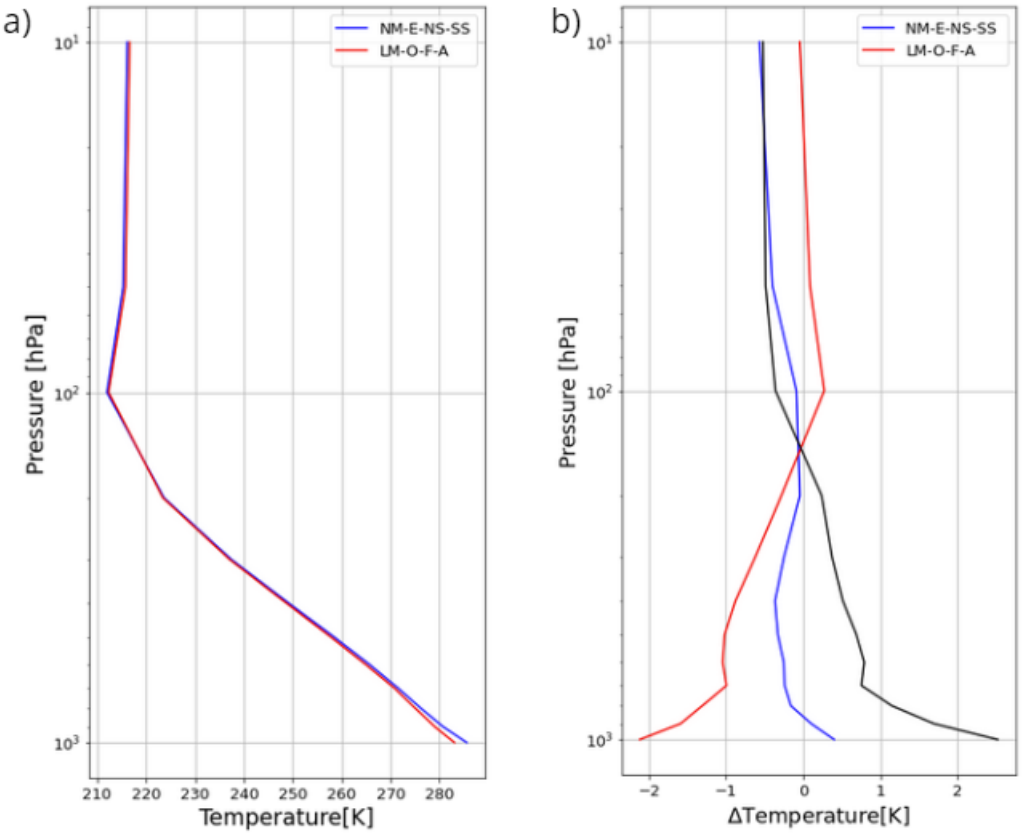

Figure 6.15: a) Comparison of the temperature profile between both experiments. b) Difference between the temperature profiles for each experiment and the control case (blue and red lines) and between themselves (Group 1 - Group 2, black line).

6.3 Results - without Sea Ice

It is necessary to investigate the differences between the groups to extend the insights gained from the previous analysis to the results obtained in Chapter 5. This can be accomplished by examining Figure 6.16, which demonstrates, as observed in the preceding section, that Group 1 exhibits higher temperatures than Group 2.

First, let's examine whether groups defined for the previous initial condition behave differently with WSI.

In contrast to the previous discussion in §6.2, the temperature difference between the two groups is slightly smaller. Another distinction is that, in this case, both experiments yield a lower overall surface temperature compared to the control

Following the same analytical approach and examining Figures 6.17a and 6.17b, it can

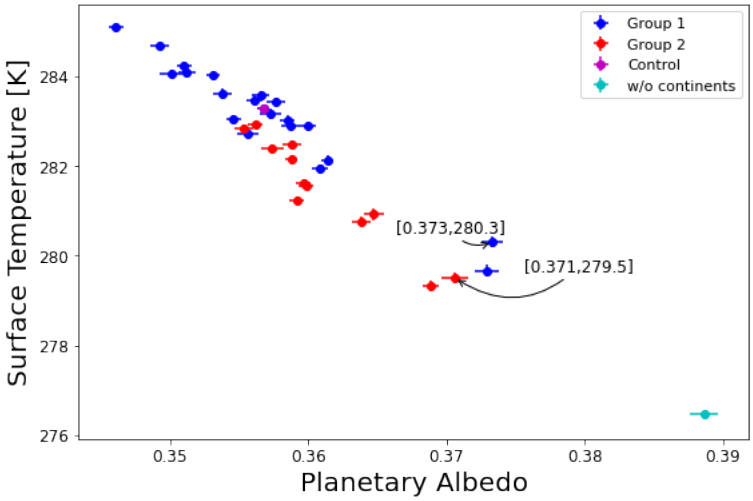

Figure 6.16: Representation of the experiment groups in the Chapter 5, but now without initial sea ice (c.r 6.4)

be seen that CNHE exhibits predominantly local changes. Nevertheless, it records lower temperatures compared to the scenario in which sea ice is present from the beginning, indicating a decrease of nearly 10 K in the Asian region.

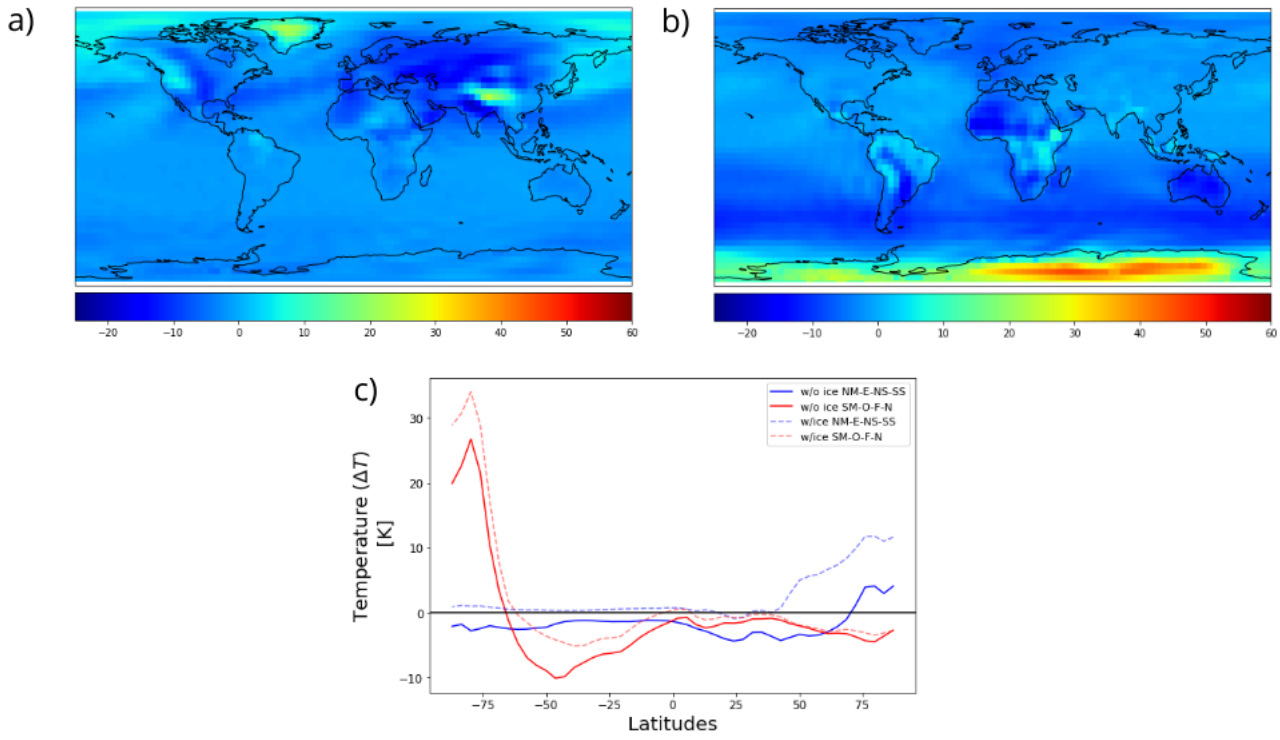

Figure 6.17: The difference in surface temperature between a) CNHE and b) CSHE and the control. c) Difference in surface temperature by latitude. Solid lines are the experiment without initial sea ice while dashed lines are the same representer in Fig. 6.7

CSHE exhibits behavior similar to that observed in the previous section, inducing changes

in surface temperature across the planet, primarily concentrated in the altered zone. A decrease in temperature occurs around the 50°S latitude band, influenced by factors such as the African Savannah and Australia.

Figure 6.17c validates the trends observed in the analyzed masks. CNHE does not bring about significant changes in the southern hemisphere, maintaining temperatures slightly lower than the control without marked variations between different latitudes. Instead, the most significant changes concentrate on where the continents were removed. A temperature reduction is noticeable between the 10th and 55th parallel north, followed by an increase near the poles

CSHE, on the other hand, exerts an influence on temperatures across most latitudes. It elevates temperatures by almost 25 K at the South Pole while causing a decrease of 10 K around 50°S. Temperature patterns in CSHE resemble those in the control simulation between the equator and 40°N, followed by a slight decrease in temperature towards the North Pole.

The observations depicted in this figure align with the results discussed in §6.2(dashed in Fig 6.17). CNHE produces similar outcomes but exhibits overall lower temperatures across the planet without initial sea ice. There is a temperature variation between latitudes 50 and 70, which is cooler than the conditions described in the previous section.

Similarly, CSHE exhibits colder temperatures across all latitudes in the southern hemisphere. Conversely, in this case, the northern hemisphere does not show a significant temperature difference.

When analyzing the global surface temperatures by hemisphere in Table 6.3, it is observed that the control simulation exhibits a slight difference between both hemispheres, with the southern hemisphere being warmer. Both the representatives of Group 1 and Group 2 have lower surface temperatures than the control, both overall and in both hemispheres. The distinction is that CNHE has higher temperatures in the southern hemisphere, whereas CSHE exhibits higher temperatures in the northern hemisphere.

Table 6.3: The table shows the different planets' surface temperatures averaged globally and by hemisphere.

	Global ST [K]	NH ST [K]	SH ST [K]
Control	282.464	282.161	282.766
CNHE	280.296	279.387	281.204
CSHE	279.499	280.364	278.633

In the study by seasons, as presented in Table 6.4, the exclusion of CNHE results in a greater difference between stations in the southern hemisphere and northern hemisphere compared to its counterpart in Table 6.2.

In fact, when comparing CSHE to the control, temperatures consistently register lower values across the table, except for the hemisphere in JJA (June, July, August) where temperatures are notably reduced. This suggests that, while there is a general alteration in the planet's overall climate when these continents are removed, the most significant change occurs

Table 6.4: The table shows the surface temperature of the different experiments averaged both globally and by hemisphere including the months of DJF and JJA.

	Global ST [K]		NH ST [K]		SH ST [K]	
	DJF	JJA	DJF	JJA	DJF	JJA
Control	280.48	284.57	273.03	291.11	287.94	278.02
CNHE	280.05	280.74	273.23	285.48	286.86	276.00
CSHE	278.08	281.05	271.29	289.46	284.86	272.64

in how the surface of the southern hemisphere responds to reduced exposure to sunlight in winter, leading to slightly colder winters.

It is important to note that the primary distinction between the previous and current sections lies in the presence or absence of initial sea ice and its impact on climate. In Figure 6.17c, a temperature drop was observed from the 60th parallel south to the equator, corresponding to the region where sea ice transitions into the ocean. This implies that in CSHE, this region is most affected by ocean currents from the cold Antarctica.

Analyzing the case of CNHE is slightly more intricate. While continentality does have an effect, it's not as pronounced as in the previous section. Similar to SM-O-F-A, a temperature drop is observed from the 60°N sector towards the equator, creating a colder region where sea ice melts, affecting even up to the 30th parallel North. According to Stonevicius *et al.* (2018), the high spatial variability in continentality may result from large-scale circulation patterns and local factors such as sea ice.

6.3.1 Vertical Temperature Profile

In the analysis of the temperature profiles in the first layer of the atmosphere (Figure 6.18), CSHE maintains a behavior similar to that seen in Figure 6.14. However, there's a notable difference in CNHE. Instead of having a warm zone near the surface, there's a cold zone between 10°N and 60°N, extending to an even colder sector at around latitude -20, which goes up to 200 hPa. Additionally, a warmer ring is observed between the 60th and 80th parallels North at 900 hPa.

In this case, the profiles of the two representatives are quite similar(Fig. 6.15). Both representatives maintain lower temperatures throughout the profile compared to the control. However, the intersection between the two occurs around 800 hPa, where CSHE becomes slightly higher in temperature than CNHE, as shown in Figure 6.19b approximately 650 hPa higher in the atmosphere. Different from what occurs in the §6.2, where the intersection occurs closer to the tropopause than the planetary surface.

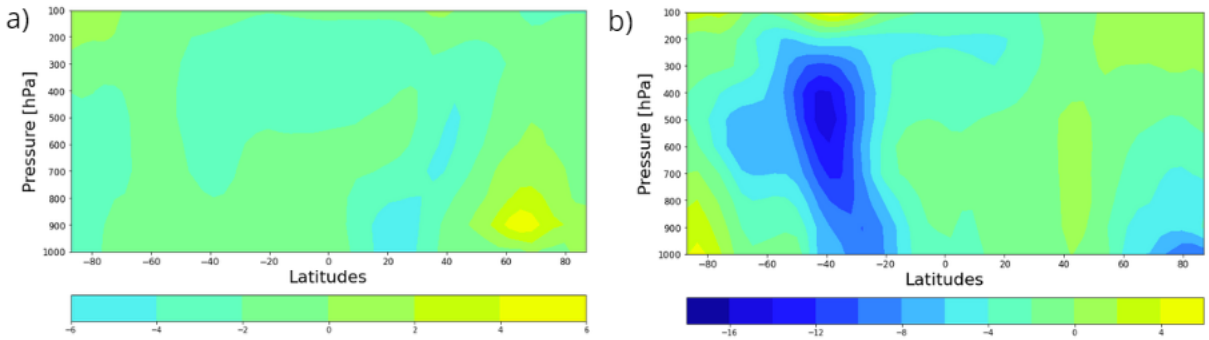

Figure 6.18: Temperature profile of both representatives minus the control case for a) CNHE and b) CSHE.

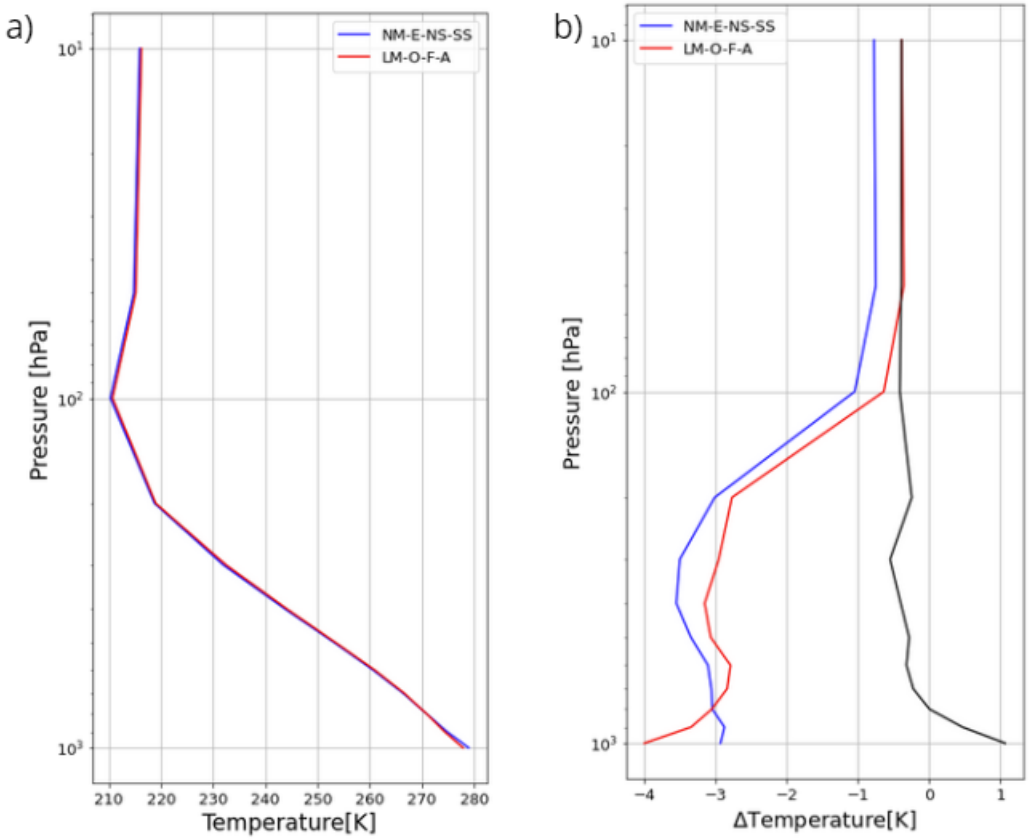

Figure 6.19: a) Comparison of the temperature profile between both experiments. b) Difference between the temperature profiles for each experiment and the control case (blue and red lines) and between themselves (Group 1 - Group 2, black line).

Chapter 7

Conclusions

Planetary habitability depends on several factors, both orbital and planetary. Therefore, to study and understand it, it is necessary to investigate each factor. Thus, the present project aimed to conduct a more detailed study of an essential aspect within the geophysical and climatic dynamics: the role of continental landmasses in the surface temperature of an Earth-like planet.

For this purpose, a total of 70 different simulations were created, divided into two experiments: 35 of them began with the same amount of sea ice as our planet has today, and 35 started with no traces of sea ice in their initial conditions.

The experiment that began with sea ice in its initial conditions can be subdivided into two groups with different behaviors. The so-called 'group 1' is characterized by the removal of continents such as Asia and North America, which entails the extraction of large land masses at high latitudes. Meanwhile, 'group 2' includes extraction from the other continents, namely Africa, Europe, South America, Oceania, and Antarctica, as well as combinations.

We find that by extracting the different continents, the contribution of surface albedo to planetary albedo decreases while the contribution of atmospheric albedo increases.

We observe that obtaining 2 or more simulations with different surface temperatures with the same planetary albedo is possible. In these cases, members belonging to Group 1 exhibit higher surface temperatures than members of Group 2, implying that Group 1 retains more energy on its surface and in the atmosphere near it, while Group 2 dissipates energy to the upper layers.

This phenomenon can be attributed to "continentality," which refers to the significant variability of continental temperature in regions far from water masses, mainly located at higher latitudes. Due to the low heat capacity of the soil, these areas experience extremely cold winters and very hot summers. Asia and North America, in particular, are very susceptible to this effect. Consequently, and by eliminating these continents, the ocean, which has a greater heat capacity, begins to regulate temperatures in the northern hemisphere, resulting in milder winters, colder summers, and an increase in global temperature.

Colder summers could be caused by the shift from land to sea. In this situation, the central

area of these large continents would begin to evaporate water during the summer, generating more significant cloudiness. This cloudiness would prevent solar radiation from reaching the surface, resulting in colder temperatures. On the contrary, this cloudiness could retain heat on the surface in winter, although apparently, there is another, stronger mechanism that keeps the northern polar area warm.

The impact of extraction from other continents depends on their distribution, with key factors being their extent and location. For example, Africa, a vast continent, could potentially experience continentality; however, its equatorial location and position within the high-pressure zone of the Hadley cell contribute to its warmer climate. Therefore, extraction from Africa would have a completely different outcome. Since each area changes temperature differently, while the temperature of the African savanna area decreases, the equatorial area of Africa increases its temperature. The case of South America is quite complex since the temperature variation is strongly linked to both its tropical zone and the Andes mountain range, and a relevant change in temperature is also seen on the coasts of the Pacific Ocean.

The set of 35 planetary simulations without sea ice at the beginning presents a general behavior different from the previous case. While this set experiences continentality in Asia and North America, it is not as pronounced because even without these continents, the difference between summer and winter temperatures is not as extreme as in other configurations, probably due to sea ice. However, this set still has considerably colder winters than the previous set with current sea ice. This is because local components, such as the presence of sea ice, also influence continentality. These continents, located at high latitudes, have greater interaction with sea ice, which can significantly impact and cool these regions during winter, especially when sea ice predominates.

In conclusion, by extrapolating these results to the habitability of other planets, we can infer that a planet with an obliquity of 23° and substantial land masses at high latitudes will have a much colder surface compared to planets without such land masses.

Bibliography

Abbot, D. S., N. B. Cowan, and F. J. Ciesla 2012. Indication of Insensitivity of Planetary Weathering Behavior and Habitable Zone to Surface Land Fraction. *756*(2), 178.

Abe, Y., A. Abe-Ouchi, N. H. Sleep, and K. J. Zahnle 2011. Habitable Zone Limits for Dry Planets. *Astrobiology 11*(5), 443–460.

Beck, H. E., N. E. Zimmermann, T. R. McVicar, N. Vergopolan, A. Berg, and E. F. Wood 2018. Present and future Köppen-Geiger climate classification maps at 1-km resolution. *Nature Scientific Data* **5**, 180214.

Blackburn, M., D. L. Williamson, K. Nakajima, W. Ohfuchi, Y. O. Takahashi, Y.-Y. Hayashi, H. Nakamura, M. Ishiwatari, J. L. McGregor, H. Borth, V. Wirth, H. Frank, P. Bechtold, N. P. Wedi, H. Tomita, M. Satoh, M. Zhao, I. M. Held, M. J. Suarez, M.-I. Lee, M. Watanabe, M. Kimoto, Y. Liu, Z. Wang, A. Molod, K. Rajendran, A. Kitoh, and R. Stratton 2013. The Aqua-Planet Experiment (APE): CONTROL SST Simulation. *Journal of the Meteorological Society of Japan* **91A**, 17–56.

Boschi, R., V. Lucarini, and S. Pascale 2013. Bistability of the climate around the habitable zone: A thermodynamic investigation. *226*(2), 1724–1742.

Brooks, C. E. P. 1919. Continentality and Temperature. *Monthly Weather Review 47*(9), 653.

Catling, D. 2013. *Astrobiology: A Very Short Introduction*. Very Short Introductions. OUP Oxford.

Cuffey, K., and W. Paterson 2010. *The Physics of Glaciers*. Elsevier Science.

Currey, D. R. 1974. Continentality of extratropical climates. *Annals of the Association of American Geographers 64*(2), 268–280.

Dahms, E., H. Borth, F. Lunkeit, and K. Fraedrich 2011. ITCZ Splitting and the Influence of Large-Scale Eddy Fields on the Tropical Mean State. *Journal of the Meteorological Society of Japan 89*(5), 399–411.

Derry, L. A. 2009. *Weathering and Climate*, pp. 981–986. Dordrecht: Springer Netherlands.

Donohoe, A., and D. S. Battisti 2011. Atmospheric and Surface Contributions to Planetary Albedo. *Journal of Climate 24*(16), 4402–4418.

Driscoll, D. M., and J. M. Y. Fong 1992. Continentality: A basic climatic parameter re-examined. *International Journal of Climatology 12*(2), 185–192.

Duckson, D. W. 1987. *Continentality*, pp. 365–367. Boston, MA: Springer US.

Fraedrich, K. 2012. A suite of user-friendly global climate models: Hysteresis experiments. *European Physical Journal Plus* **127**, 53.

Fraedrich, K., H. Jansen, E. Kirk, U. Luksch, and F. Lunkeit 2005. The Planet Simulator: Towards a user friendly model. *Meteorologische Zeitschrift 14*(3), 299–304.

Fraedrich, K., H. Jansen, E. Kirk, and F. Lunkeit 2005. The planet simulator: Green planet and desert world. *Meteorologische Zeitschrift* **14**, 305–314.

Fraedrich, K., E. Kirk, U. Luksch, and F. Lunkeit 2005. The portable university model of the atmosphere (PUMA): Storm track dynamics and low-frequency variability. *Meteorologische Zeitschrift 14*(6), 735–745.

Hoffman, P. F., and D. P. Schrag 2002. The snowball Earth hypothesis: testing the limits of global change. *Terra Nova 14*(3), 129–155.

Hörner, J., A. Voigt, and C. Braun 2022. Snowball earth initiation and the thermodynamics of sea ice. *Journal of Advances in Modeling Earth Systems* **14**.

Jacobs, S., H. Hellmer, C. Doake, A. Jenkins, and R. Frolich 1992. Melting of ice shelves and mass balance of antarctica. *Journal of Glaciology* **38**, 375–387.

Jernigan, J., É. Laflèche, A. Burke, and S. Olson 2023. Superhabitability of High-obliquity and High-eccentricity Planets. *944*(2), 205.

Journaux, B., K. Kalousová, C. Sotin, G. Tobie, S. Vance, J. Saur, O. Bollengier, L. Noack, T. Rückriemen-Bez, T. Van Hoolst, K. M. Soderlund, and J. M. Brown 2020. Large Ocean Worlds with High-Pressure Ices. *216*(1), 7.

Kopp, G., and J. L. Lean 2011. A new, lower value of total solar irradiance: Evidence and climate significance. *Geophysical Research Letters 38*(1).

Kopparapu, R. K., R. Ramirez, J. F. Kasting, V. Eymet, T. D. Robinson, S. Mahadevan, R. C. Terrien, S. Domagal-Goldman, V. Meadows, and R. Deshpande 2013. Habitable Zones around Main-sequence Stars: New Estimates. *765*(2), 131.

Köppen, W. 1936. *Das geographische System der Klimate*. Handbuch der Klimatologie in fünf Bänden. Borntraeger.

Lacis, A. A., and J. Hansen 1974. A parameterization for the absorption of solar radiation in the earth's atmosphere. *Journal of Atmospheric Sciences 31*(1), 118 – 133.

Lammer, H., J. H. Bredehöft, A. Coustenis, M. L. Khodachenko, L. Kaltenegger, O. Grasset, D. Prieur, F. Raulin, P. Ehrenfreund, M. Yamauchi, J. E. Wahlund, J. M. Grießmeier, G. Stangl, C. S. Cockell, Y. N. Kulikov, J. L. Grenfell, and H. Rauer 2009. What makes a planet habitable? *17*(2), 181–249.

Lammer, H., F. Selsis, E. Chassefière, D. Breuer, J.-M. Grießmeier, Y. N. Kulikov, N. V. Erkaev, M. L. Khodachenko, H. K. Biernat, F. Leblanc, E. Kallio, R. Lundin, F. Westall, S. J. Bauer, C. Beichman, W. Danchi, C. Eiroa, M. Fridlund, H. Gröller, A. Hanslmeier, W. Hausleitner, T. Henning, T. Herbst, L. Kaltenegger, A. Léger, M. Leitzinger, H. I. M. Lichtenegger, R. Liseau, J. Lunine, U. Motschmann, P. Odert, F. Paresce, J. Parnell, A. Penny, A. Quirrenbach, H. Rauer, H. Röttgering, J. Schneider, T. Spohn, A. Stadelmann, G. Stangl, D. Stam, G. Tinetti, and G. J. White 2010. Geophysical and Atmospheric Evolution of Habitable Planets. *Astrobiology 10*(1), 45–68.

Léger, A., F. Selsis, C. Sotin, T. Guillot, D. Despois, D. Mawet, M. Ollivier, A. Labèque, C. Valette, F. Brachet, B. Chazelas, and H. Lammer 2004. A new family of planets? "Ocean-Planets". *169*(2), 499–504.

Linsenmeier, M., S. Pascale, and V. Lucarini 2015. Climate of Earth-like planets with high obliquity and eccentric orbits: Implications for habitability conditions. **105**, 43–59.

Lucarini, V. 2009. Thermodynamic efficiency and entropy production in the climate system. *80*(2), 021118.

Lucarini, V., K. Fraedrich, and F. Lunkeit 2010. Thermodynamic analysis of snowball Earth hysteresis experiment: Efficiency, entropy production and irreversibility. *Quarterly Journal of the Royal Meteorological Society [L10] 136*(646), 2–11.

Lucarini, V., S. Pascale, R. Boschi, E. Kirk, and N. Iro 2013. Habitability and Multistability in Earth-like Planets. *Astronomische Nachrichten,[L13] 334*(6), 576.

Madden, J., and L. Kaltenegger 2020. How surfaces shape the climate of habitable exoplanets. *495*(1), 1–11.

Madhusudhan, N., S. Sarkar, S. Constantinou, M. Holmberg, A. A. A. Piette, and J. I. Moses 2023. Carbon-bearing Molecules in a Possible Hycean Atmosphere. *956*(1).

Nowajewski, P. 2018. *Atmospheric Dynamic Response by Obliquity Forcing*. Ph. D. thesis, Department of Geophysics, Universidad de Chile.

Nowajewski, P., M. Rojas, P. Rojo, and S. Kimeswenger 2018. Atmospheric dynamics and habitability range in Earth-like aquaplanets obliquity simulations. **305**, 84–90.

Paradise, A., K. Menou, D. Valencia, and C. Lee 2019. Habitable Snowballs: Temperate Land Conditions, Liquid Water, and Implications for CO_2 Weathering. *Journal of Geophysical Research (Planets) 124*(8), 2087–2100.

Pierrehumbert, R. T. 2004. High levels of atmospheric carbon dioxide necessary for the termination of global glaciation. *429*(6992), 646–649.

Pierrehumbert, R. T. 2010. *Principles of Planetary Climate*.

Rotman, Y., T. D. Komacek, G. L. Villanueva, T. J. Fauchez, and E. M. May 2023. General Circulation Model Constraints on the Detectability of the CO_2-CH_4 Biosignature Pair on TRAPPIST-1e with JWST. *942*(1), L4.

Salazar, A. M., S. Olson, T. D. Komacek, H. Stephens, and D. S. Abbot 2020. The Effect of Substellar Continent Size on Ocean Dynamics of Proxima Centauri b. In *AGU Fall Meeting Abstracts*, Volume 2020, pp. P013–0015.

Salby, M. L. 2012. *Physics of the Atmosphere and Climate* (2 ed.). Cambridge University Press.

Shields, A. L., C. M. Bitz, V. S. Meadows, M. M. Joshi, and T. D. Robinson 2014. Spectrum-driven Planetary Deglaciation due to Increases in Stellar Luminosity. *785*(1), L9.

Sleep, N. H., and K. Zahnle 2001. Carbon dioxide cycling and implications for climate on ancient Earth. *106*(E1), 1373–1400.

Stephens, G. L., S. Ackerman, and E. A. Smith 1984. A Shortwave Parameterization Revised to Improve Cloud Absorption. *Journal of the Atmospheric Sciences 41*(4), 687–690.

Stonevicius, E., G. Stankunavicius, and E. Rimkus 2018. Continentality and oceanity in the mid and high latitudes of the northern hemisphere and their links to atmospheric circulation. *Advances in Meteorology* **2018**, 1–12.

Tajika, E. 2008. Snowball Planets as a Possible Type of Water-Rich Terrestrial Planet in Extrasolar Planetary Systems. *680*(1), L53.

Turbet, M., T. J. Fauchez, J. Leconte, E. Bolmont, G. Chaverot, F. Forget, E. Millour, F. Selsis, B. Charnay, E. Ducrot, M. Gillon, A. Maurel, and G. L. Villanueva 2023. Water condensation zones around main sequence stars. **679**, A126.

Warren, S. G., R. E. Brandt, T. C. Grenfell, and C. P. McKay 2002. Snowball Earth: Ice thickness on the tropical ocean. *Journal of Geophysical Research (Oceans) 107*(C10), 3167.

Wolf, E., R. Kopparapu, V. Airapetian, T. Fauchez, S. D. Guzewich, S. R. Kane, D. Pidhorodetska, M. J. Way, D. S. Abbot, J. H. Checlair, C. E. Davis, A. D. Genio, C. Dong, S. Eggl, D. P. Fleming, Y. Fujii, N. Haghighipour, N. Heavens, W. G. Henning, N. Y. Kiang, M. López-Morales, J. Lustig-Yaeger, V. Meadows, C. T. Reinhard, S. Rugheimer, E. W. Schwieterman, A. L. Shields, L. Sohl, M. Turbet, and R. D. Wordsworth 2019. The Importance of 3D General Circulation Models for Characterizing the Climate and Habitability of Terrestrial Extrasolar Planets. *Astro2020: Decadal Survey on Astronomy and Astrophysics* **2020**, 177.

Yang, J., F. Ding, R. M. Ramirez, W. R. Peltier, Y. Hu, and Y. Liu 2017. Abrupt climate transition of icy worlds from snowball to moist or runaway greenhouse. *Nature Geoscience 10*(8), 556–560.

Annex A

PlaSim

A.1 Graphical User Interface

The initial interaction with the simulator involves launching the graphical user interface (GUI) of the model called Model Starter (MoSt), primarily responsible for generating the spatial framework and the essential files for the simulation as well as being the fastest way to get the model up and running. It is at this stage that we first engage with the configuration parameters required for our intended simulation.

Figure A.1 displays a screenshot of MoSt, showcasing the essential and commonly modified parameters within the model.

Initially, there is the option to choose between PUMA or PlaSim. PlaSim provides the flexibility to select the planet you wish to model, be it Earth, Mars, or an exoplanet.

Moreover, the graphical interface facilitates the configuration of fundamental attributes of the model, including:

- Modules

  In the 'Modules' section, you have the option to select whether you prefer to address sea ice and the ocean through climatology or modeling.

- Options:

  In Options, we can choose preferences such as debug mode, double precision, and whether to write output data or view it through the GUI.

- Parallelism:

  PlaSim is designed for use on both personal computers and mainframes, allowing parallel utilization of up to 32 cores.

- Resolution:

  The model offers three resolutions, namely, low resolution (T21), medium resolution (T32), and high resolution (T42). Table A.1 provides a summary of the implications associated with each available resolution.

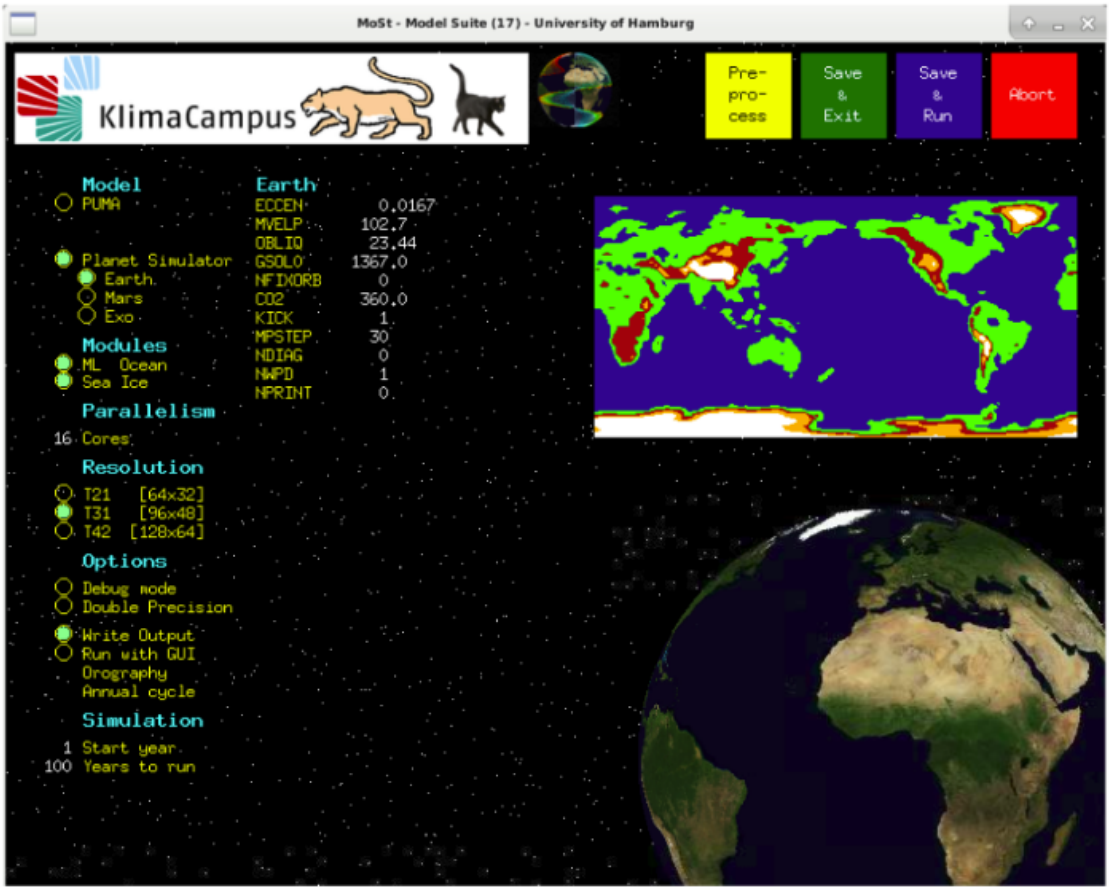

Figure A.1: GUI of PlaSim

Table A.1: Information about the resolutions

Resolution	Latitudes	Longitudes	Area
T21	32	64	5.6° x 5.6°
T32	48	96	4.2° x 4.2°
T42	64	128	2.8° x 2.8°

- Simulation's duration:

  This MIC facilitates climatic and paleoclimatic studies, enabling simulations of over 10,000 years within a reasonable timeframe

- Earth:

  When choosing to simulate a planet like Earth, real Earth data will automatically appear, which can be modified. Parameters include eccentricity (ECCEN), longitude of vernal equinox for fixed orbits (MVELP), obliquity (OBLIQ), solar constant (GSOLO), CO2 concentration (defaulting to 360 ppm), and more.

After adjusting the desired parameters, you can either run the simulation immediately by selecting the 'Save & Run' option or modify other parameters within the model. These modifications can be found in a folder created by PlaSim after selecting 'Save & Exit'.

A.2 Routines, Subroutines and Initial Masks

A.2.1 Namelist files

PlaSim employs two distinct file types that allow for the modification of initial conditions. The first file type, known as 'namelist' archives, serves as a means to manage the routines and subroutines of the model. These files contain essential instructions regarding inputs and outputs, guiding the behavior of the simulation. Most of the modifications established in the graphical interface are stored in one of these modules.

The table shows the modified namelist files. The remaining namelist files were not modified and kept their default values.

Table A.2: Modified namelist files

icemod_nl	
NICE	1
NFLUKO	1[a]
plasim_nl	
NOUTPUT	0
NGUI	1
N_START_YEAR	1
N_DAYS_PER_YEAR	360[b]
N_RUN_YEARS	100
N_RUN_MONTHS	0
N_RUN_DAYS	0
KICK	1
MPSTEP	30
NDIAG	0
NWPD	1
NPRINT	0
oceanmod_nl	
NOCEAN	1
NFLUKO	1[a]
radmod_nl	
CO2	400[b]

[a] Added and modified parameter
[b] Modified parameter

Table A.3: Unmodified namelist files

fluxmod_nl

landmod_nl

miscmod_nl

rainmod_nl

seamod_nl

submod_nl

vegmod_nl

planet_nl	
ECCEN	0.0167
MVELP	102.7
OBLIQ	23.44
GSOL0	1367
NFIXORB	0

A.2.2 '.sra' files

The second file type relates to the initial masks utilized by PlaSim. These masks define the starting conditions for the model, including critical factors such as land-sea distribution, glacier coverage, sea ice presence, orography (representing the surface elevation), and more. These files are named 'N0**_surf_xxxx.sra'. The '**' in the file name corresponds to the number of latitudes depending on the chosen resolution, as outlined in Table A.1. In the case of a low-resolution simulation (T21), '**' is set to 32. For medium resolution, '**' equals 48, and in the case of high resolution, it is adjusted to 64. The 'xxxx' part serves to uniquely identify each specific mask.

The table below shows the '.sra' files that contain the masks that can be modified by simulation. As our study was performed in medium resolution, the name of our '.sra' files starts with 'N048' since 48 is the number of latitudes it has.

Below you can see how the matrices found in each '.sra' file were handled to transform them into the desired masks:

- Surf. Geopotential Orography:

Table A.4: .sra files

Code	Name
N048_surf_0129.sra	Surf. Geopotential Orography
N048_surf_0169.sra	Surface Temperature
N048_surf_0172.sra	Land Sea Mask
N048_surf_0173.sra	Surface Roughness
N048_surf_0174.sra	Surface Albedo
N048_surf_0199.sra	Vegetation Cover
N048_surf_0210.sra	Sea Ice Cover
N048_surf_0212.sra	Forest Cover
N048_surf_0229.sra	Bucket Size
N048_surf_0232.sra	Glacier Cover

The first file, labeled 'N048_surf_0129.sra' features an 8x577 matrix. The top row within this matrix is dedicated to providing key mask information, including a unique code number and the total number of latitudes and longitudes utilized. In practice, the matrix we intend to modify is effectively 8x576 in size. This matrix holds geopotential height measurements for a map with 48 latitudes and 96 longitudes. Each latitude is represented by 12 lines (equivalent to 96 values), and the pattern continues for the remaining latitudes.

- Surf. Geopotential Orography:

  This time, we are in the presence of a 4x1153 mask, where its first line is mainly information about the mask and the following 24 lines compose the first latitude.

- Land-Sea Mask

  Enclosed within the file 'N048_surf_0172.sra' this grid shares dimensions with the previous orography matrix at 8x577. Similar to the orography matrix, this mask commences with a top row that contains essential information.

A.3 Postprocessor

The model provides two methods of delivering simulation results: through the graphical user interface (GUI) for visual inspection, and as files generated after each year of simulation. Since the visual data from the GUI is not required for any of our experiments, we have opted to receive the results in the form of annual data files.

These annual data files are created without a specific file extension and are substantial in size, as they encompass information on various parameters. To make this data more manageable, PlaSim provides a postprocessor. This postprocessor serves a dual purpose: first, it transforms the data into a more user-friendly format, and second, it extracts only the information or parameters that are pertinent to our analysis.

Furthermore, the postprocessor offers the ability to consolidate the annual files after extraction. This means that the data from each simulation can be amalgamated into a single

extensive file containing all the relevant information from every simulation.

Table A.5: The table shows the different parameters that can be extracted from the output files provided by Plasim

Code	Id	Name	Units
110	mld	Mixed Layer Depth	m
129	sg	Surf. Geopotential Orography	m2/s2
130	ta	Temperature	K
131	ua	Zonal Wind	m/s
132	va	Meridional Wind	m/s
133	hus	Specific Humidity	kg/kg
134	ps	Surface Pressure	hPa
135	wap	Vertical Velocity	Pa/s
137	wa	Vertical Wind	m/s
138	zet	a Vorticity	1/s
139	ts	Surface Temperature	K
140	mrso	Soil Wetness	m
141	snd	Snow Depth	m
142	prl	Large Scale Precipitation	m/s
143	prc	Convective Precipitation	m/s
144	prsn	Snow Fall	m/s
145	bld	Boundary Layer Dissipation	W/m**2
146	hfss	Surface Sensible Heat Flux	W/m**2
147	hfls	Surface Latent Heat Flux	W/m**2
148	stf	Streamfunction	m**2/s
149	psi	Velocity Potential	m**2/s
151	psl	Mean Sea Level Pressure	hPa
152	pl	Log Surface Pressure	
155	d	Divergence	1/s
156	zg	Geopotential Height	gpm
157	hur	Relative Humidity	%
158	tps	Tendency of Surface Pressure	Pa/s
159	u3	ustar **3	m**3/s**3
160	mrro	Surface Runoff	m/s
161	clw	Liquid Water Content	kg/kg
162	cl	Cloud Cover	0-1
163	tcc	Total Cloud Cover	0-1
164	clt	Total Cloud Cover (Mean)	0-1
165	uas	Eastward Wind 10m	m/s
166	vas	Northward Wind 10m	m/s
167	tas	2m Temperature	K
168	td2m	2m Dew Point Temperature	K
169	tsa	Surface Temperature Accumulated	K

Code	Id	Name	Units
170	tsod	Deep Soil Temperature	K
172	lsm	Land Sea Mask	
173	z0	Surface Roughness	m
174	alb	Surface Albedo	
176	rss	Surface Solar Radiation	W/m2
177	rls	Surface Thermal Radiation	W/m2
178	rst	Top Solar Radiation	W/m2
179	rlut	Top Thermal Radiation	W/m2
180	tauu	U-Stress	Pa
181	tauv	V-Stress	Pa
182	evap	Evaporation	m/s
183	tso	Soil Temperature	K
184	wsoi	Soil Wetness	
199	vegc	Vegetation Cover	
203	rsdt	Top Solar Radiation Upward	W/m2
204	ssru	Surface Solar Radiation Upward	W/m2
205	stru	Surface Therm Radiation Upward	W/m2
207	tso2	Soil Temperature Level 2	K
208	tso3	Soil Temperature Level 3	K
209	tso4	Soil Temperature Level 4	K
210	sic	Sea Ice Cover	
211	sit	Sea Ice Thickness	m
212	vegf	Forest Cover	
218	snm	Snow Melt	m/s
221	sndc	Snow Depth Change	m/s
230	prw	Vert. Integrated Spec. Hum.	kg/m2
232	glac	Glacier Cover	
259	spd	Wind Speed	m/s
260	pr	Total Precipitation	m/s
261	ntr	Net Top Radiation	W/m2
262	nbr	Net Bottom Radiation	W/m2
263	hfns	Net Heat Flux	W/m2
264	wfn	Net Water Flux	m/s

Annex B

Methodology of Multistability Experiments

The masks used in the simulations were designed to represent specific characteristics and conditions of the planets being studied. Here is a breakdown of the common masks used in all simulations and the masks that were modified according to each specific simulation:

⇒ Common mask in all simulations:

- Surface Geopotential Orography:

  This mask represents the land relief of the planet. In these simulations, all values were set to 0 meters above sea level, indicating a flat surface at all latitudes and longitudes.

- Land-Sea Mask:

  As the focus of the experiment is to study aquaplanets, snowballs, and transitional ice stages, the land sea mask was set to exclude any solid land, representing a planet without continents.

- Fractional Vegetation and Forest Ratio Masks:

  Since the simulations are based on extreme and idealistic scenarios, the presence of vegetation and forests is not considered. This mask removes all areas where vegetation would typically be found on a planet.

- Glacier Cover Mask:

  Predicting the exact locations of glaciers is challenging, especially without solid land present. Therefore, the glacier fraction was excluded from the simulations, and the albedo was determined solely by the sea ice and open water.

⇒ Masks modified according to each simulation:

- Sea Ice Cover:
  - Aquaplanet:
    All sea ice was removed, leaving only liquid water on the planet's surface.
  - Snowball:
    The entire planet was covered in ice, representing a fully frozen state.
  - Latitude 20°:
    Sea ice was present from the north pole to latitude 20° and from the south pole to latitude -20°, with a strip of liquid ocean at the equator.
  - Latitude 40°:
    Similar to the previous case, a strip of open water was included at the equator, extending between latitudes 40° to -40°, while the remaining areas were covered in sea ice.
  - Latitude 60°
    This mask represented a planet with sea ice extending up to latitude 60°. Similar to the previous cases, a strip of open water was present at the equator, but with slightly more open water compared to the latitude 40° simulation. This mask closely resembles the current amount of sea ice found on planet Earth. In Fig B.1 is possible to observe the actual sea ice modeled by PlaSim and the mask created to study the ice up to latitude 60°.

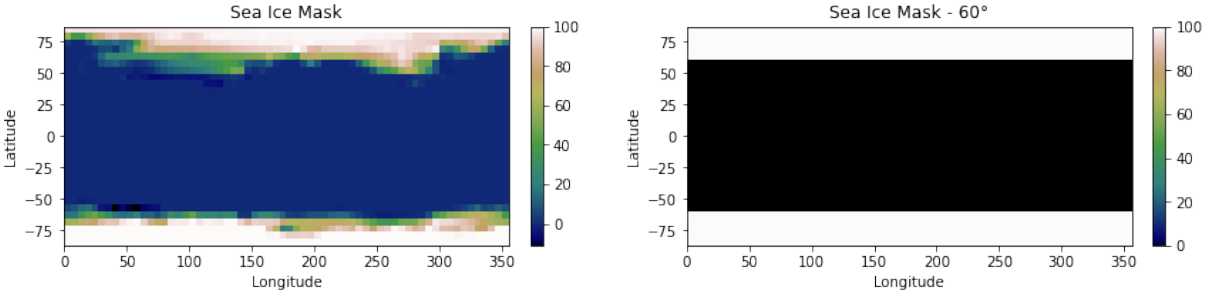

Figure B.1: Example of Sea Ice Mask

These masks played a crucial role in determining the initial conditions and configurations of sea ice for each simulation, allowing for the study of different climate states and transitions between them.

- Albedo Mask:
  The albedo mask was modified to reflect the amount of initial sea ice in each experiment. Areas with open water were assigned an albedo of 0.07, while areas with sea ice were assigned an albedo of 0.7. This differentiation in albedo values accounts for the difference in reflectivity between open water and sea ice.

- Surface Temperature Mask
  - Aquaplanet:
    The sea surface temperature (SST) profile formula from Neale & Hoskins (2001a) was used to adjust the temperature:

$$T_s(\phi) = \begin{cases} 27.0K \cdot (1 - \sin^2(\frac{3\phi}{2})) + 273.15K & \text{if } -\frac{\pi}{3} > \phi > \frac{\pi}{3} \\ 273.15K & \text{otherwise} \end{cases} \tag{B.1}$$

  - Snowball:
    In the snowball experiments, the entire planet was set to a temperature below freezing point, specifically 271 K, which represents the temperature of ice.
  - Latitude 20°:
    For this experiment, the temperature mask was created by assigning a temperature of 271 K to all sea ice areas. For the areas with open water, the temperature mask used was modified from the one used for the aquaplanets. The temperature at latitude 20° (or latitude -20° due to symmetry) was subtracted from the temperatures of the open water areas, allowing for a smooth transition between cold and warm regions.
  - Latitude 40° and Latitude 60°:
    Similar to the latitude 20° experiment, the temperature mask was created by assigning a temperature of 271 K to the sea ice areas. The temperature at the respective latitudes (40° and 60°) was subtracted from the temperatures of the open water areas, creating a gradual temperature transition.

The temperature profiles used in these experiments can be visualized in a graph, as shown in Figure B.2. The graph displays the initial temperature variations according to latitude, including the temperature used for the aquaplanet and the latitudes 20°, 40°, and 60°. It is evident that the colder regions have a temperature of 271 K, while the temperature slightly rises towards the equator in the warmer regions.

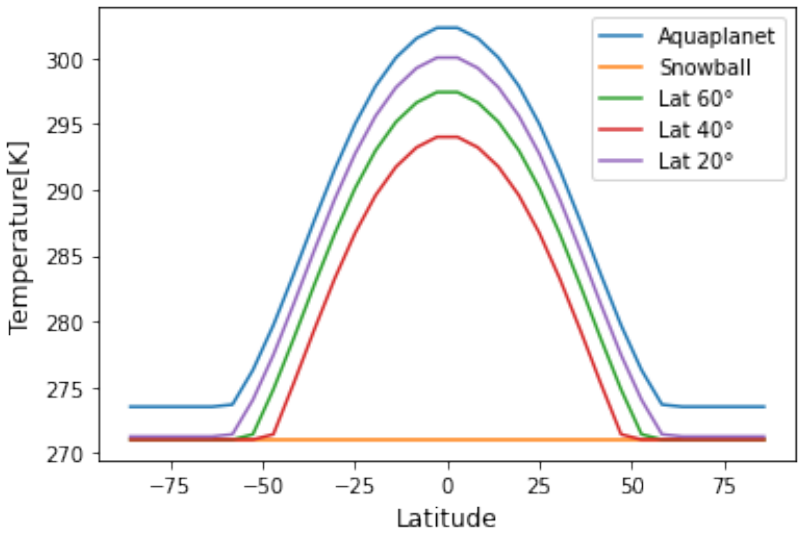

Figure B.2: Initial temperature for each latitude depending on the experiment carried out

Annex C

Extracted continents

Table C.1: IInformation about the extracted continents

Code	Name	Land Extracted [%]
SM	South-America	12.95
NM	North-America	15.85
SS	South-Asia	18.00
NS	North-Asia	11.50
F	Africa	23.00
A	Antarctica	8.32
O	Oceania	6.79
E	Europe	5.36
SM - NM	South-America and North-America	28.80
SS - NS	South-Asia and North-Asia	29.50
SM - O	South-America and Oceania	29.74
O - F	Oceania and Africa	28.97
F - A	Africa and Antarctica	31.33
E - SS	Europe and South-Asia	23.36
E - NS	Europe and North-Asia	16.85
SM - A	South-America and Antarctica	21.28
SM - F	South-America and Africa	35.13
O - A	Oceania and Antarctica	15.11
A - NM	Antarctica and North-America	24.17
SM - O - A	South-America, Oceania and Antarctica	28.07
SM - F - A	South-America, Africa and Antarctica	43.46
E - SS - NS	Europe, South Asia and North-Asia	35.86
F - E - SS	Africa, Europe and South-Asia	43.38
F - E - NS	Africa, Europe and North-Asia	39.77
NM - E - NS	North-America, Europe and North-Asia	32.70
SM - NM - A	South-America, North-America and Antarctica	37.13
SM - O - F	South-America, Oceania and Africa	41.92
NM - E - NS - SS	North-America, Europe , South-Asia and North-Asia	50.30
SM - O - F - A	South-America, Oceania, Africa and Antarctica	49.70

Table C.2: Information about the extracted continents

Code	**Name**	
O - F - E - SS	Oceania, Africa, Europe and South-Asia	50.17
O - F - E - NS	Oceania, Africa, Europe and North-Asia	46.58
O - F - E - SS - NS	Oceania, Africa, Europe, South-Asia and North-Asia	63.70
SM - NM - O - F - A	South-America, North-America, Oceania, Africa and Antarctica	66.10

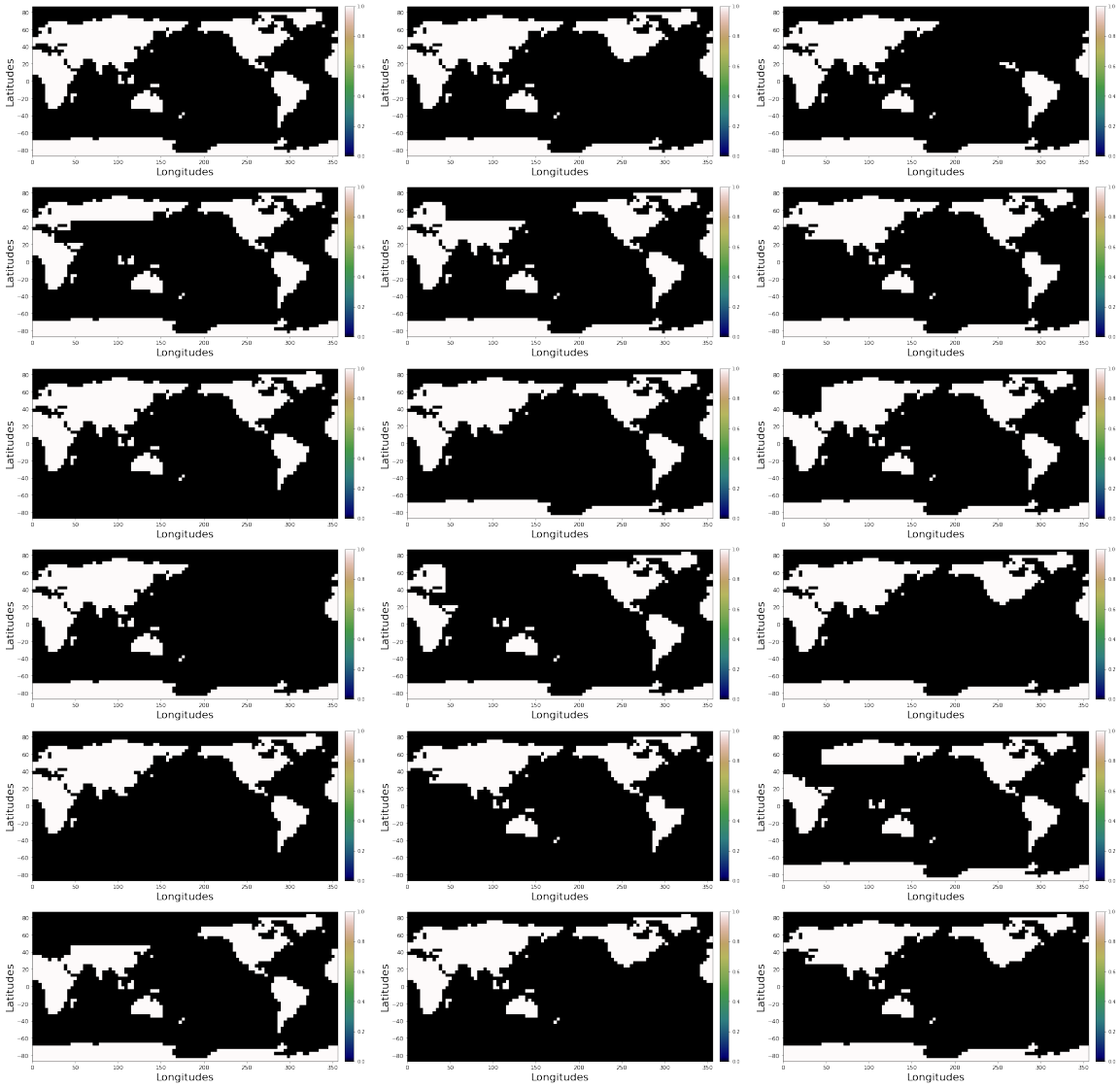

Figure C.1: Land-Sea mask for the different extracted continents

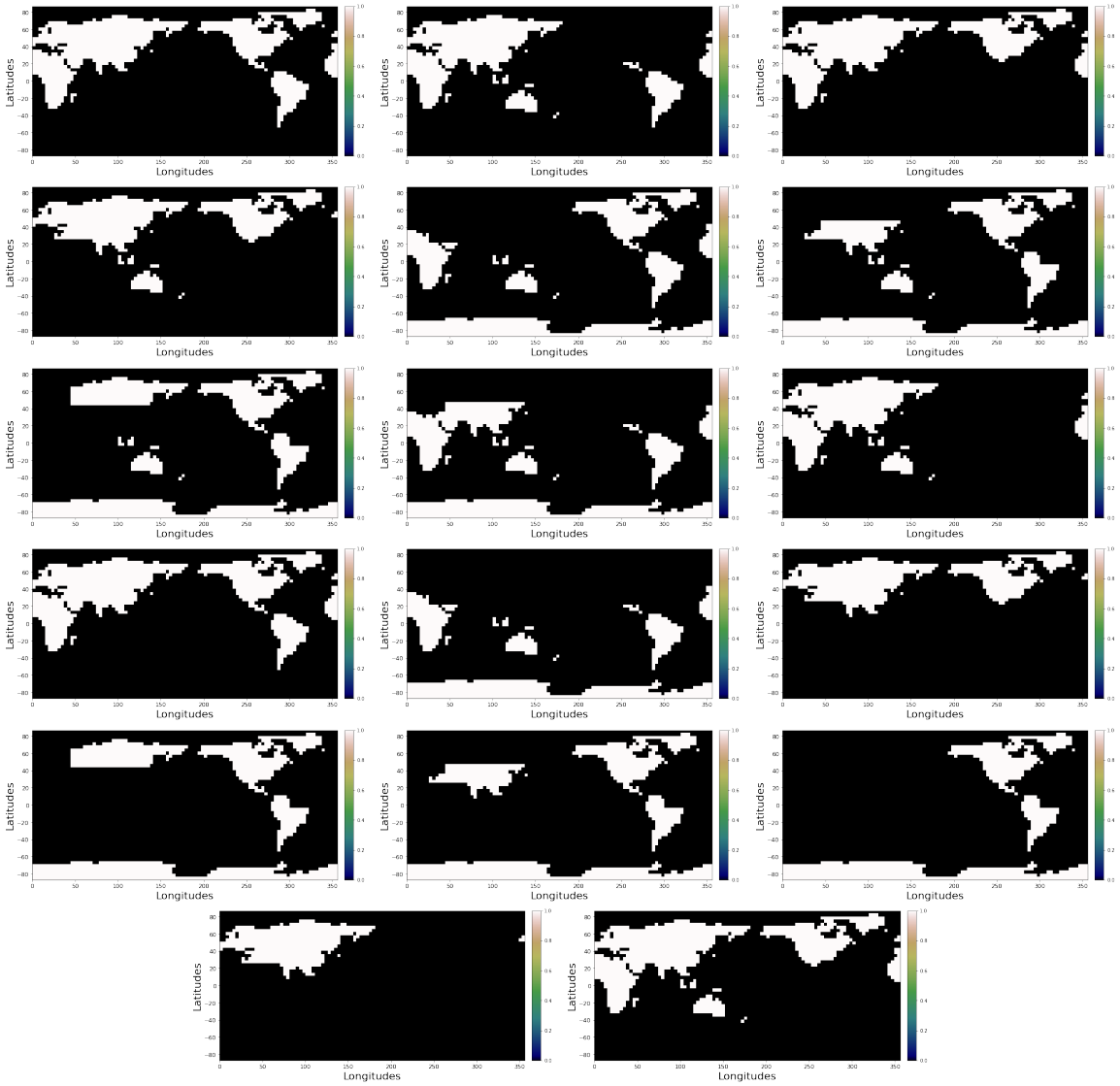

Figure C.2: Land-Sea mask for the different extracted continents

Annex D

Planetary equilibrium temperature

To calculate the planetary equilibrium temperature, we need to consider the balance between the absorbed flux and the emitted flux.

$$F_{absorbed} = F_{emitted} \tag{D.1}$$

The absorbed flux is the portion of radiation that is not reflected by the planet and is given by:

$$F_{absorbed} = (1 - A_B) * F_{star} \tag{D.2}$$

Where A_B is the Bond albedo representing the amount of reflected radiation, and F_{star} is the flux from the star reaching the planet.

The flux from the star can be estimated assuming the star behaves as a black body, and it is given by:

$$F_{star} = \sigma * T_{star}^4 \tag{D.3}$$

Where σ is a constant and T_{star} is the temperature of the star.

The luminosity of the star, which is the absolute amount of energy emitted per second, is defined as:

$$L_{star} = (\text{Area of the star}) \cdot F_{star} \tag{D.4}$$

and for a spherical star, we have:

$$L_{star} = 4\pi R_{star}^2 \sigma T_{star}^4 \tag{D.5}$$

where R_{star} is the radius of the star.

Replacing F_{star} in the equation, we get:

$$F_{star} = \frac{L_{star}}{4\pi R_{star}^2} \tag{D.6}$$

Finally, the absorbed flux can be expressed as:

$$F_{abs} = (1 - A_B)\frac{L_{star}}{4\pi R_{star}^2} \tag{D.7}$$

Therefore, the absorbed flux depends on the radius and luminosity of the star, as well as the Bond albedo.

To calculate the flux emitted by the star, we consider the planet as another black body that emits radiation. The emitted flux can be calculated using the Stefan-Boltzmann law:

$$F_{emitted} = \sigma T_{planet}^4 \tag{D.8}$$

Substituting this expression into the initial equation D.1 and rearranging, we have:

$$(1 - A_B)\frac{L_{star}}{4\pi R_{star}^2} = \sigma T_{planet}^4 \tag{D.9}$$

Solving for the equilibrium temperature of the planet (T_{planet}), we have:

$$T_{planet}^4 = (1 - A_B)\frac{L_{star}}{4\pi R_{star}^2 \sigma} \tag{D.10}$$

Taking the fourth root of both sides, we get:

$$T_{planet}^4 = (1 - A_B)\frac{L_{star}}{4\pi R_{star}^2 \sigma} \tag{D.11}$$

$$T_{planet} = \sqrt[4]{(1 - A_B)\frac{L_{star}}{4\pi R_{star}^2 \sigma}} \tag{D.12}$$

Therefore, the equilibrium temperature of the planet is given by the fourth root of the quantity $(1 - A_B)$ times the ratio of the star's luminosity to the product of 4 times the square of the star's radius and the constant σ.

In the case of the Sun, we can substitute the values specific to the Sun into the equation to calculate the equilibrium temperature of the planet:

$$T_{planet} = \sqrt[4]{(1 - A_B)\frac{L_{sun}}{4\pi R_{sun}^2 \sigma}}$$

$$T_{planet} = \sqrt[4]{\frac{(1 - A_B)}{4\sigma}}\sqrt[4]{\frac{L_{sun}}{4\pi R_{sun}^2}}$$

$$T_{planet} = \sqrt[4]{\frac{(1 - A_B)}{4\sigma}}\sqrt[4]{I_o} \tag{D.13}$$